AN ABSTRACT OF THE DISSERTATION OF

Anthony Ryan Kirincich for the degree of Doctor of Philosophy in Oceanography presented on May 24, 2007.

Title: Inner-shelf Circulation off the Central Oregon Coast.

Abstract approved: _____

John A. Barth

Inner-shelf circulation and mechanisms of across-shelf transport of water masses were examined using seven years of observations collected by the Partnership for Interdisciplinary Studies of Coastal Oceans (PISCO) program, a long-term monitoring effort along the central Oregon coast. Since 1998, moored velocity and hydrographic measurements have been obtained during the summer upwelling season in water depths of 30, 15, or 8 m at 3-5 stations along a 75 km stretch of the Oregon shelf. These observations enabled a description of along-shelf variations and upwelling dynamics in an area of intermittent wind forcing but little buoyancy influences. While wind forcing and bathymetry were nearly spatially uniform in the inner-shelf, circulation was spatially variable due to an offshore submarine bank. Classic two-dimensional upwelling existed north of the bank, with bottom stress and acceleration balancing the wind stress in the depth-averaged along-shelf momentum equation. This balance failed onshore of the bank where the pressure gradient and nonlinear advection were needed to close the momentum balance. Driven by along-shelf wind forcing, across-shelf surface transport was 25% of the theoretical Ekman transport at 15 m water depth, 1-2 km offshore, and reached full Ekman transport 5-6 km offshore in 50 m of water. This result, based on season-long comparisons of measured across-shelf transport and theoretical Ekman transport, defines the across-shelf scale of

coastal upwelling on the Oregon shelf. However, observations of across-shelf circulation also highlight the rapid movement of water masses and variable residence times in the inner shelf. To quantify the time variability of across-shelf exchange, a numerical model was adapted to estimate vertical eddy viscosity using the velocity measurements. Resulting depth-averaged eddy viscosities ranged from $0.8\text{x}10^{-3}$ m^2 s^{-1} during upwelling winds to $2.1\text{x}10^{-3}$ m^2 s^{-1} during downwelling winds, consistent with previous numerical model results. The difference in eddy viscosities between upwelling and downwelling led to varying across-shelf exchange efficiencies and increased net upwelling over time. These results quantify the structure and variability of circulation in the inner-shelf and have significant implications for ecological processes (e.g., larval recruitment, nutrient availability) in the region.

Inner-shelf Circulation off the Central Oregon Coast

by

Anthony Ryan Kirincich

A DISSERTATION

submitted to

Oregon State University

in partial fulfillment of
the requirements for the
degree of

Doctor of Philosophy

Presented May 24, 2007
Commencement June 2007

Doctor of Philosophy dissertation of Anthony Ryan Kirincich presented on May 24, 2007

APPROVED:

Major Professor, representing Oceanography

Dean of the College of Oceanic and Atmospheric Sciences

Dean of the Graduate School

I understand that my dissertation will become part of the permanent collection of Oregon State University libraries. My signature below authorizes release of my dissertation to any reader upon request.

Anthony Ryan Kirincich, Author

ACKNOWLEDGMENTS

I wish to thank my advisor, Jack Barth, for investing his time and resources in me. Jack is a great mentor and from the beginning showed a level of confidence in my abilities that I often did not share. Over the years he has taught by example how to understand concepts and explore new questions, giving me the freedom to work and progress on my own, all the while keeping a watchful eye. His continuous attention, effort, advice, and encouragement have empowered me to grow as a student, a researcher, and as a scientist.

I also would also like to thank all my committee members: Jack, Bruce Menge, Murray Levine, Ed Dever, Jonathan Nash, and Philip Watson for giving helpful suggestions and offering to read drafts. Their time and effort contributed greatly to this work and my success here.

This research was made possible by PISCO, the Partnership for Interdisciplinary Studies of Coastal Oceans funded primarily by the Gordon and Betty Moore Foundation and David and Lucile Packard Foundation. Bruce Menge, Jane Lubchenco, and Jack Barth are the principle investigators of the PISCO program at OSU and are responsible for the program's, funding, management, and data collection. I thank them for the opportunity to be a part of this incredible effort and contribute to its goals.

Scores of individuals have helped me significantly in my tenure here, whether through data collection, technical assistance, or water cooler commiseration. I wish to recognize a few of them here: Brian Grantham, Chris Holmes, Susan Holmes, Matt Robart, Greg Hudson, Captain Perry York, Rick Plummer, Jed Moore, Josh Schuening, Joe Long, Chris Chickadel, Jason Killian, Chris Scott, Francis Chan, Joe Tyburczy, Sarah Dudas, Renato Castelao, Andy Dale, Steve Pierce, Chris Wingard, Bob O'Malley, Walt Waldorf, and Alan Barton.

Finally, there is no better editor, sounding board, cheerleader, lab assistant, practice

audience, or friend than one's spouse. I simply could not have arrived at this point without her love and encouragement and thus, this document is as much hers as it is mine. Great job, Jody!

CONTRIBUTION OF AUTHORS

Dr. John A. Barth was involved in the analysis and writing of each manuscript of this dissertation. Drs. Bruce Menge, Jane Lubchenco, and Brian Grantham were involved in the writing of Chapter 2.

TABLE OF CONTENTS

TABLE OF CONTENTS (Continued)

TABLE OF CONTENTS (Continued)

LIST OF FIGURES

LIST OF FIGURES (Continued)

LIST OF TABLES

INNER-SHELF CIRCULATION OFF THE CENTRAL OREGON COAST

1. INTRODUCTION

The mechanisms by which the nearshore waters of the coastal margin communicate with the larger coastal ocean are of critical importance to life, including humankind, along our coastlines. The physical processes at work in this small fraction of the ocean's surface control how different water masses, nutrients, pollutants, and larvae are transported out of or into the coastal margin. Coastal biological communities depend on these processes for food, shelter, and transportation. Humankind depends on these processes to provide (or host) the ecological services that sustain commercial fisheries, increase recreational value, disperse nearshore pollutants, and provide transportation pathways. Variations of this communication in time or space can alter ocean conditions both onshore and offshore, having significant implications for ecological communities. The physical mechanisms controlling across-shelf exchange are well-studied in coastal regions dominated by buoyant sources such as river plumes (Wiseman and Garvine, 1995; Yankovsky et al., 2000; Garvine, 2004; Kirincich and Hebert, 2005). Yet on wind-forced shelves, much of the previous research has focused on either the dynamics of the well-mixed surf zone inshore (Svendsen, 2006; Komar, 1998) or the larger-scale dynamics of the stratified ocean offshore (Hickey, 1998; Huyer, 1990). Mechanisms of across-shelf exchange in the transition region that must exist between them have only recently become an active area of research. This work attempts to better our understanding of this oceanic transition zone, referred to as the inner shelf, along wind-forced shelves by using observations from a long-term

monitoring program along the central Oregon coast.

Much of the west coast of the United States has a narrow ribbon of continental shelf between it and the abyssal ocean. As the basin-wide circulation is relatively weak along this eastern boundary of the North Pacific ocean, regionally generated coastal currents are the dominant mesoscale features (Hickey, 1998). On and adjacent to the shelf, wintertime flows are mostly northward but variable in time, as a result of large-scale northward pressure forcing and variable, winter-storm dominated, atmospheric forcing (Hickey, 1998). During summer, more stable atmospheric conditions force the regional ocean with southward, upwelling-favorable winds (Huyer, 1983). The upwelling circulation these summertime conditions enable make the California Current Large Marine Ecosystem one of the world's most productive areas (Pauly and Christensen, 1995), supporting large stocks of pelagic and sessile plants and invertebrates as well as significant recreational and commercial fisheries.

Located within the northern part of the system, the central Oregon shelf is a particularly productive region of the California Current system (Small and Menzies, 1981). Flow over the continental shelf off Oregon has been documented in numerous process studies [originally: CUE-I (Smith, 1974; Huyer et al., 1974), CUE-II (Kundu and Allen, 1976), and more recently: the 1999 NOPP project (Oke et al., 2002a,b; Barth et al., 2005a), the 2001 COAST project (Barth et al., 2005b; Kosro, 2005)] as well as long-term monitoring projects [GLOBEC: (Smith et al., 2001; Huyer et al., 2005), and coastal HF radar observations (Kosro, 2005)]. Here, strong stratification and intermittent upwelling winds work to create a dynamic system during the spring and summer. Additionally, the physical circulation created by these meteorological and hydrographic conditions are affected, through flow-topography interactions, by a sub-surface bathymetric feature in the region (Barth et al., 2005a; Castelao and Barth, 2005). This feature, the Stonewall and Heceta Bank Complex (the bank), widens the continental shelf from 13 km north of the bank to 60 km

over the bank, causing a complex three-dimensional (3D) physical circulation that further increases productivity above and inshore of the bank complex (Barth et al., 2005a).

In contrast to the variable bathymetry offshore along the central Oregon coast, relatively uniform along-shelf conditions exist onshore in the inner shelf. The inner shelf is physically defined here as lying between the 10 and 50 m isobaths, located from 0.5 to 5-6 km offshore. However, a number of dynamical definitions of this transition zone have been given in the literature. Based on momentum balances along the North Carolina coast, Lentz et al. (1999) inferred that the inner shelf extends from the surf zone offshore to the 13 m isobath. A second definition, valid on wind-driven shelves such as the Oregon shelf, is the zone encompassing the divergence of Ekman transport marking the region of active upwelling. Analytical models of shelf-wide upwelling dynamics have tended to use the offshore edge of the inner-shelf as their onshore boundary condition (Samelson, 1997). In contrast, many numerical models use a vertical wall at water depths of 10 m as the inshore edge of their domains (Oke et al., 2002a; Gan and Allen, 2005). Comparisons of inner-shelf width between these definitions vary significantly over time and space as hydrographic, bathymetric, and forcing conditions change. Yet, how circulation and across-shelf exchange occur in this transition zone, regardless of its definition, controls how nearshore waters communicate with the larger coastal ocean.

In recent years, a number of studies have made progress in understanding this exchange on wind-driven shelves not strongly influenced by buoyant coastal plumes. Both with observations (Lentz and Winant, 1986; Lentz, 1994; Lentz et al., 1999; Lentz, 2001) and numerical models (Austin and Lentz, 2002; Kuebel Cervantes et al., 2003; Tilburg, 2003), these works have begun to illustrate the transition of shelf-scale physical processes into the surf zone inshore. Lentz and Winant (1986) reported that inner-shelf circulation within the Southern California Bight was dominated by along-shelf currents closely linked to large-scale wind stress and pressure gradients, but that this simple relationship

broke down when waters became more stratified. Lentz (1994) illustrated the reduction of along-shelf current magnitudes in the inner-shelf, relative to currents offshore of Northern California as well as the role of the inner-shelf in leading current reversals that occurred during wind relaxations. Comparing these measurements to one-dimensional numerical models, Lentz (1994) found good agreement between along-shelf currents but had less success with across-shelf currents. This difference resulted from an incorrect parameterization of vertical diffusion of turbulent momentum in the models (Lentz, 1994, 1995). Depth-averaged momentum balances between the 4 and 13 m isobaths off North Carolina (Lentz et al., 1999) were dominated by the surface and bottom stresses in the along-shelf direction and wave setup in the across-shelf direction. Offshore of 13m, geostrophy dominated the across-shelf momentum balance while a complex combination of surface and bottom stresses, pressure gradients, and acceleration existed in the along-shelf direction (Lentz et al., 1999). In later work from the North Carolina coast, Lentz (2001) documented the across-shelf divergence of Ekman transport as occurring between the 5 and the 40 m isobaths. Two-dimensional numerical modeling efforts of the inner-shelf (Austin and Lentz, 2002; Kuebel Cervantes et al., 2003) have illustrated the movement of density stratification due to upwelling or downwelling events and the response of the coastal ocean to wind forcing events. These efforts have described the types of conditions that can cause reduced across-shelf exchange and the sequestering of water masses onshore. The collective results of these modeling and observational studies form a basic understanding of circulation dynamics in this transition region. Yet they also raise further questions about the magnitude and variability of across-shelf exchange, the transitioning physical processes in the inner-shelf, and their affects on nearby ecological systems.

Until recently no descriptive or process studies existed for the inner shelf along the central Oregon coast, an area of regional importance physically, ecologically, and economically. In 1998, the Partnership for Interdisciplinary Studies of Coastal Oceans (PISCO)

program began making these types of measurements as part of a long-term monitoring effort. The program, a consortium created to study the link between inner-shelf oceanography and marine ecosystems along the U.S. west coast, aims to quantify patterns of distribution, abundance, and diversity in nearshore communities and determine how oceanographic processes influence these patterns. Funded primarily by the David and Lucile Packard Foundation and the Gordon and Betty Moore Foundation, the PISCO program at OSU has greatly aided coastal oceanographic studies through its interdisciplinary efforts. Besides observing the physical circulation of the inner shelf, its operations have enabled new oceanographic topics such as inner-shelf hypoxia, mechanisms of larval transport, and local/regional responses to climate variability to be addressed.

To accomplish these goals, the oceanographic component of PISCO at OSU maintains an array of inner-shelf hydrographic and velocity moorings along a 70 km stretch of the central Oregon coast. Each year during the summer upwelling season, spanning April to October, the program measures temperature, salinity, velocity, bottom pressure, chlorophyll fluorescence, and dissolved oxygen in water depths ranging from 8 to 30 m. Over time the size, shape, and composition of the mooring array has varied, but a number of core sites have been occupied since its inception. In recent years a total of 70 thermistors, 6 conductivity-temperature sensors, 4 fluorometers, 2 oxygen sensors, and 4 acoustic Doppler current profiles (ADCPs) with bottom pressure have been deployed, serviced, and recovered each season. While not all measurements are made at all locations, water-column temperature is the most common measurement and 15 m water depth is the main station depth. Adding value to this observational array, the program has supported process studies on inner-shelf dynamics using towed sensor packages to collect high-resolution hydrographic sections, and seasonal, shelf-wide hydrographic sampling.

The goal of this dissertation is to increase our understanding of inner-shelf dynamics along the central Oregon coast by quantifying how across-shelf exchange occurs over

varying temporal and spatial scales and how the external forcing and shelf-wide processes control the character of inner-shelf circulation. This work uses the PISCO observations to quantify the wind-driven dynamics in an area where observations as well as a dynamical understanding of the physical processes have been lacking. The result forms a physical foundation for future interdisciplinary analysis that will continue to directly address PISCO's ecological goals. The remainder of this document is divided into three manuscripts, each addressing a different component of inner-shelf dynamics along the central Oregon coast. As presented, they focus on dynamics over continually decreasing temporal and spatial scales.

Chapter 2, entitled "Wind-driven inner-shelf circulation off central Oregon during summer", uses 4 years of velocity observations from these inner-shelf stations to quantify the across-shelf divergence of Ekman transport. In general, the measured fraction of across-shelf surface transport was found to be 25% of theoretical Ekman transport in 15 m of water, 1-2 km offshore, and 100% of full Ekman transport in 50 m of water, 5-6 km offshore. This result indicates that the region of active upwelling marked by the divergence of Ekman transport is limited to a narrow region along the central Oregon coast. Comparing these results with previous studies finds that the thickness of the Ekman layer and water depth are the main controllers of the across-shelf scale of this region.

Chapter 3, entitled "Spatial and temporal variability of inner-shelf circulation along the central Oregon coast during summer", focuses on the 2004 upwelling season to describe the seasonal development of inner-shelf circulation and the spatial differences that exist within the region. The effect of the offshore bank on inner-shelf circulation was striking, as stations inshore of the bank were isolated from a station north of the bank, exhibiting different dynamics. This isolation developed and intensified as the upwelling season progressed.

Chapter 4, entitled "Time-varying across-shelf Ekman transport and vertical eddy

viscosity on the inner shelf", investigates the event-scale variability of across-shelf exchange in the inner shelf using hydrographic and velocity observations from 2004. This work uncovers the rapid across-shelf movement of water masses and variable residence times that exist. An inverse calculation, used to estimate the vertical diffusion of momentum and eddy viscosity, further highlights the variability of the efficiency of across-shelf exchange as well as biases in its direction.

Finally, the overarching results of these works are summarized in Chapter 5. Here, the salient features of the Oregon inner shelf are condensed, the ecological implications of this work are linked to results from ongoing biological sampling efforts, and ideas for future studies are given.

2. WIND-DRIVEN INNER-SHELF CIRCULATION OFF CENTRAL OREGON DURING SUMMER.

Anthony R. Kirincich, John A. Barth, Brian A. Grantham, Bruce A. Menge, and Jane Lubchenco

Journal of Geophysical Research

2000 Florida Avenue, N.W. Washington, DC 20009, USA

Vol. 110, 2005, doi:10.1029/2004JC002611.

Abstract

Velocity measurements from 17 deployments of moored acoustic Doppler current profilers obtained during four summer upwelling seasons are used to describe the across-shelf divergence of Ekman transport in the inner shelf off Oregon. For each deployment, the measured surface and bottom across-shelf transports were compared with estimates of the theoretical Ekman transports to find the fraction of full theoretical Ekman transport present. In general, in 15 m of water at 1-2 km offshore, measured transport was 25% of the full Ekman transport. Measured transports reached full Ekman transport 5-6 km offshore in 50 m of water. This result indicates that the region of active upwelling marked by the divergence of Ekman transport was limited to a narrow region along the coast. With small wind stress curl and no major headlands in the region, no along-shelf trends in the transport fractions were observed. Average transport fractions at each station were similar from year to year with one exception. The interannual variability seen at this particular site was most likely a result of local along-shelf bathymetric features. In addition, a weak linear relationship was found between the ambient stratification and the fraction of full Ekman transport. Reduced across-shelf transport occurred at times of decreased stratification. This type of 'shutdown' of the inner-shelf across-shelf circulation has significant biological implications, sequestering production in the nearshore and reducing larval across-shelf transport.

2.1. Introduction

The across-shelf circulation associated with coastal upwelling has been well documented for wind-driven middle and outer continental shelves, where water depths are generally deeper than 50 m. Numerous review papers exist on the subject (Huyer, 1983,

1990; Hickey, 1998) and the interactions of the wind forcing, surface and bottom transports, and bottom stress from these phenomena have been documented on many of the world's continental shelves (Allen and Smith, 1981; Smith, 1995). In general, all describe an across-shelf circulation with offshore surface Ekman transport driven by the along-shelf wind stress. A return flow exists either in the interior of the fluid or in the bottom boundary layer (BBL) created by the interaction of the along-shelf current and the shelf bottom. The contributions of the interior and BBL to the return flow over the middle to outer shelf is dictated by the slope Burger number, a measure of the relative importance of stratification and bottom slope (MacCready and Rhines, 1993; Austin and Lentz, 2002). Most middle and outer-shelf investigations of upwelling have found fully developed Ekman transport in the boundary layers with small stresses in the interior (Lentz, 1992; Lentz and Trowbridge, 1991). Less is known about downwelling circulation, although observational (Winant, 1980) and model studies (Austin and Lentz, 2002; Allen et al., 1995) confirm the same notion of wind-forced onshore Ekman transport and offshore compensatory flow beneath.

Inshore of these middle and outer shelf locations exists a region in which the wind-driven across-shelf Ekman transport is reduced in magnitude due to the presence of a coastal wall (Gill, 1982). The across-shelf extent of this divergence of Ekman transport encompasses the region of active upwelling or downwelling (Lentz, 2001) and is bounded offshore by the upwelling or downwelling front. Further, using a numerical model Allen et al. (1995) found a large fraction of upwelling takes place in relatively shallow water near the coast. Their results showed that half of the upwelled water came directly from the BBL in shallow water inshore of 20 m depth. In this area, surface and bottom boundary layers occupy the entire water column (Lentz, 1995). Thus, on wind-driven shelves the inner shelf serves as a transition zone between the middle and outer shelf, where wind forcing and large-scale pressure gradients are dominant forces, and the nearshore where

surface-gravity wave radiation stresses are large.

A number of recent investigations have attempted to document the nature of across-shelf circulation in the inner shelf. In 30 m of water off central California, Lentz (1994) identified an across-shelf surface flow driven by along-shelf winds and a bottom return flow driven by the along-shelf jet. In Lentz's study area, flow was found to be essentially two dimensional, with no significant depth-averaged across-shelf flow (Lentz, 1994). Using a across-shelf array of moorings on the wide, gently sloping North Carolina shelf, Lentz (2001) observed across-shelf transport increased moving offshore as dictated by Ekman theory. He reported large differences in across-shelf transports between summer, when waters were more stratified, and fall, when waters were only weakly stratified. Demonstrating stratification's effect on transport, Allen et al. (1995) showed the majority of upwelling occurred within 3 km of the coast when stratification was present, and within 8 km of the coast when no stratification was present. Austin and Lentz (2002) obtained similar results, finding that across-shelf transports in the inner shelf decreased as stratification was reduced.

Summarizing these previous works, circulation in this shallow area is dependent on wind forcing, but can be significantly influenced by stratification. The link between the level of stratification and the amount of across-shelf Ekman transport exists because reducing the stratification increases the eddy viscosity (A), which increases the Ekman layer depth (d) as $d = \sqrt{2A/f}$, where f is the Coriolis parameter. For shallow water near the coast, less of the Ekman spiral is realized when stratification is reduced, leading to a reduction in across-shelf transport. This type of reduction (or shutdown) of across-shelf circulation as a result of reduced stratification in the inner shelf affects the circulation dynamics of the entire shelf (Lentz, 2001; Samelson, 1997) and may be important for biological processes as well. In particular, understanding patterns of across-shelf circulation is key to understanding the processes responsible for transport of larvae and particulates

(phytoplankton and detritus) to and from benthic coastal habitats (Morgan, 2001).

The study described here analyzes the across-shelf circulation in the narrow, steeply sloping inner shelf along the coast of central Oregon. Located on the eastern boundary of the North Pacific Ocean, the shelf-wide upwelling system off Oregon has been well documented (Allen and Smith, 1981; Huyer, 1983) and is known for its high productivity (Small and Menzies, 1981). During summer, southward winds with mean values of 0.03 N m^{-2} and small offshore wind stress curl (Samelson et al., 2002) drive offshore surface flow, upwelling, and an along-shore equatorward jet with mean velocities reaching 0.25 m s^{-1} (Huyer, 1983). Shelf waters off Oregon are generally highly stratified with top to bottom density differences as large as 2 kg m^{-3} regularly occurring (Huyer, 1983). For the most part, these shelf studies have left the inner shelf off Oregon poorly resolved. However, since 1999 the Partnership for Interdisciplinary Studies of Coastal Oceans (PISCO) program has collected numerous long-term hydrographic and velocity measurements in the inner shelf along the central Oregon coast.

The PISCO program is a long-term ecological consortium created in 1998 to study the link between inner-shelf oceanography and marine ecosystems along the U.S. west coast. The objectives of the program are to quantify patterns of distribution, abundance, and diversity in nearshore communities and determine how oceanographic processes influence these patterns. This study begins to quantify the wind-driven dynamics in the inner shelf, forming a foundation for interdisciplinary analyses to follow. A companion paper by Austin and Grantham (in progress) uses different portions of the PISCO data set to analyze sub-inertial along-shelf and across-shelf variability in the inner shelf off Oregon. In summary, the PISCO project has enabled the transition between shelf and nearshore circulation occurring within the inner shelf to be more clearly understood.

Using measurements obtained from the long-term mooring efforts taking place in the region, this study describes the offshore extent of the Ekman divergence off Oregon by

comparing the measured across-shelf transports to theoretical values. The observations used in this study are introduced in Section 2, along with the theory and data analysis techniques employed to compute the measured and theoretical Ekman transports. Section 3 describes the results of the transport fraction calculation and then examines the effects of both stratification and the frictional coefficient used to obtain bottom stress. A discussion of the key results follows in Section 4, including a comparison with previous results from the wide, gently sloping North Carolina shelf. Section 5 summarizes the findings of this study.

2.2. Data and Methods

2.2.1 Data sources

The bulk of the observations used here were made as part of PISCO's Oregon State University (OSU) mooring program. This mooring component of the larger PISCO program has collected hydrographic measurements in Oregon's inner shelf each summer since 1998. Data from years 1999, 2001, 2002, and 2003 are examined here while similar measurements from years 1998, 1999, and 2000 are presented in Austin and Grantham (in progress). Over the course of the four summers examined here, the program made 14 deployments of bottom-mounted upward-looking acoustic Doppler current profilers (ADCPs) at 6 locations spanning an along-shelf distance of 83 km (Figures 2.1 and 2.2). The ADCPs, 600-kHz Workhorse Broadband Sentinels from RD Instruments, collected 2 minute averages of water velocities from 1-m depth increments starting 3 m above the seafloor. Adjacent to each ADCP deployment, a separate mooring recorded temperature at multiple depths and conductivity at mid-water. These instruments sampled every 2-30 minutes, depending on the instrument and deployment year.

The deployed ADCP array varied in size and locations among the years described.

Mean water depths for the deployments ranged from 8 to 30 m, although most were located at 15 m (Table 2.1, Figure 2.3). While only one deployment occurred in 1999 at station YH at 15 m of water, five were made in 2001, with two measurement intervals at 15 m at station CH separated by 20 days, and 8-m and 15 m deployments at both stations FC and SH. In 2002, 15 m deployments occurred at stations FC (two measurement intervals separated by 20 days), SR, and SH, while shorter 30 m deployments were also made at stations FC and SH. The array was reduced in 2003, with 15 m deployments at stations LB (near FC), SR, and SH only.

To augment the PISCO array with offshore observations, 3 additional velocity measurements from adjacent field programs are included in this study. Velocity profiles were obtained from a 1999 deployment at station IS, located offshore and 5 km south of station YH (Figure 2.1), as part of the Prediction of Wind-Driven Coastal Circulation Project, a NOPP Project (Boyd et al., 2000; Oke et al., 2002a,b). Similar deployments were made in 2001 as part of the Coastal Ocean Advances in Shelf Transport (COAST) Project offshore of stations CH and SH (Boyd et al., 2002). Each of these three deployments, all at 50 m depth, consisted of moored upward-looking 300-kHz RDI Workhorse Broadband ADCPs, collecting 2 minute ensemble averages in 2-m bins starting at 8 m above the seafloor.

Observations from a number of buoy and coastal stations were used to estimate the wind velocities at each mooring location. Hourly averages of wind measurements from the NOAA National Data Buoy Center's (NDBC) buoy 46050 and the Newport, Oregon NOAA Coastal Marine Automated Network (CMAN) station NWPO3 are examined in this study. The CMAN station is located on the south jetty of the Newport harbor entrance while buoy 46050 is located 33 km west of Newport in 100 m of water (Figure 2.1). In addition, hourly averages of wind measurements obtained by meteorological buoys operated by the 1999 NOPP program and the 2001 COAST program were taken into consideration as mid-shelf estimates of wind velocity during those years (Figure 2.1).

Wind velocities are not measured as part of the PISCO program.

2.2.2 Ekman transport theory

The wind-driven across-shelf circulation can be described by the relationship between the across-shelf transport and the applied stress that drives it. Starting from a linear, layer-integrated along-shelf momentum balance:

$$\frac{\partial V}{\partial t} + fU = -\frac{1}{\rho_o}\frac{\partial P}{\partial y} + \frac{\tau_s^y}{\rho_o} - \frac{\tau_b^y}{\rho_o} \tag{2.1}$$

where V, U, and P are the layer integrated along-shelf velocity, across-shelf velocity, and pressure, ρ_o is a reference density, and τ_s^y and τ_b^y are the applied stresses at the surface (s) and the bottom (b) of the layer. Assuming steady flow with no pressure gradient or bottom friction, equation (2.1) reduces to the Ekman transport equation:

$$U = \frac{\tau_s^y}{\rho_o f} \tag{2.2}$$

defined as the across-shelf transport balanced by the applied surface stress divided by a reference density and the Coriolis parameter (Ekman, 1905). In shallow waters, where this Ekman transport is not fully developed, the relationship can be further approximated using a linear regression as (Lentz, 2001):

$$U = a\frac{\tau_s^y}{\rho_o f} + b \tag{2.3}$$

with a, the slope of the line, defining the fraction of full Ekman transport present while b, the y-intercept, is the transport at zero wind stress. Using this relationship for the surface Ekman layer, and a similar one for the bottom layer, we can calculate how measured surface and bottom transports compare with the full theoretical Ekman transports computed from the surface and bottom stresses.

Evaluating (2.3) is best handled using a neutral regression technique (Garrett and Petrie, 1981). While a normal linear regression technique minimizes the variance in one dimension, a neutral regression minimizes the variance in both dimensions. Here, the regression coefficient (a) is defined as the square root of the ratio of the variance of the second time series to the variance of the first time series, or:

$$a = \left(\frac{\sigma_2^2}{\sigma_1^2} \right)^{1/2} \tag{2.4}$$

More complex methods for computing this regression exist (e.g., Reed (1992)), however these methods differ from (2.4) only if known measurement uncertainties are used to compute the required weighting functions. If the variance of the input time series are used as weights, a reasonable assumption if measurement uncertainties are not known (Reed, 1992), this method collapses to the simple ratio used by Garrett and Petrie (1981).

Using these methods we can define the offshore extent of Ekman divergence using the theoretical Ekman transport given by (2.2) and the measured Ekman transports derived from the velocity observations (see next section). Here, the neutral regression coefficient is the square root of the ratio of the measured Ekman transport (time series 2) to the theoretical Ekman transport (time series 1).

2.2.3 Calculating Ekman transports

Measured Ekman transport

For each deployment, estimates of the across-shelf transport in the surface and bottom Ekman layers were calculated from the across-shelf velocity profiles obtained from the ADCPs. As ADCPs do not sample the entire water column, the across-shelf velocity profiles were extrapolated to the surface and bottom in order to compute across-shelf transports occurring throughout the water column. For the COAST 50-m deployments in 2001, velocity observations below 40 m and above 6 m depth were excluded because of

quality control concerns (Boyd et al., 2002). For station IS in 1999, velocity observations below 40 m and above 8 m were excluded from the velocity profiles (Boyd et al., 2000).

Similar 'tide-independent' quality control analysis at the PISCO deployment locations would exclude up to 1/3 of the water column at high tide due to larger tidal height variations at these shallow locations. Therefore, profiles of the total acoustic backscatter intensity were used to create 'tide-following' velocity profiles for all of the 30, 15, and 8-m ADCP deployments. Produced for each ensemble by summing the backscatter intensity profiles of all 4 beams, the depth of the maximum total backscatter intensity was marked as the water surface. Velocities from all depth bins above this surface were masked. An additional surface bin of the measured water velocities was subtracted from the masked profiles at 8 and 15-m locations due to side lobe reflection (Gordon, 1996). For the same reason, an additional 3 surface bins were subtracted from the 30-m location velocity profiles. All further analysis was performed on hourly-averages of the tide-following velocity profiles from the PISCO deployments and the quality controlled 50-m deployments mentioned above.

Possible sources of error in ADCP measurements include both random error and a bias due to surface gravity wave orbital velocities. RDI literature (Gordon, 1996) estimates the random error in the velocity measurements as the standard deviation of the difference in the vertical velocity estimates made by the two beam pairs. This 'error' velocity can then be estimated for each depth bin measured for each deployment. Error velocities averaged 0.01 m s^{-1} for all PISCO deployments and less than 0.01 m s^{-1} for the COAST and NOPP deployments (Boyd et al., 2000, 2002). In addition, because most deployments were in relatively shallow water, the inclusion of partial periods of the dominant surface gravity waves in the 2-minute ensemble averages might cause a bias in the velocity estimates. An estimate of this type of bias can be made considering the particle motion of a 1 m amplitude linear wave. Based on these parameters the estimated bias

ranged from 0 to a maximum of 0.025 m s^{-1} for wave periods from 4 to 20 s. In 15 m of water, the range of the maximum possible bias with depth was less than 0.01 m s^{-1}. Thus the bias is a strong function of wave period but a weaker function of depth below the surface, as the majority of the bias is absorbed into the depth-averaged mean velocity. Since we are only concerned with the depth-dependent component of the water velocities, the maximum possible bias due to surface gravity waves is of similar magnitude as the random error given above.

The principle axis coordinate system was used for velocity observations presented here. The principal axis of flow is that which minimizes the velocity variances in the minor axis. For most deployments, orientations of the axes ranged from 4 to 13° clockwise from North (Table 2.1), with notable exceptions located primarily at station FC. In general, the principal axes are aligned with local bathymetric contours. After rotation into the principal axis coordinate system, the velocity profiles were considered to be in along-shelf and across-shelf coordinates. Across-shelf transports were then found from the across-shelf components of the measured water velocity profiles.

To compute transports based on the full water column, a number of extrapolation techniques were considered. The simplest method, vertically extrapolating to the surface and the bottom assuming a constant velocity between the nearest measurements and the boundary, was attempted for all deployments (Figure 2.4). For 8-m and 15-m deployments, 1 m of extrapolation was needed at the surface and 2 m at the bottom. For the 30-m deployments, velocities were extrapolated 3 m at the surface and 2 m at the bottom. Extrapolated distances at 50 m were much larger as noted earlier. For the 8-m and 15-m deployments, only the constant velocity method was considered because the extrapolated distances were small. Given the larger distances between the nearest measurements and the surface or bottom at the 30-m and 50-m locations, two alternative profiles were considered. The first assumed a constant velocity slope between the two highest measure-

ments and the water surface for the top portion, and a constant velocity slope between the deepest velocity measurement and 0 m s^{-1} at the bottom (Figure 2.4). However, it is possible that the true shape of the velocity profiles includes a surface mixed layer with no vertical shear (Lentz, 1992). Thus, the second alternative was a combination of the constant velocity extrapolation to surface and the constant slope extrapolation to the bottom (Figure 2.4). After extrapolation, the depth-averaged mean of the across-shelf circulation was removed from all deployments to isolate the depth-dependent across-shelf circulation.

In this analysis, the flow field was assumed to be two dimensional and uniform in the along-shelf direction. The inner shelf off the coast of central Oregon is relatively along-shelf uniform in nature (Figure 2.1 and 2.2). While the large Heceta Bank in the southern part of the region influences circulation at depths greater than 50 m, there is little variation in along-shelf bathymetry at depths less than 50 m (Figure 2.2). However, small scale coastal topography could become an influencing factor in areas immediately adjacent to the coastline (Figure 2.1). If the two-dimensional assumption used in this calculation is valid, the total across-shelf transport caused by wind-forcing should have zero mean. Therefore, the depth-averaged portion of the across-shelf transport is expected to be small and uncorrelated with the wind. This criterion will be tested in Section 3.

From the resulting zero-mean hourly profiles for each deployment, the surface transport was found by vertically integrating from the surface down to the first zero crossing of the profile (Figure 2.4). Similarly, the bottom transport was found by vertically integrating from the bottom up to the lowest zero crossing available. These integrated transports form the measured surface and bottom transports used in the calculation. This method has been used previously for both inner shelf (Lentz, 2001; Austin and Lentz, 2002) and outer shelf (Allen et al., 1995), analysis.

Theoretical Ekman transport

Estimates of the surface and bottom stresses were used to calculate the theoretical Ekman transports in each layer using equation (2.2). For all deployments, a reference density of ρ_o=1025 kg m^{-3} and a Coriolis parameter of f=1.03x10^{-4} s^{-1} corresponding to a latitude of 45° are used. The along-shelf wind stress was calculated from observed wind velocities at each measurement location described earlier. The hourly averages of all available wind measurements were rotated into the principal axes coordinate system defined for each ADCP deployment. These estimates of along-shelf and across-shelf wind velocities were used to compute wind stress in the along-shelf direction using the empirical method given by Large and Pond (1981):

$$\tau_s^y = \rho_a C_f |\vec{v}| v \tag{2.5}$$

where ρ_a = 1.25 kg m^{-3} and C_f, the frictional drag coefficient, is a function of wind speed as well as the height of the measurement. All measurements were translated to 10 m height wind velocities and wind stresses using the assumption of a stable atmosphere (Large and Pond, 1981).

Using the neutral regression technique outlined above, the along-shelf wind stress observed offshore at buoy 46050 during each summer was compared with wind stresses from the Newport CMAN station and the mid-shelf meteorological moorings in 1999 and 2001 to find the most representative wind for each deployment. Curiously, the magnitude of the buoy 46050 along-shelf wind stress matched by the CMAN station varies somewhat year-to-year (Table 2.2). In 1999, 2001, and 2003, CMAN station along-shelf wind stress was ∼80% of the wind stress found offshore at buoy 46050. However, in 2002 wind stress at the CMAN station was closer (∼90%) to the wind stress at the offshore buoy. In 1999 and 2001, the regression of the mid-shelf winds to the offshore buoy winds is similar in magnitude to the regression between CMAN winds and buoy winds. In fact, winds at

mid-shelf locations were found to be statistically equal to CMAN winds at Newport.

From the comparisons shown, the CMAN station winds should be most representative of local winds at the 8, 15, and 30-m mooring deployments during the summer periods of interest and will be used in this analysis for those stations (Table 2.2). Further, given the high correlation between mid-shelf winds and CMAN winds in both 1999 and 2001, for continuity the CMAN winds will be used for the 50-m deployments as well.

While these regressions give estimates of across-shelf curl of the along-shelf wind stress, the average across-shelf wind stress curl along the Oregon coast was also computed. Curl-driven upwelling can be a significant part of the total upwelling (Picket and Paduan, 2003), yet as stated earlier, Samelson et al. (2002) reported a small wind stress curl off central Oregon. With a maximum computed across-shelf curl of 10^{-6} N m^{-3}, our calculations agree with these conclusions. In addition, most of the wind stress curl found occurred offshore of the mid-shelf moorings at 80 m depth (Table 2.2). This is an important result, as it implies that a divergence of Ekman transport inshore of 80 m depth is most likely caused by coastal upwelling rather than curl-driven upwelling. For these reasons, wind stress curl is not considered to be an important factor here.

The along-shelf bottom stress was approximated, following Lentz (2001) as:

$$\tau_b^y = \rho_o r v_b \tag{2.6}$$

where v_b is taken as the along-shelf bottom velocity (i.e., the deepest measured along-shelf velocity during each deployment), and r is the frictional coefficient. A value of r=5x10^{-4} m s^{-1} was used here based on previous mid-shelf observations (Lentz, 2001; Lentz and Winant, 1986). While a quadratic stress parameterization is thought to be more appropriate in and near the surf zone (Feddersen et al., 1998), initial tests found correlations of measured and theoretical transports calculated using linear bottom stress were not significantly different than correlations of measured and theoretical transports

calculated using quadratic bottom stress. Thus for simplicity, quadratic bottom stress was not considered here. In contrast, the success of the bottom transport fraction calculation is quite sensitive to the frictional coefficient used. This parameter is evaluated further in Section 3.2.

Finally, prior to performing the neutral regression both the measured and theoretical transports were low pass filtered using a filter with a 40-hr cut-off (Mooers, 1968) in order to isolate the sub-tidal portions of the transport calculations. The 95% confidence level is used to establish significant correlations and confidence intervals throughout the results shown below.

2.2.4 Hydrographic observations

Hydrographic observations from moorings adjacent to each 15-m ADCP location were used in this study to examine the role of stratification on across-shelf transport. A typical mooring at 15 m in the PISCO mooring program consists of temperature measurements at 1, 4, 9, and 14 m, with additional temperature and salinity measurements at 8 m. All temperature and salinity records were low pass filtered using the method described above to isolate the sub-tidal frequencies of variability. However, the PISCO data set lacks adequate vertical salinity coverage to compute stratification using the top to bottom density difference. Therefore, the difference between the surface and bottom temperature sensors, divided by the distance between them, is used as a proxy for the stratification. The majority (60%) of surface temperature values were from 1 m depth. When 1-m measurements were not available, temperature measurements from 4 m depth were substituted. The validity of using the temperature gradient as a proxy for the density stratification is discussed in Section 4.4.

2.3. Results

2.3.1 Transport results

Using the methods described above, the measured and theoretical transports for both the surface and bottom layers were calculated for each deployment and then compared using the neutral regression technique. The results of this regression indicate the fraction of theoretical surface or bottom Ekman transport present, and results from all deployments are listed in Table 2.3. Significant results are defined here as those deployments where the measured and theoretical transports are positively correlated, while the wind stress and the depth-averaged velocity are uncorrelated. Both criteria indicate that the assumption of along-shelf uniformity is valid for the wind-driven circulation. Based on these conditions, significant results were found for the majority of the 17 deployments (Table 2.3). The necessary criteria were met for the surface layer at ten 15-m deployments, one 30-m deployment, and all 50-m deployments. Significant results for the bottom layer were found only during nine 15-m deployments and two 50-m deployments. It is of interest to note that both 8-m locations failed the necessary conditions for significance. Many of the intercepts, b, were not significantly different than zero, indicating that across-shelf transport was small in the absence of stress. Among the significant results, b increases moving offshore in the surface layer from an average of 0.05 $m^2\ s^{-1}$ at 15 m to 0.2 $m^2\ s^{-1}$ at 50 m. In the bottom layer, mean transports are in the opposite direction, increasing offshore from 0.02 $m^2\ s^{-1}$ at 15 m to 0.12 $m^2\ s^{-1}$ at 50 m. These transports represent processes in the momentum balance (2.1) that we've assumed to be small (e.g. along-shelf pressure gradients or accelerations), the importance of which apparently increases moving offshore. However, as our focus is on wind-driven across-shelf circulation, these non-wind-driven mean transports will not be discussed further.

Comparing the different methods of extrapolation used for the 30-m and 50-m deployments showed the following. At the two 30-m locations, the average difference in

transport fractions between the 3 methods was less than 3%. Thus, only results using constant velocity extrapolation profiles are included in Table 2.3 for simplicity. At the three 50-m locations, transport fractions found using the two alternative profiles differed from the constant velocity extrapolation profiles by an average of 30%. Results from the constant velocity extrapolation profiles themselves were quite variable. Using this profile, surface fractions ranged from 70 to 109% while the two significant bottom fractions were 100 and 160% respectively (Table 2.3). Results from the constant slope extrapolation profiles consistently over-estimated the fraction of full Ekman transport present in the surface layer with all three deployments over 120%. The significant bottom transport fractions using the constant slope extrapolation method were 91% and 160% (Table 2.3). Results from the combined extrapolation method (constant velocity at surface, constant slope at bottom) follow those above: surface fractions were similar to the constant velocity method while bottom fractions were similar to those from the constant slope method. The high surface fractions from the constant slope extrapolation overestimate the full transport present as a result of the extrapolation method used. Both alternative methods show that the constant slope extrapolation in the bottom layer yields transport fractions only slightly different than the constant velocity extrapolation results. For these reasons, only results from the constant velocity extrapolation profiles are considered further.

Using the significant results only (Table 2.3, Figure 2.5), the measured surface Ekman transport ranged from 18% to 35% of the full theoretical Ekman transport at 15 m. Measured bottom transport fractions at this depth were more variable, ranging from 25% to 70% of the full theoretical bottom Ekman transport. The surface fraction from the one significant 30-m deployment in 2002 was 55% of the full theoretical transport. Finally, as stated earlier, surface fractions at 50-m deployments ranged from 70% to 109% while bottom fractions were 100% and 160%. Viewed as a whole (Figure 2.5), the results from all significant deployments begin to describe the relationship between the Ekman frac-

tions and the local water depth. In general, these results show the fraction of theoretical Ekman transport increases with offshore depth, becoming near full-Ekman transport at the deepest deployment depth, 50 m. A linear fit to the surface fractions of the significant deployments increases offshore from 25% at 15 m to 90% at 50 m. A similar fit of the significant bottom fractions increases from 45% at 15 m to 130% at 50 m, although there is considerably more variability in the bottom transport fractions at both depths.

As the bulk of the deployments were at water depths of 15 m, results at these locations are discussed further. At all 15-m stations except station YH, calculated bottom transport fractions were consistently larger than their corresponding surface transport fractions (Figure 2.6). Bottom transport fractions were an average of 1.2 and 2.1 times the surface transport fractions at stations SR and SH, 1.3 at LB, 2.5 at CH, and 2.2 at station FC while only 0.88 at YH (Table 2.3). Of those stations with multiple significant results in each layer, transport fractions at station FC are variable while fractions at stations SR and SH are quite steady over time. The larger bottom fractions seen here and the influence of stratification on the transport fractions are discussed in the following sections.

2.3.2 Effects of bottom stress parameterization

Assuming that the wind-driven flow is two dimensional and steady with no along-shelf pressure gradient, the depth-integrated along-shelf momentum balance is between the surface and bottom stress terms only. If this is true, the surface and bottom transport fractions should balance as well. However, results shown above give bottom fractions that are generally higher than surface fractions. In these cases, the bottom stress calculated using a frictional coefficient of r=5x10^{-4} m s^{-1} was less than the surface stress calculated using Large and Pond (1981) empirical relationship. Here we compute the frictional coefficient needed for bottom stress to balance surface stress by forcing the surface and bottom transport fractions to balance.

Using equations (2.2), (2.4), and (2.6) with the above assumption that the bottom transport fraction should equal the surface transport fraction,

$$\frac{var(U_b)}{R^2} = var\left(r\frac{v_b}{f}\right) \tag{2.7}$$

where: $var()$ denotes a variance operation, U_b is the measured bottom transport, R is the surface transport fraction, and v_b is the bottom velocity. From this relationship, a new friction coefficient r can be found iteratively. This calculation was performed on all results, and the resulting frictional coefficients are given here as a function of both station and year (Table 2.4) and of local water depth (Figure 2.7). At most deployments the calculated coefficients are greater than the original value of r=5x10^{-4} m s^{-1}. A linear fit to the calculated frictional coefficients increases slightly with decreasing depth from 7x10^{-4} at 50-m depth to 9x10^{-4} at 15-m depth. At 50 m, the new value of r is close to the initial value used, while an average 1.7 times the original value is needed at 15 m. However, the range of the calculated coefficients at 15 m is quite large, spanning an order of magnitude. The variability of r could be due to terms in momentum balance we've neglected here, however the increase of r with decreasing water depth is consistent with an increase in bottom stress due to the effect of surface gravity waves in the bottom boundary layer (Grant and Madson, 1979).

2.3.3 Influence of Stratification

As mentioned earlier, observations and model studies indicated reduced Ekman transport at lower levels of stratification. Decreasing stratification acts to thicken the boundary layers, as stratification affects the eddy viscosity in the Ekman velocity derivation (Allen et al., 1995; Austin and Lentz, 2002). Because the surface and bottom boundary layers overlap in the inner shelf, changes in stratification should have a direct effect on the fraction of full Ekman transport present.

A simple example of decreases in the fraction of full Ekman transport occurring at the same time as reductions in stratification was observed at station YH, a 15-m deployment made in 1999. Using the top-to-bottom temperature gradient as a proxy for the density stratification, the stratification decreased over the deployment period (Figure 2.8). The effect of stratification on the across-shelf transport is apparent if we divide the transport results into two regimes, an initial stratified regime and a more weakly stratified regime occurring after early September (yearday 250), and then perform the neutral regression analysis described earlier on both halves. With a mean gradient of 0.19 °C m^{-1}, in the stratified regime the surface transport fraction was 38% while the bottom transport fraction was 33%. In contrast, during the weakly stratified regime, with a mean gradient of 0.09 °C m^{-1}, both the surface and bottom transport fractions were reduced to 31% and 24% respectively.

To test this hypothesis further, the fraction of full transport and average stratification were compared over shorter time intervals for the surface layers of all 15-m deployments. The measured and theoretical Ekman transports were used to compute the transport fractions in incremental 6-day blocks. Then the transport fractions were compared to the average stratification of each time block. A scatter-plot (Figure 2.9) of the average stratification and surface transport fraction time series from all deployments suggests a weak linear dependence. A neutral regression of the surface transport fraction and average stratification time series gives a slope and intercept of 2.5 and near 0 respectively. Thus, using the full surface layer data set yields a stronger dependence of transport fraction on stratification than in the single YH 15-m example (Figure 2.8).

2.4. Discussion

The results of the Ekman transport calculation presented above clearly illustrate the offshore divergence of Ekman transport in the inner shelf off Oregon. The wind-driven dynamics that control circulation offshore appear to extend inshore with a magnitude adjustment based on the divergence of Ekman transport along a coastal boundary. Yet the role of wind stress curl in this process and the wind-driven dynamics in water less than 15 m depth deserve further discussion. In addition, we compare these results to previous studies and discuss the validity of using temperature differences as a proxy for density stratification on the inner shelf.

2.4.1 Wind stress curl

In contrast to a number of previous studies, wind stress curl is unlikely to be a significant cause of upwelling in the inner shelf off central Oregon. As shown here, CMAN station winds were at least 80% of the magnitude of winds measured offshore at buoy 46050. Small across-shelf and along-shelf curl were also reported by Samelson et al (2002) for our study area. In contrast, Lentz (1994) reported large wind stress curl for the CODE region off northern California. In that region, along-shelf wind speeds 1 km offshore (at 30-m depth) were 1/3 the magnitude of along-shelf wind speeds 8 km offshore (at 90-m depth) (Lentz, 1994). Our results also contrast with the recent model results of Ekman transport and pumping given by (Picket and Paduan, 2003) for the continental shelf off central California where pumping caused a significant fraction of the total upwelling velocity. The differences from this study are twofold. First, Picket and Paduan (2003) measured significant wind stress curl (up to 10^{-5} N m^{-3}) within 50 km of the coast, highest downwind (equatorward) of coastal promontories. Off Oregon, the maximum across-shelf curl measured here was much less at $\sim 10^{-6}$ N m^{-3} (Table 2.2). Second, Picket and Paduan (2003) used a Rossby radius of 10 or 20 km to convert Ekman transports into upwelling

velocities. The resulting vertical velocity was found to be of the same order as the Ekman pumping velocity which peaks at about 25 km offshore. As shown here from the Ekman divergence off central Oregon, upwelling is fully realized by a water depth of 50 m or 4-5 km offshore (Figure 2.2). This value is significantly shorter than the 10-20 km used by Picket and Paduan (2003) and would result in higher vertical velocities.

2.4.2 Comparing with previous results

Comparing the transport fraction results presented here with those reported by (Lentz, 2001) for the wide North Carolina shelf indicates a dynamical similarity between the two regions. Overlaying the two series (Figure 2.5), the results from North Carolina fall close to those from Oregon in both layers but have consistently higher surface transport fractions. These similarities are notable given the large difference in shelf geometry. Off Oregon, 15-m moorings were 1 km offshore while 50-m locations were about 5 km offshore. In contrast, off North Carolina, the 13-m site was 1.6 km offshore while the 60-m site was 77 km offshore. Thus, results from the two areas collapse when compared by water depths, but are quite different when compared by offshore distance. In addition, the 5 km offshore extent of Ekman divergence found here is half the value reported by Huyer (1983) using mid-shelf measurements made off central Oregon.

Using combination of current meters and ADCPs, Austin and Grantham (in progress) reported across-shelf transport fraction results for additional PISCO mooring locations in 1999 and 2000. With a similar method, the authors found surface transport fractions at station SH of 25% and 16% in 1999 and 2000 respectively. Their results concur with those seen here, indicating the steady nature of the wind-driven dynamics at this station over the course of six summers. However, like those reported here, fractions from station FC were quite variable. The variability seen at station FC will be discussed in the next section.

2.4.3 Calculation failures

Given the across-shelf divergence of Ekman transport found on the Oregon inner shelf and its similarities to the across-shelf transports observed elsewhere, those deployments that failed to meet the necessary conditions are of further interest as they raise questions about the assumptions used in this analysis. Notable failures of the transport calculations occurred in all measurements taken at 8-m locations and at more than half the deployments made at station FC. These deployments failed as either the measured transports were uncorrelated with the stresses or a significant wind-driven depth-averaged across-shelf velocity component existed. Again, positive correlations of the measured transports and stresses as well as no significant correlation between the surface stress and the depth-averaged across-shelf velocity are necessary conditions of the theory used here.

We suggest that the influence of local bathymetry is responsible for the failure of the transport calculations at station FC. The rotation of the principal axis of flow with depth for deployments at station FC are significantly higher than any other station. The range of principal axis orientations spanned 80° and 71° for the 2001 deployments at 15 and 8 m, 43° and 21° for the 2002 15-m deployments, and 43° for the 30-m deployment in 2002 (Table 2.1). Comparatively, the 30-m deployment at station SH had a total range of 10° (Table 2.1). A wide range of turning with depth (40-70 degrees) in 15 m indicates the assumption of along-shelf uniformity and two-dimensional flow might not be valid at this location. Indeed, station FC is located just north of a headland (Figure 2.1), possibly causing this variability. In contrast, station LB located a few kilometers farther north in a region of smoother topography has a principal axis range of only 7°. Further, correlations of the depth-averaged along-shelf velocities from all years (not shown here) found that currents at station FC were poorly correlated with all other stations, even though stations to the north and south were well correlated. These results indicate that a systematic difference between station FC and stations both to the north and south exists, most likely

the result of local bathymetry.

In addition to the transport calculation failure for the FC 8-m deployment, inconsistent results occurred for the SH 8-m deployment as well. Given the shallow water depth of these deployments, a large fraction of the water column (37%) was not measured by the instruments. Velocities in these regions (2 m at bottom and 1 m at top) were assumed by extrapolation and remain a possible source of error in the transport calculation. In addition, we hypothesize that these mooring locations were frequently in the surf zone where wave-induced radiation stresses can be a dominant force. If true, root mean squared wave heights (H_{rms}) must be large enough to cause wave breaking and dissipation at the mooring location, resulting in non-zero wave radiation stresses in the depth-averaged along-shelf momentum balance. During the period of the 8-m deployments, H_{rms} wave heights measured offshore at buoy 46050 averaged 2 m with peak waveheights exceeding 3-4 m. With similar H_{rms} waveheights, Lentz et al. (1999) observed the surf zone extending past an 8-m mooring location on a number of occasions off North Carolina. Even though appropriate measurements (i.e., wave direction) to fully investigate this point were not made in our study, the results raise questions about the exact nature of the across-shelf transport that occurs between the surf zone and the inner shelf.

2.4.4 Temperature difference and stratification

Our analysis links the level of stratification to the across-shelf transport fractions using the top to bottom temperature difference, divided by the depth between them, as a proxy for the actual density stratification present. However, density over the Oregon shelf is also a strong function of salinity. Thus, it is necessary to determine how well temperature works as a proxy for density. If temperature changes throughout the water column are well correlated with salinity changes, we would have reason to assume that temperature is a good predictor of density.

Where we have salinity measurements (8-m depth at each 15-m mooring), salinity

is strongly negatively correlated with temperature (Table 2.5). Further, correlating the 8-m salinity with temperature measurements from all available depths showed that temperatures throughout the water column were negatively correlated with the 8-m salinity at most locations (Table 2.5). In fact, only a few examples exist in the data where the surface temperature is not significantly correlated to the 8-m salinity. While surface heating might be a factor in these few examples, this simple test indicates that temperature and salinity generally fluctuate together over the entire water column at these shallow inner-shelf stations. CTD casts (not shown here) made by the PISCO program adjacent to most mooring locations further support this result. In most casts, observed temperature and salinity gradients are co-located with warm, fresh water overlaying cold, salty waters. Therefore, the top-to-bottom temperature difference used here is a valid proxy for the density stratification present over the inner-shelf during summer.

2.4.5 Implications for larval transport and phytoplankton blooms

Our results have several ecological implications. The first is that our data suggest across-shelf transport of materials such as larvae and phytoplankton may be minimal inshore of about 15-m depth. Two observations are consistent with this interpretation. Barnacle (*Balanus glandula* and *Chthamalus dalli*) recruitment varies little with latitude along the stretch of coast encompassed by the PISCO mooring array (Menge et al., 2002). In the context of the present results that indicate little across-shelf Ekman transport occurs inshore of 15 m depth, barnacle larvae released into inner-shelf waters may be retained there rather than being swept far offshore as has been suggested for California coastal waters (Roughgarden et al., 1998; Farrell et al., 1991). Since we find no evidence for a latitudinal pattern in the across-shelf width of the divergence of Ekman transport, if barnacle larvae tend to remain within or inshore of this band, no latitudinal trend in barnacle recruitment would be expected.

A second observation consistent with our interpretation is the regular observation of

sharp color fronts between the near shore and waters 1-2 km offshore. We have regularly observed these fronts on PISCO cruises and other work in the region. Water samples from shore and ship-based surveys indicate that the difference in color is caused by dense coastal phytoplankton blooms (that color the water brown) abutting offshore waters (green in color) with much lower phytoplankton concentrations. Whether or not this front represents the outer edge of the region our physical measurements have identified as the region of reduced across-shelf transport in the inner shelf is not known and bears further investigation.

Finally, observed recruitment patterns suggest that the link between across-shelf transport and larval dispersal (or retention) in the inner shelf may vary at a larger latitudinal scale. Data on geographic variation in barnacle recruitment indicates that, in contrast to the minimal variation in recruitment seen along the central Oregon coast, recruitment varies enormously between regions north and south of Cape Blanco, on the southern Oregon coast (Connolly et al., 2001; Menge et al., 2004). Recruitment rates are high north of Cape Blanco, while south of the Cape and throughout California, recruitment rates are significantly lower. These data and the results of this study imply that a fundamental difference in the link between across-shelf transport and larval dispersal (e.g. differences in the near-shore stratification or wind-stress patterns) exists north and south of the Cape, causing higher offshore losses of larvae to the south. This hypothesis deserves further research.

2.5. Conclusions

The fraction of the full theoretical Ekman transport present in the wind-driven across-shelf circulation over the Oregon inner shelf increased from 25% of full Ekman transport at 15-m depth (1-2 km offshore) to full Ekman transport near 50-m depth (5-6

km offshore). In general, transport fractions were found to be locally steady at those stations occupied for multiple years. The assumption of along-shelf uniformity was found to hold at most locations and velocities at these stations were well correlated along the coast. At station FC, the consistent exception to most results reported here, velocity profiles from all deployments exhibit significant turning of the principal axis of flow with depth. This indicates flow at this location is significantly influenced by local along-shelf bathymetric variations, causing deviations from theoretical Ekman predictions.

The preliminary drag coefficient assumed here in the linear bottom stress parameterization resulted in bottom transport fractions that were consistently higher than surface transport fractions. Adjusting this coefficient to balance the bottom and surface transport fractions resulted in slightly higher drag coefficients that increased in magnitude moving onshore. This increase is consistent with higher drag nearshore due to surface gravity wave effects on the bottom boundary layer.

The fraction of full Ekman transport as a function of water depth found here is similar to that reported by (Lentz, 2001) for the wide North Carolina coast. Thus the region of Ekman divergence is dependent on local water depth rather than offshore distance. Additionally, a comparison of the 6-day average stratification and surface transport fractions showed that the level of stratification was weakly correlated with and linearly related to the fraction of across-shelf transport. A reduction of stratification would act to thicken the boundary layers and increase the boundary layer depth overlap in shallow waters by increasing the eddy viscosity. This process was suggested by Lentz (2001) and modeled by Austin and Lentz (2002) as leading to a shutdown of the inner-shelf circulation. Finally, reduced across-shelf transport in the inner shelf could suppress the connection between the shore and the mid shelf, leading to retention of organisms within the inner shelf.

2.6. Acknowledgments

The authors would like to acknowledge the David and Lucile Packard Foundation for its support of the PISCO mooring program at OSU. M. Levine and T. Boyd generously provided the NOPP (Office of Naval Research Grant N00014-98-1-0787) and COAST (National Science Foundation Grant OCE-9907854) 50-m mooring and meteorological data used in this analysis. We thank M. Levine and J. Austin (of Old Dominion University) for helpful discussions. This work was supported in part by NSF Grant OCE-9907854. This paper is PISCO contribution #161.

BIBLIOGRAPHY

Allen, J., P. Newberger, and J. Federick, 1995: Upwelling circulation on the Oregon continental shelf, part 1: Response to idealized forcing. *J. Phys. Ocean.*, **25**, 1843–1866.

Allen, J. and R. Smith, 1981: On the dynamics of wind-driven shelf currents. *Phil. Trans. R. Soc. Lond.*, **A302**, 617–634.

Austin, J. and B. Grantham, in progress: Subinertial variability of the Oregon inner shelf. *J. Geophys. Res.*.

Austin, J. and S. Lentz, 2002: The inner shelf response to wind-driven upwelling and downwelling. *J. Phys. Ocean.*, **32**, 2171.

Boyd, T., M. Levine, P. Kosro, and S. Gard, 2000: Mooring observations from the Oregon continental shelf: April-September 1999. *Oregon State University Data Report*, **177**.

Boyd, T., M. Levine, P. Kosro, S. Gard, and W. Waldorf, 2002: Observations from moorings on the Oregon continental shelf: May-August 2001. *Oregon State University Data Report*, **190**.

Connolly, S., B. Menge, and J. Roughgarden, 2001: A latitudinal gradient in recruitment of intertidal invertebrates in the northeast Pacific ocean. *Ecology*, **82**, 1799–1813.

Ekman, V., 1905: On the influence of the Earth's rotation on ocean-currents. *Arkiv. Math. Astro. Fys.*, **2**, 1–53.

Farrell, T., D. Bracher, and J. Roughgarden, 1991: Cross-shelf transport causes recruitment to intertidal populations in central California. *Limnol. Oceanogr.*, **36**, 279–288.

Feddersen, F., R. Guza, S. Elgar, and T. Herbers, 1998: Alongshore momentum balances in the nearshore. *J. Geophys. Res.*, **103**, 15667–15676.

Garrett, C. and B. Petrie, 1981: Dynamical aspects of the flow through the strait of Belle Isle. *J. Phys. Ocean.*, **11**, 376–393.

Gill, A., 1982: *Atmosphere-ocean dynamics*. Academic Press, 666 pp.

Gordon, R., 1996: *Acoustic Doppler Current Profiler: principles of operation, a practical primer Second edition for Broadband ADCPs*. RDI Instruments, 54 pp.

Grant, W. and O. Madson, 1979: Combined wave and current interaction with a rough bottom. *J. Geophys. Res.*, **84**, 1797–1808.

Hickey, B., 1998: Coastal oceanography of western North America from the tip of Baja California to Vancouver island. *The Sea, v11*, A. Robinson and K. Brink, eds., John Wiley and Sons, chapter 12, 345–393.

Huyer, A., 1983: Coastal upwelling in the California Current System. *Prog. Oceano.*, **12**, 259–284.

— 1990: Shelf circulation. *The Sea, v9a*, B. LeMehaute and D. Hanes, eds., John Wiley and Sons, chapter 12, 1647–1658.

Large, W. and S. Pond, 1981: Open ocean momentum flux measurements in moderate to strong winds. *J. Phys. Ocean.*, **11**, 324–336.

Lentz, S., 1992: The surface boundary layer in coastal upwelling regions. *J. Phys. Ocean.*, **22**, 1517–1539.

— 1994: Current dynamics over the northern California inner shelf. *J. Phys. Ocean.*, **24**, 2461–2478.

— 1995: Sensitivity of the inner-shelf circulation to the form of the eddy viscosity profile. *J. Phys. Ocean.*, **25**, 19–28.

— 2001: The influence of stratification on the wind-driven cross-shelf circulation over the North Carolina shelf. *J. Phys. Ocean.*, **31**, 2749–2760.

Lentz, S., R. Guza, S. Elgar, F. Feddersen, and T. Herbers, 1999: Momentum balances on the North Carolina inner shelf. *J. Geophys. Res.*, **104**, 18205–18226.

Lentz, S. and J. Trowbridge, 1991: The bottom boundary layer over the northern California shelf. *J. Phys. Ocean.*, **21**, 1186–1200.

Lentz, S. and C. Winant, 1986: Subinertial currents on the southern California shelf. *J. Phys. Ocean.*, **16**, 1737–1750.

MacCready, P. and P. Rhines, 1993: Slippery bottom boundary layers on a slope. *J. Phys. Ocean.*, **23**, 5–22.

Menge, B., C. Blanchette, P. Raimondi, T. Freidenburg, S. Gaines, J. Lubchenco, D. Lohse, G. Hudson, M. Foley, and J. Pamplin, 2004: Species interaction strength: testing model predictions along an upwelling gradient. *Ecological Monographs*, **74**, 663684.

Menge, B., E. Sanford, B. Daley, T. Freidenburg, G. Hudson, and J. Lubchenco, 2002: An inter-hemispheric comparison of bottom-up effects on community structure: insights revealed using the comparative-experimental approach. *Ecological Research*, **17**, 1–16.

Mooers, C., 1968: A compilation of observations from moored current meters and thermographs, vol 2: Oregon continental shelf, August-September 1966. *OSU Data Report*.

Morgan, S. G., 2001: The larval ecology of marine communities. *Marine community ecology*, M. Bertness, S. Gaines, and M. Hay, eds., Sinauer Associates, Inc., 159–181.

Oke, P., J. Allen, R. Miller, G. Egbert, J. Austin, J. Barth, T. Boyd, P. Kosro, and M. Levine, 2002a: A modeling study of the three-dimensional continental shelf circulation off Oregon. Part I: model-data comparisons. *J. Phys. Ocean.*, **32**, 1360–1382.

— 2002b: A modeling study of the three-dimensional continental shelf circulation off Oregon. Part II: dynamical analysis. *J. Phys. Ocean.*, **32**, 1383–1403.

Picket, M. and J. Paduan, 2003: Ekman transport and pumping in the California current based on the U.S. Navy's high-resolution atmospheric model (COAMPS). *J. Geophys. Res.*, **108**, doi:10.1029/2003JC001902.

Reed, B., 1992: Linear least-squares fits with errors in both coordinates. *Am. J. Phys.*, **60**, 59–62.

Roughgarden, J., S. Gaines, and H. Possingham, 1998: Recruitment dynamics in complex life cycles. *Science*, **241**, 1460–1466.

Samelson, R., 1997: Coastal boundary conditions and the baroclinic structure of wind-driven continental shelf currents. *J. Phys. Ocean.*, **27**, 2645–2662.

Samelson, R., P. Barbour, J. Barth, S. Bielli, T. Boyd, D. Chelton, P. Kosro, M. Levine, and E. Skyllingstad, 2002: Wind stress forcing of the Oregon coastal ocean during the 1999 upwelling season. *J. Geophys. Res.*, **107**, doi: 10.1029/2001JC00900.

Small, L. and D. Menzies, 1981: Patterns of primary productivity and biomass in a coastal upwelling region. *Deep-sea Res.*, **28**, 123–149.

Smith, R., 1995: The physical processes of coastal ocean upwelling systems. *Upwelling and the ocean: modern processes and ancient records*, C. Summerhayes, K. Emeres, M. Angel, R. Smith, and B. Zeitzchel, eds., John Wiley and Sons, 39–64.

Winant, C., 1980: Downwelling over the southern California shelf. *J. Phys. Ocean.*, **10**, 791–799.

Year	Station	Depth(m)	Duration (days)	(μ_{east}	σ_{east}	μ_{north}	σ_{north}	θ_p	Range of θ_p
				(m s^{-1})					
1999	YH	15	67	-0.007	0.004	0.014	0.013	13	6
	IS	50	77	0.005	0.004	0.004	0.014	12	8
2001	CH_a	15	80	-0.012	0.003	-0.068	0.013	11	12
	CH_b	15	50	-0.014	0.003	-0.067	0.009	13	16
	NIS	50	104	-0.007	0.004	-0.011	0.017	9	3
	FC	08	100	-0.021	0.005	-0.015	0.004	-28	71
	FC	15	62	-0.0038	0.002	-0.017	0.007	5	80
	SH	08	46	-0.033	0.003	-0.081	0.017	7	1
	SH	15	63	-0.007	0.002	-0.077	0.014	6	4
	SIS	50	105	0.015	0.003	-0.013	0.011	5	10
2002	FC_a	15	62	-0.019	0.004	-0.001	0.008	22	43
	FC_b	15	33	-0.017	0.002	-0.001	0.005	22	21
	FC	30	51	-0.029	0.004	-0.001	0.014	13	43
	SR	15	115	0.002	0.002	0.002	0.012	4	15
	SH	15	111	0.000	0.002	-0.054	0.014	5	7
	SH	30	52	0.009	0.002	0.02	0.015	5	10
2003	LB	15	111	-0.02	0.005	-0.064	0.011	21	7
	SR	15	116	-0.002	0.002	0.000	0.012	5	9
	SH	15	122	-0.003	0.002	-0.049	0.015	5	8

TABLE 2.1: Location, depth, and duration of ADCP deployments made during the 1999, 2001, 2002, and 2003 PISCO OSU mooring program field seasons with the depth-averaged mean (μ in m s^{-1}) and standard deviation (σ in m s^{-1}) of both east and north velocities. 50-m deployments at stations IS, NIS, and SIS were obtained from the 1999 NOPP program (Boyd et al, 2000) and the 2001 COAST program (Boyd et al, 2002). Also included for each deployment are the calculated principal axis directions (θ_p, degrees clockwise from true north), and the range of principal axis directions with depth.

Year	Stations Compared	Yearday start	Yearday end	Fraction	CC	Cross-shelf wind stress curl $\bigtriangledown \times \tau^y$ (10^{-6} N m^{-3})
1999	buoy/cman	100	250	0.77±0.13	0.93	1.3
	buoy/midshelf	118	204	0.72±0.06	0.98	0.8
	midshelf/cman	118	204	1.09±0.17	0.93	0.4
2001	buoy/cman	136	241	0.77±0.17	0.93	0.7
	buoy/midshelf	136	241	0.68±0.09	0.96	1.2
	midshelf/cman	136	241	1.14±0.23	0.93	-0.3
2002	buoy/cman	100	250	0.91±0.14	0.87	0.4
2003	buoy/cman	100	250	0.79±0.13	0.87	0.4

TABLE 2.2: Comparison of along-shelf wind stress at buoy 46050, the Newport CMAN station, and the midshelf meteorological buoys from 1999 NOPP and 2001 COAST projects during summer (defined here as yearday 100-250) using the neutral regression technique. The correlation coefficients (CC) between each pair are also shown, with all correlations being significant at the 95% confidence level. As an example, regressing buoy 46050 and the CMAN station in 1999 yielded 0.77, meaning that the along-shelf wind stress at the CMAN station was 77% of the magnitude of the wind stress measured at buoy 46050 to the 95% confidence interval cited. Estimates of the average across-shelf wind stress curl (x10^{-6}) between the measurement locations for each year are included as well.

Year	Station	Depth (m)	Surface transport a	Surface transport b (m^2s^{-1})	Bottom transport a	Bottom transport b (m^2s^{-1})	ratio
1999	YH	15	0.34±0.086	0.05±0.030	0.27±0.073	0.00±0.028	0.79
	IS_{vel}	50	1.09±0.254	0.19±0.106	1.03±0.193	-0.11±0.082	0.95
	IS_{slope}	50	1.27±0.278	0.09±0.116	0.91±0.172	-0.05±0.079	0.72
	IS_{combo}	50	1.10±0.277	0.23±0.106	0.84±0.172	0.00±0.079	0.76
2001	CH_a	15	0.18±0.037	0.05±0.022	0.47±0.104*	-0.05±0.022*	
	CH_b	15	0.22±0.071	0.05±0.027	0.54±0.182	-0.04±0.032	2.45
	NIS_{vel}	50	0.69±0.247	0.19±0.114	0.51±0.120*	-0.22±0.064*	
	NIS_{slope}	50	1.36±0.484	0.09±0.222	0.62±0.148*	-0.28±0.082*	
	NIS_{combo}	50	0.64±0.230	0.18±0.106	0.62±0.148*	-0.22±0.082*	
	FC	08	0.08±0.021*	0.03±0.011*	0.94±0.150*	-0.02±0.010*	
	FC	15	0.15±0.032*	0.16±0.016*	2.50±0.436*	-0.15±0.013*	
	SH	08	0.08±0.020*	-0.03±0.011*	0.07±0.012*	0.02±0.008*	
	SH	15	0.22±0.0685	0.00±0.033	0.26±0.075	-0.01±0.030	1.18
	SIS_{vel}	50	1.03±0.362	0.24±0.167	1.61±0.635	-0.14±0.1616	1.56
	SIS_{slope}	50	1.31±0.453	0.13±0.209	1.60±0.583	-0.26±0.150	1.22
	SIS_{combo}	50	0.95±0.337	0.24±0.156	1.60±0.583	-0.26±0.150	1.28
2002	FC_a	15	0.23±0.067	0.02±0.030	0.67±0.168	-0.04±0.033	2.91
	FC_b	15	0.22±0.079	0.07±0.029	0.32±0.115	-0.09±0.030	1.45
	FC	30	0.75±0.251*	-0.19±0.120*	2.16±0.579*	0.18±0.109*	
	SR	15	0.38±0.107	0.04±0.052	0.68±0.189	0.06±0.050	1.89
	SH	15	0.23±0.063	0.01±0.031	0.28±0.077	-0.01±0.030	1.22
	SH	30	0.55±0.161	-0.02±0.080	0.77±0.223*	0.02±0.066*	
2003	LB	15	0.19±0.038	0.07±0.017	0.24 ±0.052	-0.07±0.017	1.33
	SR	15	0.29±0.073	0.02±0.036	0.70±0.176	0.04±0.033	2.38
	SH	15	0.24±0.054	0.03±0.026	0.28±0.079	-0.02±0.030	1.17

TABLE 2.3: Results of the Ekman transport fraction calculation. All fractions (a) and y-intercepts (b) are accompanied by their respective 95% confidence intervals. For 50-m deployments, results from all 3 extrapolation methods considered are included. Results marked with asterisks failed to meet the necessary criteria outlined in the text. The ratio of the bottom transport fraction to the surface transport fraction is included as the rightmost column for significant results only.

Year	Station	Depth (m)	Duration (days)	r (10^{-4} m s^{-1})
1999	YH	15	67	4
	IS	50	77	5
2001	CH	15	80	NA
		15	50	12
	NIS	50	104	NA
	FC	08	100	NA
		15	62	NA
	SH	08	46	NA
		15	63	6
	SIS	50	105	9
2002	FC	15	62	14
		15	33	7
		30	51	NA
	SR	15	115	9
	SH	15	111	6
		30	52	NA
2003	LB	15	111	7
	SR	15	116	12
	SH	15	122	6

TABLE 2.4: Calculated bottom friction coefficients found by matching the surface and bottom transport fractions. The coefficients are included only for those deployments where both the bottom and surface transport fractions meet the necessary conditions. Compared to the original value of r=5x10^{-4} m s^{-1}, the results of this calculation are larger and increase in magnitude with decreasing local depth.

Year	Stat. ID	Depth (m)	Length (days)	CC
1999	YH	3	44	-0.833
		8	89	-0.646
		13	89	-0.752
2001	CH	1	110	-0.648
		4	140	-0.704
		9	140	-0.776
		14	140	-0.731
	FC	1	81	-0.730
		4	125	-0.787
		9	65	-0.800
		14	121	-0.808
	SR	1	105	-0.625
		4	133	-0.707
		9	133	-0.763
		14	133	-0.758
	SH	1	60	-0.767
		4	103	-0.636
		9	103	-0.752
		14	103	-0.771
2002	FC	9	71	-0.915
		14	71	-0.914
	SR	1	111	-0.735
		4	111	-0.780
		9	111	-0.893
		14	111	-0.908
	SH	1	87	-0.473
		4	87	-0.554
		9	87	-0.655
		14	87	-0.707
2003	LB	1	111	-0.705
		4	120	-0.784
		9	120	-0.813
		14	120	-0.768
	SR	1	63	-0.592*
		4	116	-0.796
		9	116	-0.847
		14	116	-0.854
	SH	1	120	-0.716
		4	120	-0.749
		9	90	-0.731
		14	120	-0.691

TABLE 2.5: Correlation coefficients (CC) between 8 m salinity and temperature measurements from all depths for 15-m deployments. Correlations marked with asterisks were not significant at the 95% confidence level. All timeseries used were band-pass filtered prior to computing the correlation coefficients, isolating variability with periods from 2 to 10 days. This technique was employed to remove larger amplitude unresolved seasonal trends, maximizing the effective degrees of freedom in the correlations.

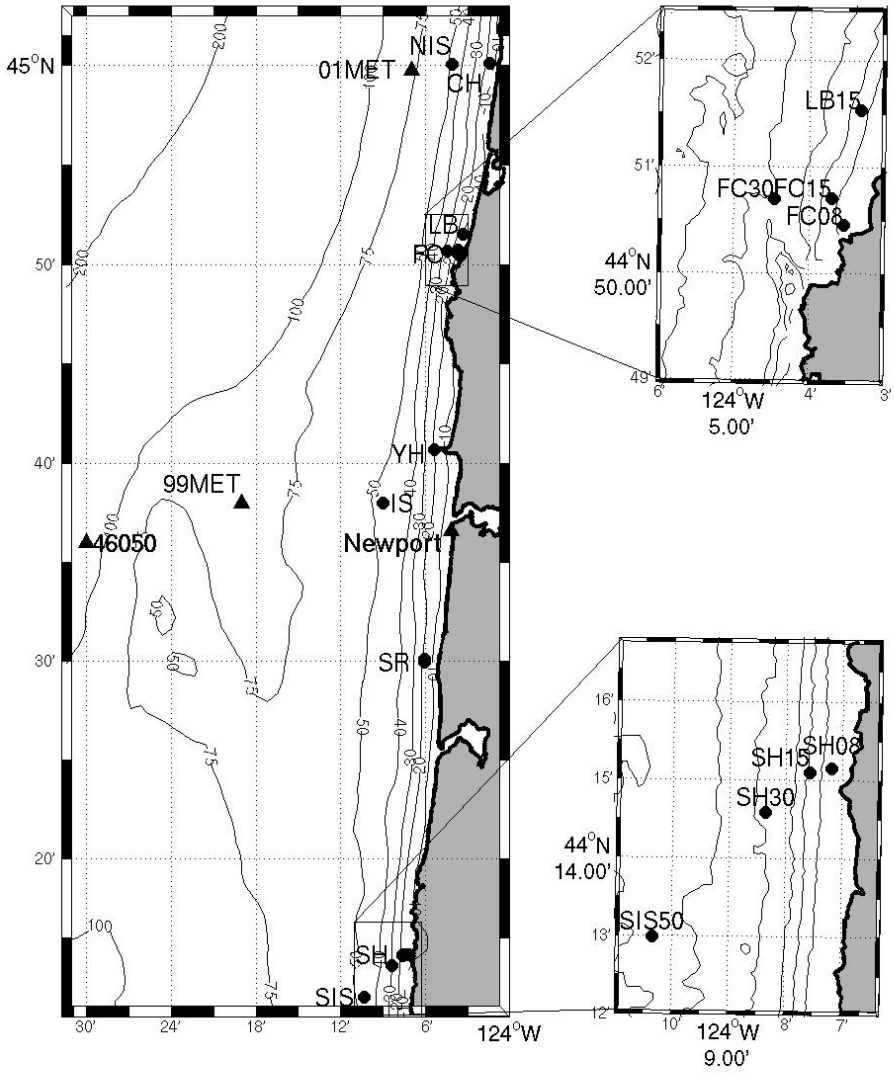

FIGURE 2.1: The study region: The continental shelf off Oregon along the west coast of the U.S.. The locations of all ADCP deployments are shown as filled circles near their station ID. Wind measurements from buoy 46050 (46050), the Newport CMAN station (Newport), the NOPP 1999 meteorological buoy (99MET), and the COAST 2001 meteorological buoy (01MET) are marked by triangles. Isobaths are in 10-m increments up to 50 m. Additionally, the 15-m isobath is included on both insets for reference.

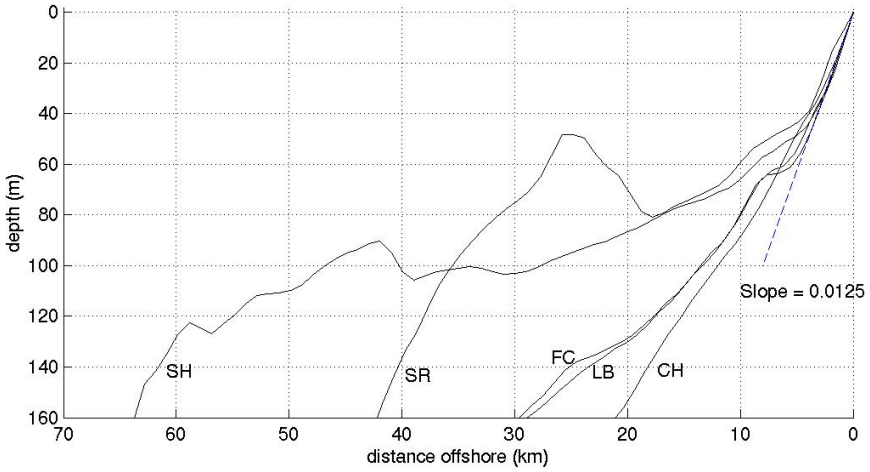

FIGURE 2.2: Bottom profiles from all major PISCO mooring locations plotted on the axis of offshore distance in km. The Station ID is near each profile. Plotted on this axis, the profiles line up with the southernmost (station SH) on the left, and the northernmost (station CH) profile on the right. A dashed line representing a bottom slope of 0.0125 is included for reference.

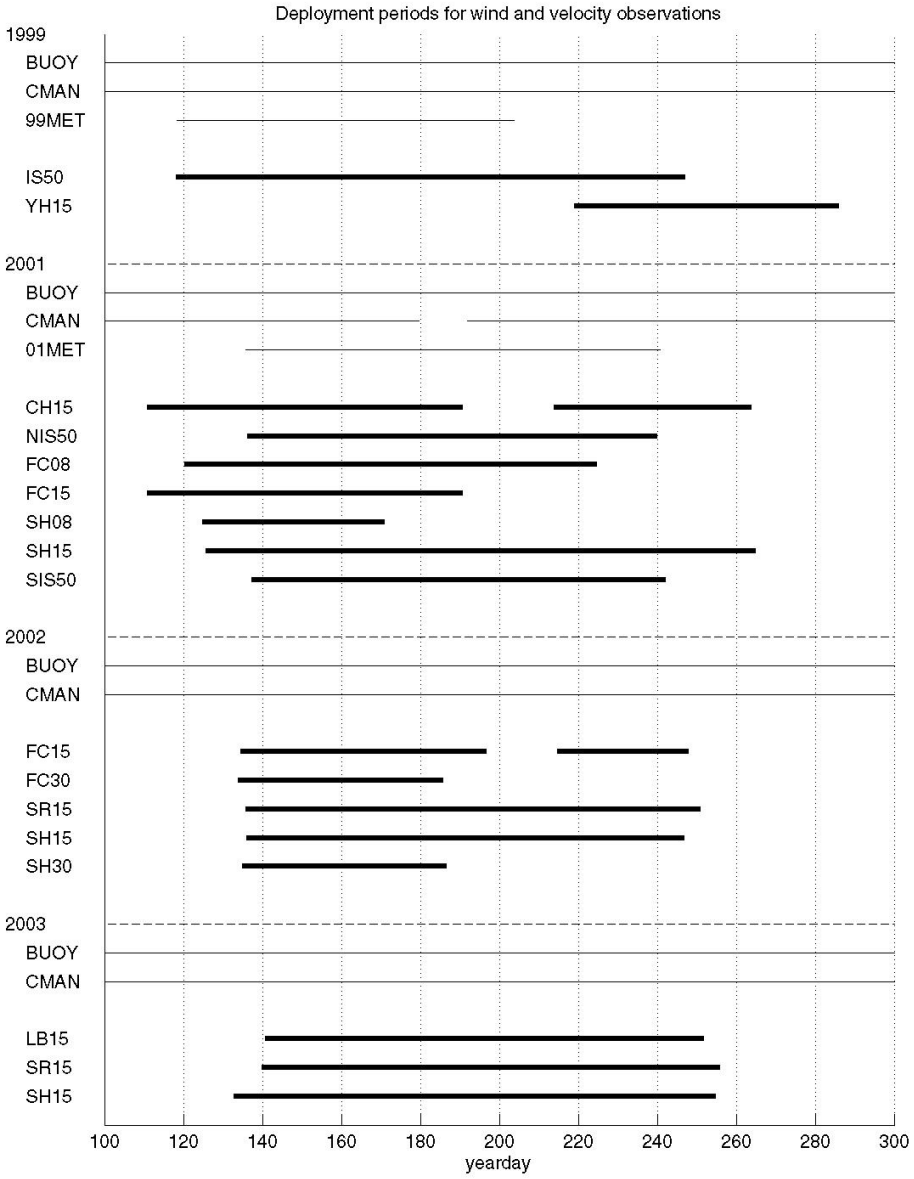

FIGURE 2.3: Deployment periods of ADCP (thick lines) and wind measurements (thin lines) used in this study.

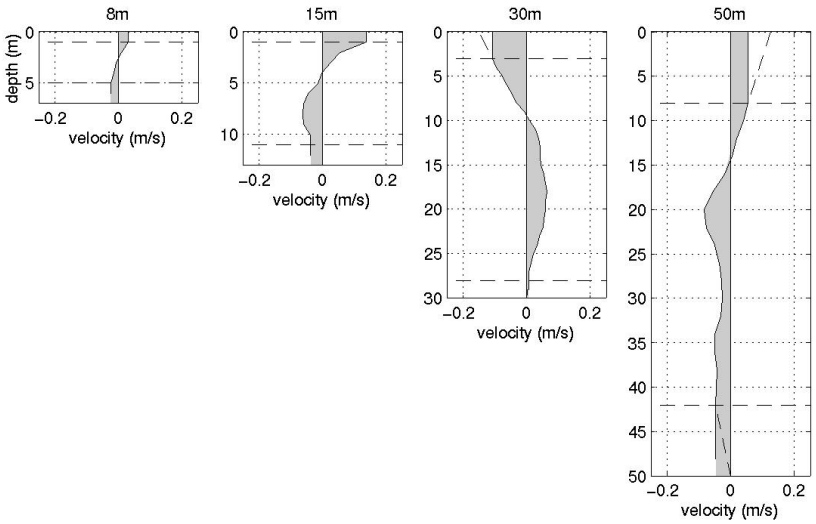

FIGURE 2.4: Examples of hourly-averaged across-shelf velocity profiles for each deployment depth. In each, the measured velocities exist between the horizontal dashed lines. These across-shelf profiles were used to calculate measured surface and bottom transports following the methods described in the text. The shaded areas of these profiles form the measured surface or bottom transports using the constant velocity extrapolation method. Constant slope extrapolations are included on the 30-m and 50-m deployments for reference.

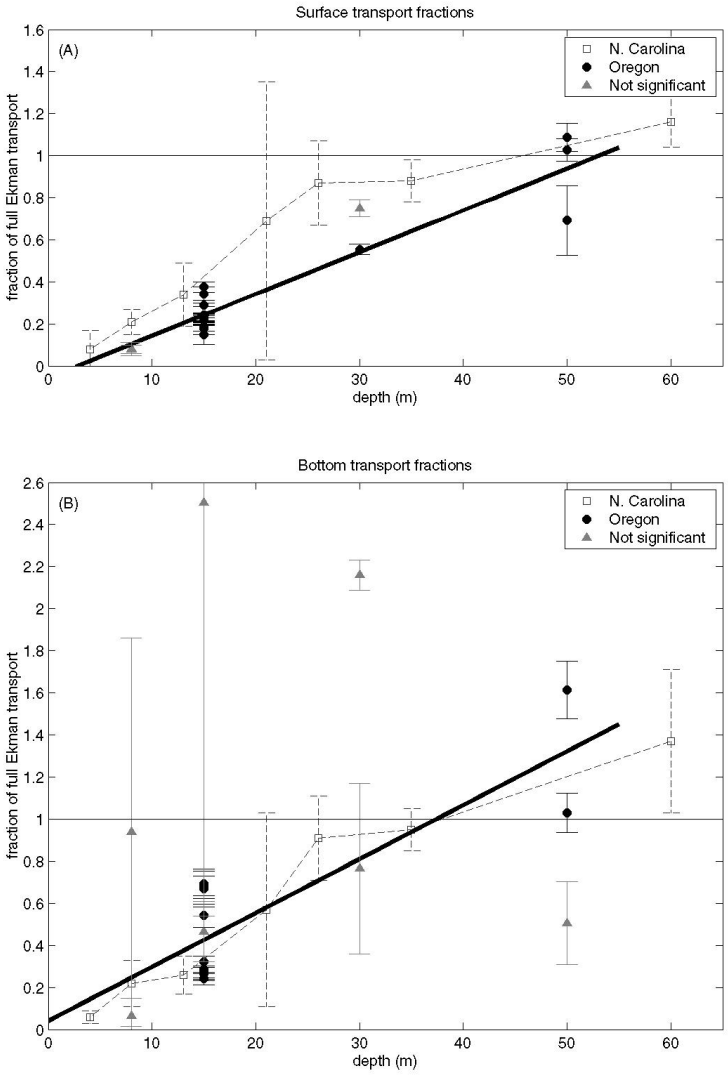

FIGURE 2.5: Fraction of full Ekman transport for (A) surface and (B) bottom transport. Dark circles indicate significant regression results, each with its individual confidence interval shown. Light triangles indicate the deployments that did not meet the necessary conditions for significance. A linear fit to the significant results is shown for each layer. Results for the North Carolina coast from Lentz (2001) are overlaid as open squares connected with a dashed line.

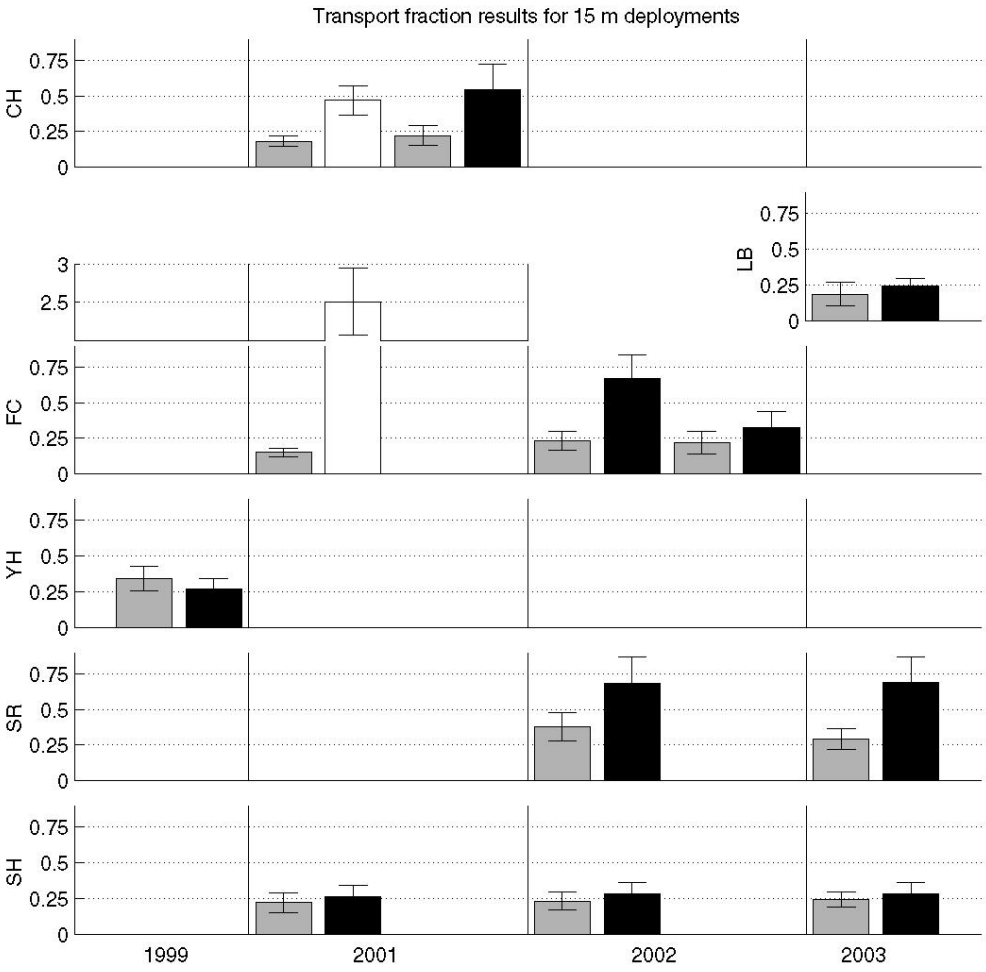

FIGURE 2.6: Transport fraction results of the 15-m deployments only. Stations are listed from north to south and the results for each station, both surface (light) and bottom (dark), are displayed by deployment year, left to right. Deployment results not meeting the necessary conditions are included as well (open bars).

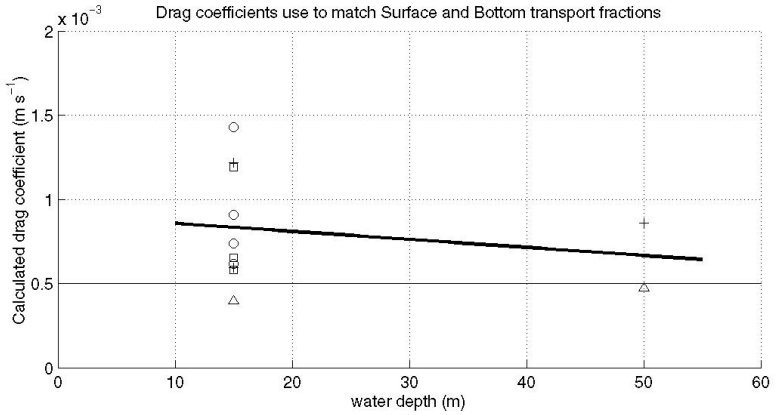

FIGURE 2.7: The bottom drag coefficient found by requiring the bottom transport fraction to equal the surface transport fraction. Calculated coefficients are shown for all deployments where results from both layers were significant. A linear fit to the results shows a trend of increasing r values with decreasing water depth. The year of each deployment is noted as: 1999 (triangle), 2001 (plus), 2002 (circle), and 2003 (square).

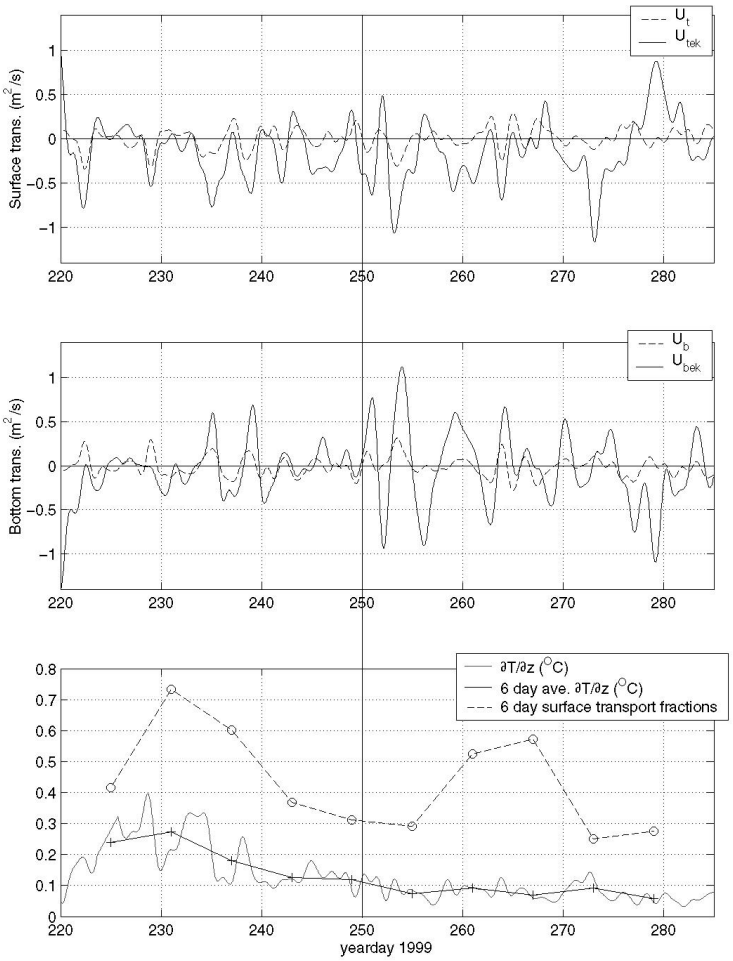

FIGURE 2.8: Stratification and transport results for the 15-m deployment at station YH in 1999. The top and middle panels show the resulting measured (U_t and U_b) and theoretical (U_{tek} and U_{bek}) Ekman transport for both the surface layer (top panel) and the bottom layer (middle panel). The bottom panel shows the stratification proxy as well as the 6-day block averages of stratification and 6-day surface transport fractions for this deployment. The decrease of transport fractions with decreased stratification is visually seen by comparing the measured and theoretical transport before and after yearday 250.

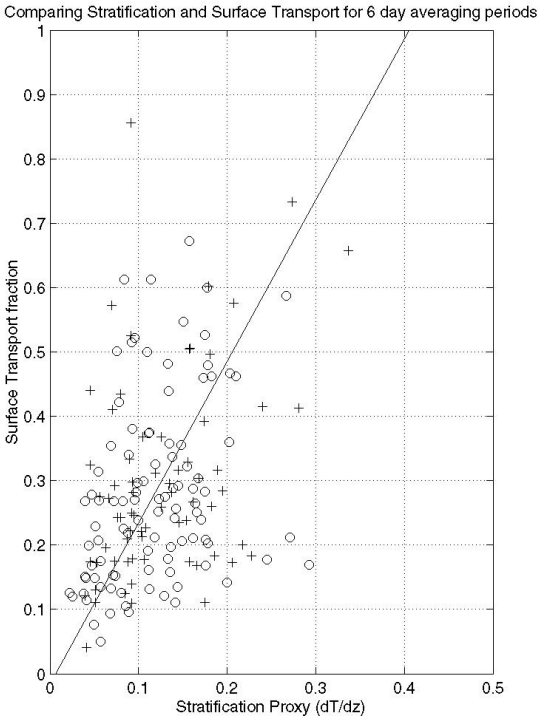

FIGURE 2.9: Scatter-plot of 6-day block average stratification and 6-day block surface transport fractions from the 15-m deployments. Stratification averages were found using the 1-14 m temperature differences (circle) or the 4-14 m temperature differences (plus). A neutral regression of stratification vs. transport fraction gives a slope and intercept of 2.5 and -0.01 respectively. The two time series are weakly positively correlated, having a correlation coefficient of 0.35 with a 95% level of significance of 0.17. The correlation was strongest using the 6-day averaging interval shown here, i.e. the middle of the weather band.

3. SPATIAL AND TEMPORAL VARIABILITY OF INNER-SHELF CIRCULATION ALONG THE CENTRAL OREGON COAST DURING SUMMER.

Anthony R. Kirincich and John A. Barth

Journal of Physical Oceanography

45 Beacon Street, Boston, MA 02108-3693

Submitted

Abstract

The nature and variability of inner-shelf circulation along the central Oregon coast are examined using measurements obtained in water depths of 15 m during the summer of 2004. Although wind forcing and bathymetry are spatially uniform in the inner-shelf, distinct differences in circulation existed among four along-shelf stations. Upwelling circulation at the northernmost station, north of an offshore submarine bank, is similar to classic two-dimensional (2D) upwelling with along-shelf bottom stress and acceleration balancing the along-shelf wind stress. In contrast, onshore of the bank at the southern three stations, the 2D balance is poor and inclusion of the pressure gradient and nonlinear terms improves the along-shelf momentum balance. During downwelling events the 2D balance holds well at the southern sites, but poorly at the northern site. The dominant mode of variability, found using EOF analysis of pressure, along-shelf velocity, across-shelf surface transport, and density, was correlated to the local wind forcing and seen at all stations. A second mode, unrelated to the wind, drives additional upwelling or downwelling north of the bank. The observed temporal and spatial differences result from region-wide flow-topography interactions which leave the on-bank stations in a lee. By late summer, inner-shelf flow during upwelling is strong and southward north of the bank, weak and onshore on the northern part of the bank, and increasingly southward on the southern part of the bank. These results agree favorably with previous outer- and mid-shelf studies conducted in the region, while offering new insight into physical and ecological interactions in the inner-shelf.

3.1. Introduction

Inner-shelf circulation along the central Oregon coast has recently been the focus of an intensive monitoring effort by the Partnership for Interdisciplinary Studies of Coastal Oceans (PISCO) program. PISCO is a long-term ecological consortium created in 1998 to study the link between inner-shelf oceanography and marine ecosystems along the U.S. west coast. Along the central Oregon coast, PISCO has maintained an array of moorings at water depths of 15 m since 1999. Deployed each spring and summer, these moorings collect velocity profiles, bottom pressure (since 2004), and hydrographic measurements. This study uses PISCO data from the 2004 upwelling season to establish the physical characteristics and along-shelf variations of inner-shelf circulation along the central Oregon coast, setting the stage for future investigations of the biological implications of these variations. The time series from this season enable a thorough description of inner-shelf circulation in the region as well as the computation of the terms in the depth-averaged, along-shelf momentum equation.

Flow over the continental shelf off the Oregon coast has been investigated in numerous process studies [originally: CUE-I (Smith, 1974; Huyer et al., 1974), CUE-II (Kundu and Allen, 1976), and more recently: the 1999 NOPP project (Oke et al., 2002a,b; Barth et al., 2005a), the 2001 COAST project (Barth et al., 2005b; Kosro, 2005)] as well as long-term monitoring projects [GLOBEC: (Smith et al., 2001; Huyer et al., 2005), and coastal HF radar observations (Kosro, 2005)]. Together these works have increased our understanding of upwelling processes and documented circulation patterns on the central Oregon middle and outer continental shelf, where water depths are greater than 50 m (Figure 3.1). In contrast, circulation in the inner-shelf, the transition area between the surf-zone onshore and the mid-shelf offshore, was largely neglected by these studies due to lack of data. Previous hydrographic surveys of the shelf were conducted in waters deeper

than 40 m. Previous 'close to shore' moorings have been deployed at water depths of 50 m, the outer edge of the inner-shelf (Kirincich et al., 2005). Most numerical models of shelf circulation have used smoothed onshore topography and a coastal wall at 10 m water depth as the onshore boundary condition.

From these studies, a description of shelf-wide circulation emerges. During summer, ocean circulation along the central Oregon shelf is forced by intermittent upwelling favorable winds that are nearly spatially uniform with minimal wind stress curl (Samelson et al., 2002). North of Newport, Oregon, in a region of simple topography, the upwelling circulation is essentially two-dimensional (2D) with little variation in the along-shelf direction (Kundu and Allen, 1976). However, a three-dimensional (3D) circulation pattern develops as the southward flowing upwelling jet encounters an offshore submarine bank (the Heceta and Stonewall Bank complex - Figure 3.1). Approaching the bank, the upwelling jet can be forced offshore and around the western edge, creating a 'lee' region on the bank (Barth et al., 2005a). This lee develops as the upwelling season progresses and by late summer, the position of the jet to the south of the bank is quite variable (Castelao and Barth, 2005). Flow on the bank has been the focus of additional analysis (Oke et al., 2002b; Barth et al., 2005b; Kosro, 2005; Gan and Allen, 2005). Both observations and models have shown that the magnitude of along-shelf flow on the bank during upwelling favorable winds is reduced compared to areas to the north, while levels of nutrients and phytoplankton are increased. Evidence of localized coastal upwelling onshore of the bank exists as well (Kosro, 2005; Barth et al., 2005b).

Inner-shelf circulation has not been investigated on the spatial and temporal scales of these shelf-wide studies, yet some interesting contrasts do exist. Physical conditions in the inner-shelf along the central Oregon coast differ from those offshore. Bathymetry at depths less than 50 m is relatively uniform in the along-shelf direction, despite the offshore bank reaching to within 7 m of the sea surface. The across-shelf scale of the divergence of

Ekman transport, marking the region of active coastal upwelling and defining the inner-shelf, has no along-shelf trends in this region (Kirincich et al., 2005). Yet, Menge et al. (2002, 1997) found that the growth of mussels and barnacles at rocky intertidal sites onshore of the bank were consistently higher than sites to the north or south. Nutrients and primary production had similar patterns. It has been suggested that inner-shelf oceanographic differences could be the primary driver for these variations (Leslie et al., 2005).

A common tool of analysis in shelf circulation studies is the computation of terms in the depth-averaged, along-shelf momentum equation. In water depths of 100 m along the Oregon coast, Allen and Smith (1981) found that Coriolis acceleration was the dominant term, possibly balanced by a baroclinic pressure gradient. A secondary balance between along-shelf wind and bottom stress existed as well, augmented by acceleration at periods less than 10 days and the barotropic pressure gradient at longer periods. Bottom stress was consistently small at this depth. Later work by Federiuk and Allen (1995) and Lentz and Chapman (2004) has shown that the nonlinear terms, specifically the offshore advection of along-shelf momentum, can be substantial over the Oregon shelf, balancing the wind stress during upwelling.

With shallow water depths and a proximity to the coastal boundary, inner-shelf observations should contrast with these studies. Across-shelf velocities are minimized in the along- and across-shelf coordinate system usually chosen, making the Coriolis term small and difficult to resolve accurately. Previous inner-shelf studies have shown that wind stress and bottom stress form the dominant along-shelf balance (Lentz et al., 1999; Lentz and Winant, 1986). Yet, as water depths increase the along-shelf pressure gradient becomes more important in driving along-shelf currents. However, the validity of these results decrease as stratification or velocity shear increases (Lentz and Winant, 1986).

Given the contrast of uniform bathymetry and wind forcing near the coast, with

non-uniform bathymetry and circulation further offshore, this paper intends to establish the physical characteristics and along-shelf variations of inner-shelf circulation along the central Oregon coast. The 2004 PISCO mooring array and the necessary processing steps are described in Section 2, while Section 3 contains a description of the 2004 upwelling season and the general characteristics of inner-shelf circulation in the region. In section 4 we analyze the modes of variability using Empirical Orthogonal Functions (EOFs), while terms in the depth-averaged, along-shelf momentum equation are analyzed in Section 5. We conclude by discussing these results (Section 6) and summarizing our findings (Section 7).

3.2. Data sources and methods

3.2.1 The 2004 PISCO mooring array

During the summer of 2004, the PISCO program maintained moorings in 15 m of water (∼1 km offshore) at four, along-shelf locations on the central Oregon coast. These locations, listed from north to south, Lincoln Beach (LB), Seal Rock (SR), Yachats Beach (YB), and Strawberry Hill (SH), spanned an along-shelf distance of 67 km (Figure 3.1, Table 3.1). In the north, station LB is located in a region of relatively uniform bathymetry in the along-shelf direction, while the remaining stations to the south are located onshore of the Stonewall and Heceta Bank complex. At each station, a bottom-mounted, upward-looking acoustic Doppler current profiler (ADCP) was deployed along with a mooring of temperature and conductivity sensors. The ADCP, a RDI Workhorse 600-kHz model, collected velocity profiles in 1-m depth bins between 2.5 m above the bottom and 1 m below the surface as ensemble averages of 40 pings (1.5 s ping rate) every two minutes. Bottom pressure was recorded at each ADCP (14.5 m depth) using a Keller 5-Bar, sealed-gauge, piezo-resistive pressure transducer. The nearby hydrographic moorings measured

temperature at 1, 4, 9, and 14 m with ONSET XTI or Tidbit loggers and temperature and conductivity at 8 or 11 m depth using Seabird 16 or 37 recorders (Table 3.1). The length of individual time series varied greatly due to weather conditions, instrument failures, and losses (Table 3.1). As a result, much of the analysis is split into two periods: early summer (before day 190) when velocity and pressure observations are available for stations LB and YB only; and late summer (after day 190) when measurements are available from all stations.

From these measurements, we derive time series of along-shelf velocity, across-shelf surface transport, pressure anomaly, and density profiles at each station using the steps outlined below. All moored time series were averaged to hourly values centered on the hour. The hourly averaged water velocities were rotated into an along- and across-shelf coordinate system defined by the principal axis of flow. This coordinate system was calculated for each deployment separately using depth-averaged velocities (Table 3.1). Time series of across-shelf surface transport were computed from full depth velocity profiles, found assuming a constant velocity (slab) extrapolation to the surface and bottom, by subtracting the depth-averaged mean, and integrating the resulting profiles from the surface to the first zero crossing. This method is described further in Kirincich et al. (2005). A harmonic fit of the tidal variability, found using T_TIDE (Pawlowicz et al., 2002), and a pressure trend, calculated following the methods described in the Appendix, were subtracted from the pressure records to yield pressure anomaly. Temperature-salinity profiles from CTD casts made by PISCO at these stations revealed that a linear relationship between temperature and salinity exists in the inner-shelf during summer. The average slope of this relationship (m=8.4 ^{o}C/psu) and the 8-m (11-m at LB) salinity measurement were used to estimate salinity and density at each of the temperature locations (Table 3.1). As a quality check of this estimate, the second salinity measurement at 11 m depth at station SH was compared with the estimated 11-m salinity with good results (mean difference of

0.06 and standard deviation of ±0.09). Finally, all time series were low-pass filtered using a filter with a 40-hr cut-off frequency to isolate the sub-tidal components.

Measurement uncertainty varied for each instrument type. The accuracy of ONSET temperature loggers is 0.2°C, while Seabird temperature and conductivity accuracies are 0.005°C and 0.0005 S/m respectively. Two-minute ensemble averaged ADCP velocity uncertainties are estimated to be near 0.01 m s^{-1} (Gordon, 1996). However, with the sampling scheme used, the orbital motions of a 1 m amplitude surface gravity wave may cause a bias of up to 0.08 m s^{-1}. For most wave climates, this bias is mainly in the depth-averaged across-shelf velocity and is reduced significantly by hourly averaging. Due to this additional uncertainty, the depth-averaged, across-shelf velocities are not considered further. Pressure sensors were calibrated relative to each other, finding RMS differences of ∼1 mB with a standard error of 0.125 mB.

An Empirical Orthogonal Function (EOF) analysis was performed on many of the hourly-averaged, low-pass-filtered time series. Purely a statistical tool, the EOF calculation (Davis, 1976) decomposes measurements made at different spatial locations into coherent patterns, or modes, of variability. Each successive mode collects as much of the remaining variability as possible while being orthogonal to the previous mode. This analysis was performed separately on pressure anomaly, depth-averaged along-shelf velocity, mid-water column density, and across-shelf surface transport from each of the four stations for the common time period of year days 190 to 250 (Figure 3.2). The spatial structure of the first three modes for each EOF are listed in Table 3.2 along with their percent of the total and local variance explained.

3.2.2 Meteorological and tidal measurements

Additional measurements of wind velocity and sea level height collected at Newport, Oregon by NOAA are used here. Hourly averages of wind velocities at the Newport CMAN station, located on the south jetty of the Newport harbor entrance, were used to estimate

the wind forcing at all PISCO locations. Winds at the CMAN station are considered representative of winds throughout the study area during summer (Kirincich et al., 2005). These measurements were translated to 10 m height wind velocities using the assumption of a stable atmosphere. Wind stress in the along-shelf direction was estimated using the empirical method given by Large and Pond (1981). A 'Newport' pressure anomaly, composed of hourly averaged sea level height at NOAA's South Beach tidal station and atmospheric pressure at the CMAN station, is included for comparison to the pressure anomaly measured at the ADCPs.

3.3. General results

A description of the 2004 upwelling season along the central Oregon coast must begin with the wind forcing. Winds at Newport were intermittently upwelling favorable throughout the summer. Early in the season, winds were to the south (equatorward) with northward reversals occurring almost weekly (Figure 3.2). As illustrated by a negative accumulation in the cumulative northward wind stress (Figure 3.3), a period of more persistent southward winds begins after day 170 (June 18^{th}). After this date, northward wind events occur every $\sim$20 days, specifically near days 203, 220, and 238 (Figure 3.3).

The depth-averaged, along-shelf velocities at each station were positively correlated to the wind forcing (Figure 3.2, Tables 3.3 and 3.4). In general, northward (southward) flow occurred when winds were to the north (south). However, statistically significant lags between the velocities and the wind forcing existed. Early in the season, velocities at LB and YB lag the wind by 5 and 19 hours respectively (Table 3.3). During the second half of the season, all stations lagged the wind, with the lag generally increasing to the south from 3-12 hours (Table 3.4).

During early summer, mean flow was to the south at station LB (Table 3.1), with

large negative accumulation occurring (Figure 3.3). In contrast, station YB had a near zero mean (Figure 3.3) but larger magnitude velocity fluctuations (Figure 3.2 and Table 3.1). After year day 190, the additional two stations (SR and SH) make along-shelf differences in along-shelf velocity even more obvious. As before, a mean southward flow existed at station LB during this deployment (Figure 3.3), yet velocities at the remaining three stations differed from LB (Table 3.1). Mean along-shelf velocity was northward at station SR, in the middle of the array, yet southward at YB and SH (Table 3.1). Velocity standard deviations at these on bank stations were all larger than at LB. From these observations, we see that two flow regimes exist: a near-zero or southward velocity present during upwelling favorable (southward) winds, and a large northward velocity that occurred in response to northward wind events. During upwelling winds, along-shelf velocities were 0.2 m s^{-1} to the south at station LB, near zero at station SR, 0.1 m s^{-1} to the south at station YB, and 0.2 m s^{-1} to the south at station SH (Figures 3.2 and 3.3). Northward flow occurred every $\sim$20 days, with the largest on year day 238 exceeding 0.3 m s^{-1}.

The isolation of inner-shelf waters onshore of the bank from waters to the north is evident from the convergence of along-shelf velocities between stations LB and YB before day 190 and stations LB and SR afterward (Figure 3.3). This convergence implies that southward flowing waters north of the bank are exported offshore throughout the summer. In addition, the velocity divergence between stations SR and YB after day 190 implies a mean onshore flow must exist between the two to conserve mass.

Time series of pressure anomaly tell a similar story. Pressure anomaly is used here as a proxy for the across-shelf pressure gradient present during coastal upwelling, a reasonable assumption given the shallow onshore location of our measurements. Early in the season, anomalies at stations LB, YB, and Newport (NP) are all positively correlated with the along-shelf wind stress (Table 3.3). This is visibly apparent during days 168-185 in Figure

3.2. As the summer progressed, pressure anomaly at station LB diverged from those to the south, most notably on days 203, 219-225, and 235-244. As a result, correlations of pressure between the LB and the wind, as well as with stations YB and NP were reduced compared to early season values (Table 3.4). Among the stations onshore of the bank (SR, YB, SH, and including NP), pressure anomalies were well correlated during this time period.

Accumulated across-shelf transport was similar among the stations, in contrast to accumulated along-shelf velocity. Early in the season, transport was offshore at YB and LB, yet YB accumulated slightly larger values. Near day 190, YB and SH had onshore transport for 10 days while SR and LB were near zero. After this point all stations accumulate offshore surface transport, with some station-to-station variations as well as onshore transport events. The total accumulated transport for all four stations during the second half of the season is similar between LB, SR, and YB, yet slightly higher at SH.

Time series of density are included at the bottom of Figure 3.2 from 8 m depth at stations SH, YB, and SR, and 11 m depth at LB. In general, a sharp increase in density occurred at the onset of strong upwelling on day 165, before which significant variability existed. During this persistent upwelling, density reaches a maximum near 26 kg m^{-3}, marked in Figure 3.2 by thin, light lines for each time series. The wind reversals noted above are seen in the hydrography as sharp decreases in density around days 203, 220, and 238. Here, density reaches minimum values of 23.5-24.5 kg m^{-3} for 2-3 days. In contrast to velocity and pressure, spatial variations in density are difficult to find visually due to the larger-amplitude, low-frequency signal (Figure 3.2).

3.4. Modes of variability

Results of the EOF analyses offer an explanation for the differences in circulation between station LB, north of the offshore bank, and the southern three stations, located onshore of the bank. In all four EOFs, the first mode explained greater than 73% of the total variance (Table 3.2). Amplitudes of pressure and velocity for this mode decrease moving south from LB to YB before increasing at SH. For across-shelf transport and density, amplitudes decrease between LB and SR, increase at YB, and increase (decrease) at SH for density (transport). More than the amplitude results, the distribution of local variance explained by the EOF modes is the most interesting result. Locally, the mode one results accounted for greater than 86%, 69%, 68%, and 95% of the variability for pressure, velocity, transport, and density at the southern three stations (Table 3.2). At station LB to the north, the local percent variance explained by mode one was always lower, at 40%, 33%, 47%, and 82% for pressure, velocity, transport, and density respectively. In each of the EOFs, a higher mode (mode two for pressure, velocity, and density but mode three for transport) accounted for most of the remaining variability at station LB and little of the remaining local variance at the on-bank stations. Thus, analyzing all four EOFs together, two distinct patterns of variability exist: a dominant mode that accounted for the bulk of the total variability, and a secondary pattern which was concentrated at station LB in the north.

The dominant pattern was directly related to the local wind forcing, and its effect on across-shelf transport. Mode-one amplitude time series for pressure anomaly and along-shelf velocity are shown in Figure 3.4*a* along with the along-shelf wind stress. Time series of both pressure and velocity were positively correlated with the local wind stress. A maximum correlation of 0.63 (0.87) occurred when pressure (velocity) lagged the wind stress by 6 (8) hours. That pressure and velocity are both similar to the wind is not

surprising. This analysis has assumed that pressure anomaly was an adequate proxy for the across-shelf pressure difference, thus pressure and along-shelf velocity should be related through the depth-averaged across-shelf geostrophic balance:

$$fV = \frac{1}{\rho}\frac{\Delta P}{\Delta x}. \tag{3.1}$$

Comparing these mode-one time series (e.g. Huyer et al. 1978), velocity and pressure were significantly correlated (0.60 with pressure leading by 6 hours). A neutral regression between V and ΔP*1000* gives a slope and intercept of 2.5 m^3 (s kg km)$^{-1}$ and -0.006 m s^{-1}. Evaluating the slope in (3.1), using a reference density and Coriolis parameter of ρ=1025 kg m^{-3} and f=1x10^{-4} s^{-1}, results in a Δx of $\sim$4 km. This value is close to the 5-7 km found by Kirincich et al. (2005) for the across-shelf scale of the divergence of Ekman transport and upwelling.

The second panel of Figure 3.4*b* shows the mode one time series of across-shelf surface transport (*Us*) and theoretical Ekman transport ($Utek=\tau_s^y/\rho f$). The two time series are well correlated (0.72 at 0 lag). In the panel, *Utek* is reduced by R=0.19, the neutral regression coefficient between *Utek* and *Us* (Kirincich et al., 2005). The varying differences between *Us* and *Utek*R* illustrate variations in the fraction of full Ekman transport present in the dominant mode of *Us*. The direct effect of wind-driven across-shelf transport on density at these stations is shown by including the time rate of change of the mode-one density amplitude time series ($\Delta\sigma_t/\Delta t$). When *Us* and *Utek* were positive (negative), density decreased (increased). The rapid variations of *Us* near days 203, 220, and 235 are mirrored by changes of mode-one density, while during sustained upwelling (negative *Us*, e.g. days 205-216), density changes are much smaller. These mode-one time series illustrate the across-shelf transports and isopycnal movements associated with changes in the mode-one pressure and velocity in response to the local wind forcing (i.e. upwelling or downwelling).

Amplitude time series from the LB-dominated pattern (Figure 3.5) were uncorrelated with the local winds. In fact, the mode-two time series of pressure and velocity were often not in geostrophic balance and frequently appeared to be in quadrature, (days 217-226 and 238-245). A phase and coherence diagram of mode-two pressure and velocity shows a peak at 0.3 cpd ($2.18\text{x}10^{-5}$ s^{-1}) having a phase lag of 90^o (Figure 3.6). More information about this peak comes from a two-week moving cross-covariance between pressure and velocity (Figure 3.6). From this it is clear that the 0.3 cpd coherence peak shown is driven primarily by the large oscillations during days 214-230, with significant lags at 20 hrs (and 100 hrs, the peak of the next cycle) during this period. Lags are not stable during the remainder of the record, and velocity and pressure are occasionally correlated at zero lag (days 208 and 237). The mode-two across-shelf transport and density time series were again coupled as described above. Mode-two across-shelf transport (Us) and along-shelf transport (V) were also positively correlated (0.56 when velocity leads by 5 hours). Through mass conservation, a barotropic along-shelf velocity could cause the surface across-shelf transport (through an equal but opposite across-shelf transport in a bottom Ekman layer) and the density variability seen in the LB mode.

Based on these modal decompositions, it is apparent that the local wind forcing drives some circulation at station LB, but most circulation at the three southern stations, located onshore of the bank. The largest part of circulation at station LB is not driven by local wind forcing in this manner. This important result is addressed further in the discussion.

3.5. Along-shelf momentum

3.5.1 Theory and calculation

Analysis of the depth-averaged, along-shelf momentum equation shows both the dynamics of inner-shelf circulation along the central Oregon coast as well as some of the spatial and temporal variations that exist. We use the depth-averaged, along-shelf momentum equation (e.g. Allen and Smith 1981):

$$\frac{\partial V}{\partial t} + fU + \frac{1}{\rho_o}\frac{\partial P}{\partial y} - \frac{\tau_s^y}{\rho_o h} + \frac{\tau_b^y}{\rho_o h} + \frac{\partial \overline{uv}}{\partial x} + \frac{\partial \overline{v^2}}{\partial y} = 0, \tag{3.2}$$

where U and V are the depth-averaged across- and along-shelf velocities, u and v are the depth-dependent velocity components with the over-bar denoting depth averaging, $\partial P/\partial y$ is the depth-averaged, along-shelf pressure gradient, ρ_o=1025 kg m^{-3} is a reference density, f is the Coriolis parameter, and τ_s^y and τ_b^y are the along-shelf wind and bottom stresses. A water column depth of h=15 m is used for all stations. All terms in the balance were estimated for each station except the Coriolis acceleration. As mentioned above, U is minimized in the principal axis coordinate system making this term at or below our measurement accuracy (Table 3.1).

Briefly describing those methods not listed earlier: The acceleration was calculated using 3-point, centered finite-differences of the along-shelf velocity (V). Bottom stress, was estimated with a quadratic parameterization, using velocities from the bottom ADCP bin (centered at 2.7 m above the bottom). For each deployment, the drag coefficient (C_f) was found by minimizing the variance of the sum of the acceleration, wind stress, and bottom stress terms as these terms should compose the dominant mean balance. Calculated values for C_f ranged from 0.0007 to 0.0034 (Table 3.1) and were lower during the early season deployments at stations LB and YB, yet consistently higher at LB than the southern three stations. As a check of their validity, the mean value for all deployments, C$_f$=0.0015,

agrees with that reported by (Perlin et al., 2005) for 5 m above the bottom in 80 m of water off the Oregon coast.

The depth-averaged, along-shelf pressure gradient was a difficult term to estimate given the along-shelf spacing of the stations and limited accuracy of the sensors. The total depth-averaged pressure gradient is written as the sum of the bottom pressure gradient and depth-averaged gradients of density throughout the water column:

$$\frac{\partial P}{\partial y} = \frac{\partial P^b}{\partial y} - \frac{\partial}{\partial y}\left(\int_{-h}^{0} \rho g dz\right) + \frac{\partial}{\partial y}\left(\frac{1}{h}\int_{-h}^{0}\int_{z}^{0} \rho g dz dz\right). \tag{3.3}$$

where P is the depth-averaged pressure anomaly, and ρ is the local density. The first two terms on the right hand side comprise the sea level (or barotropic) pressure gradient, while the third term describes the depth-averaged water column (or baroclinic) pressure gradient. Estimates of both the second and third terms were made from the time series of density profiles at each station. A comparison of the three terms on the right hand side of equation 3.3 (not shown here) revealed that the contribution of bottom pressure to the total pressure gradient was an order of magnitude greater than the remaining terms. Thus, because of the significant time gaps in the density records and their small contribution to depth-averaged pressure, only the bottom pressure term was used to calculate the pressure gradients used here. Station pairs for along-shelf pressure gradients were chosen as follows: Stations LB and YB, with an RMS difference of 1.7x10^{-3} Pa m^{-1}, are paired during days 133-190. For days 190 to 248, a LB-SR pair is used at station LB while the SR-SH pair was used at stations SR, YB, and SH, both with RMS errors of 3.3x10^{-3} Pa m^{-1}.

The nonlinear advective terms in equation (3.2) were estimated from products of unfiltered hourly velocities, depth-averaged, and then low-pass filtered. The first term, the across-shelf advection of along-shelf momentum ($\partial\overline{uv}/\partial x$), was estimated at each station using the gradient of the velocity product between the mooring (1 km offshore) and the coast, where the velocity product must be zero, following Lentz and Chapman (2004). The

second term, the along-shelf advection of along-shelf momentum ($\partial\overline{v^2}/\partial y$), was estimated using differences between the same mooring pairs used to estimate pressure gradients.

We also consider the average balance from each station under different forcing and response regimes. Terms in the momentum equation were grouped by the sign and magnitude of the wind stress term into periods of upwelling favorable winds, near zero winds, or downwelling favorable winds using a threshold value of $\pm 5\text{x}10^{-7}$ m s^{-2} and averaged. This threshold corresponds to a wind stress of $\pm 7.7\text{x}10^{-3}$ Pa. Mean terms during times of near-zero bottom stress were also found using a similar threshold. The average residuals of the 2D balance (the acceleration, wind stress, and bottom stress) and the full equation (the sum of all terms) were found under each regime as well. If either of these combinations is an accurate representation of local dynamics, its magnitude will be small compared to the terms in the balance. The percentage of the total time spent in each regime is also reported. This metric provides a useful tool to assess circulation conditions as well as the representativeness of an individual result.

3.5.2 Results

Results from representative stations LB (off-bank) and YB (on-bank), occupied for the longest period, are described here for days 133-190 and 190-250 (Figures 3.7 & 3.8). Again, the split into two time periods was made due to deployment lengths, and the availability of suitable pressure records. Results for the other stations (SR and SH) are similar to those presented for YB.

Focusing on upwelling wind events, these time series results illustrate the interaction of each of the terms on the time-scales of wind forcing events (e.g. days 145-149 and 166-172 in Figure 3.7). After the onset of an upwelling wind, acceleration first increases to balance the wind, followed shortly by an increasing bottom stress. The sum of these three terms form the classic 2D upwelling balance (*2D-res*), as shown in panels *b* and *d* of Figures 3.7 and 3.8. These two upwelling events also illustrate the failure of *2D-res* as well

as differences in circulation at these stations. In the first event, days 145-149, acceleration and bottom stress do not fully balance the wind and a non-zero *2D-res* exists (Figures 3.7b,d). At both stations the along-shelf pressure gradient appears to offset the remainder of these three terms. During the second event, days 166-172, the bottom stress response is much weaker at station YB, giving a larger *2D-res* here compared to LB. At YB only, the across-shelf momentum flux term appears to offset the larger *2D-res* at a time when the estimated pressure gradient is incomplete.

Looking at these time series as a whole allows more general results regarding term interactions. A tight interaction existed between acceleration and the stresses. Usually, acceleration balanced a changing wind stress as the change propagated through the water column to the bottom, allowing the bottom stress to react. Thus, at these stations, acceleration is a significant term in the time-dependent balance. The two nonlinear terms were largest at station YB, becoming similar in magnitude to the acceleration. The cross-shelf flux of along-shelf momentum was the larger of the two terms, having maxima during times of high winds and/or weak bottom stress (Figures 3.7 and 3.8). This term frequently offsets an unbalanced *2D-res* in addition to the pressure gradient (e.g. days 203-207 and 238-240 in Figure 3.8).

The along-shelf pressure gradient balanced *2D-res* most frequently during the first half of the season at station LB (Figure 3.7b). In contrast, at this station pressure gradients were regularly much larger then all other terms during the second half of the season (Figure 3.8). After day 200, the pressure gradient at LB was mostly unbalanced with large magnitudes and peak variations that coincided with the major downwelling events described earlier. At YB, the pressure gradient offset *2D-res* and the advective terms during both deployments. This was most apparent at station YB during days 145-160 and 174-180 (Figure 3.7d) and days 203-207, 214-230, and 238-240 (Figure 3.8d). A large pressure gradient also occurred at station YB during days 226 to 236.

The occurrence of balanced and then unbalanced pressure gradients implies that the along-shelf scale of pressure variation varied over the summer. Balanced pressure gradients were often found early in the season, implying that the along-shelf scale of pressure variation was longer than the mooring array. After day 190, the LB-SR pressure gradient (the off-bank/on-bank gradient) did not appear to represent the pressure gradients at LB, but the SR-SH pressure gradient (the on-bank gradient) balanced the momentum equation at YB frequently during this period.

Given the convergence of cumulative velocity between LB and SR late in the season (Figure 3.3), the measured LB-SR along-shelf pressure gradient could have a significant contribution from the geostrophically-balanced equatorward upwelling jet that must turn offshore (crossing isobaths) between these stations. If true, the along-shelf velocities at LB would become across-shelf velocities for a station between LB and SR. To explore this hypothesis, the along-shelf geostrophic balance in (3.2) was tested using the LB-SR pressure gradient and three estimates for U in the along-shelf Coriolis acceleration: the depth-averaged, along-shelf velocities from stations LB, SR, and the amplitude time series of the first velocity EOF. Of the three, the mode-one velocity time series gave the highest negative correlation (-0.76 when fU leads by 26 hours as shown in Figure 3.9). This lag is consistent, given the flow speeds of the jet, with the time needed for a change in along-shelf flow to propagate through the region between LB and SR, altering the along-shelf pressure gradient and across-shelf transport via mass conservation. The residual of this geostrophic balance, when fU is lagged by 26 hours, is weakly negatively correlated (-0.28) with the 2D residual from station LB during this time period (Figure 3.9). Thus, adjusting the LB-SR along-shelf pressure gradient for the offshore movement of the along-shelf upwelling jet reduces its amplitude to that of other terms in the equation over much of the time series. The large pressure gradients that still occur (e.g., year days 220, 224, and 242) come at times of rapid transitions between upwelling and downwelling events.

This adjusted pressure gradient is used below at station LB.

Analyses of the regime mean balances for all four stations from the second half of the season reinforces the time-dependent results described above. The top two rows of Figure 3.10 display the mean along-shelf momentum balance under upwelling (top row) and downwelling (2nd row) favorable winds. Upwelling favorable winds occurred ∼50% of the deployed time while downwelling winds occurred ∼25% of the time. During upwelling conditions, bottom stress is strong and negative at station LB. Here, the acceleration and bottom stress appear to balance the wind stress as the residual of these three terms is small, indicating that the 2D balance holds well. Additionally, the adjusted along-shelf pressure gradient and along-shelf advection terms contributed to a larger full-equation residual. In contrast, *2D-res* was larger at the three southern stations as the mean bottom stress during upwelling winds was reduced in magnitude. At these stations, the full residual was lower in magnitude (esp. at station SH) as the across-shelf momentum flux, aided sometimes by the pressure gradient, offset the wind stress.

During downwelling conditions (2nd row, Figure 3.10), the average momentum balances are distinctly different. Both mean residuals are large at LB, yet small at SR, YB, and SH. While *2D-res* is near-zero at SR, the pressure gradient brings the full residual closer to zero at SH. At LB, the full residual was large due to the negative pressure gradient and advective terms. In contrast to upwelling conditions, the advection terms are smaller during downwelling, except for the along-shelf momentum flux at LB and SR.

Finally, grouping the momentum balance terms by near-zero bottom stress reiterates the importance of the across-shelf momentum flux term during upwelling at stations SR, YB, and SH. Weak bottom stress existed during 57-70% of the deployments at these stations. Yet during this time, upwelling favorable wind stress occurred at all three stations. This wind stress was always offset by the across-shelf momentum flux term, and sometimes (stations SR and SH) by the pressure gradient. In contrast, weak bottom stress

occurred during 34% of the second deployment at LB, with only the pressure gradient being significant. As also shown above in the time series, this result implies that despite similar water depths, upwelling circulation is dynamically different between station LB north of the bank and the southern three stations, located onshore of the bank.

3.6. Discussion

3.6.1 Comparison with previous studies

The description of inner-shelf circulation along the central Oregon coast given here agrees well with the region-wide circulation described earlier. The combined picture is summarized in Figure 3.11. From these results, it is clear that the effects of the offshore submarine bank on the large-scale upwelling circulation are felt all the way into the inner-shelf, onshore of the bank. The convergent flow between LB and SR suggested by cumulative velocities (Figure 3.3), is consistent with the offshore transport of the main upwelling jet seen in recent COAST surveys (Castelao and Barth, 2005; Barth et al., 2005b). These authors showed that the main upwelling jet moved offshore in the region between LB and SR. In addition, the divergence between SR and YB is consistent with the northeastward flow onto the north part of the bank from the southwest also found in these surveys. The signature of a secondary upwelling jet (the 'mini-jet'), apparent here based on the southward velocities at YB and SH and previously by shelf-wide observations (Barth et al., 2005b; Kosro, 2005) and numerical models (Oke et al., 2002a,b; Gan and Allen, 2005), forms late in the season onshore of the bank. Spatial amplitudes of the first mode pressure EOF matched the on-bank/off-bank variations seen by Barth et al. (2005b) using dynamic height analysis. Further, the mode-one variations from all EOFs appeared directly related to the local wind forcing. This relation was previously seen by Kosro (2005) in shelf-wide surface currents in the region. These similarities suggest that

the 2004 results are representative of general summer upwelling conditions in the study area and able to highlight along-shelf differences in the inner-shelf.

Our analysis of the depth-averaged, along-shelf momentum equation found that the dominant balances can be quite complex. In contrast to previous inner-shelf observations, the stresses were rarely the only significant terms in the momentum equation. At all stations, acceleration played an important part of the 2D balance, both in the time-dependent balance and the mean upwelling and downwelling regime balances. We suggest the importance of acceleration in the mean circulation cannot be discounted in areas of higher stratification and intermittent winds such as the Oregon shelf. Further, the along-shelf pressure gradient frequently offsets the residual of the stresses and acceleration, most often at the on-bank stations.

The largest difference in the along-shelf momentum balances at the four stations was the importance of across-shelf advection at the on-bank stations. Lentz and Chapman (2004), using mid- to outer-shelf observations and model results, proposed that the across-shelf advection of along-shelf momentum term can fully balance the wind during upwelling when bottom stress is small. With little bottom stress, the across-shelf momentum flux frequently balances *2D-res* at our on-bank stations. In contrast, this term was usually small at LB. We hypothesize that the small scale of the 'mini-jet', with its along-shelf spin-up noted above, makes terms traditionally looked at in larger-scale shelf-wide studies important in the inner-shelf. At LB, located on the onshore side of the larger jet, little vertical shear of the along-shelf velocity shear exists. The along-shelf advection of along-shelf momentum term was found to be relatively small here, despite the spatial variations in along-shelf velocity described in Section 3.

Recent numerical models of the region provide an interesting comparison with our findings. Oke et al. (2002b) describe two types of inner-shelf dynamical balances: areas in the coastal jet and areas onshore of the jet. Circulation at station LB appears to match

their description of an area frequently within the jet, with large accelerations and generally a 2D momentum balance during upwelling. To the south and on the bank, accelerations were smaller in magnitude and the addition of the pressure gradients contributed to better balances during upwelling, characteristic of areas onshore of the main jet as described by Oke et al. (2002b). Further, their mean results for depth-averaged velocity and bottom stress appear to capture the along-shelf variability shown here during upwelling.

A second interesting model-data comparison can be made for relaxation events. Gan and Allen (2002)'s model study of the CODE region found that after cessation of an upwelling wind, the local southward pressure gradient was balanced by northward acceleration. In our study area, Oke et al. (2002b) found this to be true on the bank itself, while north of the bank acceleration balanced bottom stress during relaxation. Our results during the major relaxation event (days 170-180) appear mixed. Flow at LB was initially northward as evident from the depth-averaged velocities (Figure 3.2). A decreasing wind stress was balanced by acceleration and bottom stress after which all terms were small. At YB, where flow was initially near zero (Figure 3.2), the pressure gradient balances the 2D residual after day 175, composed mostly of acceleration and bottom stress. It should be noted that it is difficult in practice to find true relaxation events (upwelling to zero wind transitions) in the 2004 data. Wind fluctuations are more often quick transitions to downwelling winds rather than transitions to 'relaxed' weak winds.

3.6.2 EOF modes

The sheltering effect of the lee on the on-bank stations is also evident from the EOF results. Local wind forcing (mode one) dominated the system, accounting for nearly all variability at on-bank stations. The variability not accounted for by this mode at these stations (i.e. the mode two velocity and mode three transport variability at SR) is likely related to the along-shelf spin up of the mini-jet. At station SR, along-shelf velocities were near zero during upwelling favorable winds, but by station SH, 27 km to the south,

velocities were southward and of similar magnitude as those at LB, off the bank to the north. This stagnation point of along-shelf circulation in the area of station SR has not been observed previously.

In contrast to the on-bank stations, LB is exposed to the larger, regional upwelling jet and forced both by the local winds as well as a second mode of variability. It is tempting to infer that the 0.3 cpd coherence between pressure and velocity in this mode is the signature of remotely forced coastal-trapped waves (CSW). Indeed, this coherence peak is similar to one reported in an early study of these phenomenon on the Oregon coast by (Huyer et al., 1975). Using sea level data collected at Depoe Bay (5.5 km south of LB) and current meter velocities at station NH-10 (in 80 m of water, 29 km southwest of LB) for the second half of the upwelling season (July-September) in 1972, the authors reported a 0.3 cpd coherence peak that could not be attributed to the local wind forcing. However, the phase relationship found here (quadrature) is not characteristic of free, unforced CSWs. Phase information for this coherence peak in Huyer et al. (1975) was not significant, yet the wind-forced coastal-trapped wave results of Chapman (1987) do show a similar phase lag between pressure and velocity in the CODE region (his Figures 9 and 10). A second, possibly more apt, explanation might be that this mode, combined with mode one, show the delayed movement of the regional upwelling jet in response to the integrated wind forcing.

Regardless, it is interesting that these features where not seen at the on-bank stations, or at Newport. The link between V, Us, and $\Delta\sigma_t$ in the LB mode infers that the along-shelf velocity of the LB mode was related to (or caused) additional across-shelf circulation not directly forced by the local winds, and therefore not seen at the on-bank stations. Thus, although the mode-one transport amplitude at LB was half that of the on-bank stations (Table 3.2), the total across-shelf transport at LB, including both mode one and mode three contributions, was similar in magnitude to the on-bank stations (Figure

3.3). Only the timing of events (i.e. frequency content) differed.

Our findings have important implications regarding the use of the Newport sea level station for dynamical studies of the region. The Depoe Bay station used by (Huyer et al., 1975) was occupied for their study and abandoned soon after. Upwelling season observations in the region (Cutchin and Smith, 1973; Allen and Smith, 1981; Kundu et al., 1975; Battisti and Hickey, 1984; Kosro, 2005) using sea level from the Newport station did not observe the 0.3 cpd coherence structure seen here and by Huyer et al. (1975). The one exception was Mooers and Smith (1968), who use a full year (both upwelling and downwelling seasons) of sea level observations including the Newport station and reported coherences of pressure at this frequency. Our results show that during late summer, the Newport sea level was closely related to pressure at the on-bank stations, all of whom were sheltered from the LB mode. EOFs of pressure anomaly including the Newport sea level data, not shown here, have similar dynamical patterns as those reported here. Thus the Newport station is representative of the on-bank pressure variability, but not of region-wide sea level variability during this time. Because of this 'on-bank/off-bank' effect, sea level heights from the South Beach station should be used with caution in dynamical studies.

3.6.3 Ecological implications

These results have a number of important implications for the regional marine ecosystem. The varying fates of inner-shelf waters north of the bank and those onshore of the bank tend to support some of the known along-shelf ecological variations reported earlier. A key difference between the southward velocities on and off the bank is that on-bank waters (station SH) remain near the coast while off-bank waters (station LB) are diverted offshore by the bank. A possible effect of this is that chlorophyll *a*, a proxy for phytoplankton biomass, at station SH is consistently higher than at station LB. The same is true for the growth of the barnacle *Balanus glandula* and the mussel *Mytilus califor-*

nianus and production of their larvae (Leslie et al., 2005). The seasonal development of this circulation pattern is quite important, as the major recruitment pulses of *B. glandula* appear to occur during the summer or fall (Barth et al., 2007), when the along-shelf upwelling circulation differences are most prevalent. Thus, the availability of phytoplankton in the nearshore and larval transport and recruitment could be significantly altered by the circulation differences described above, potentially causing the variations seen. While previous studies (Barth et al., 2005a) have suggested these implications, our inner-shelf results contain much stronger evidence of the effects of circulation on rocky intertidal growth and recruitment. In addition, naturally occurring hypoxia over and onshore of the bank, recently outlined by Grantham et al. (2004), appears to be caused in part by these circulation differences and the ecological variations they impart. The details of these effects will be investigated in a future paper.

3.7. Summary

The results presented here show the nature and variability of inner-shelf circulation along the central Oregon coast during summer upwelling conditions. Upwelling circulation at the northernmost station, north of an offshore submarine bank, is similar to classic 2D upwelling with bottom stress and acceleration balancing the wind stress in the along-shelf momentum balance. Along-shelf velocities here are strong with large variations in magnitude and direction. In contrast, circulation at the southern three inner-shelf stations, all onshore of the bank, is weaker and prone to large reversals under downwelling conditions. At these sites, the 2D balance is poor during upwelling winds and inclusion of the along-shelf pressure gradient and nonlinear terms improves the along-shelf momentum balance. During downwelling conditions the 2D balance holds well at the southern sites, but poorly at the northern site.

Much of the variability is due to the interaction of the mid-shelf upwelling jet and an offshore submarine bank, as along-shelf winds and inner-shelf bathymetry are mostly uniform in the along-shelf direction throughout the region. Because of this interaction, stations onshore of the bank are sheltered from the stronger, southward upwelling jet offshore and to the north. A smaller, secondary upwelling jet (the 'mini-jet') develops at the on-bank inner-shelf locations, strengthening to the south. These effects were both time and space dependent as conditions were similar early in the season with along-shelf differences developing over time to the south. An empirical orthogonal function analysis of pressure anomaly, along-shelf velocity, across-shelf surface transport, and mid-water density found two important patterns of variability. The first pattern, explaining some off-bank but nearly all the on-bank variability, is associated with the local wind forcing. The second pattern explains the bulk of the off-bank variability, and contributes additional across-shelf transport at this station. The variability shown influences the coastal marine ecosystem and begins to explain known along-shelf trends in biological productivity in the region.

This study gives a picture of the inner-shelf response to wind forcing during the summer upwelling season in an area of complex bathymetry and shows the importance of the inner-shelf in shelf-wide dynamics. Our analysis of the depth-averaged along-shelf momentum balance examines both time series interactions and mean regime balances. The combined picture that emerges from correlated term relationships as well as regime mean balances gives insight into the underlying dynamics. However, large residual terms exist in both views of the momentum balance, illustrating the difficulties of closing the equation with even a substantial observational effort such as this one. These difficulties, similar to those of previous outer- and inner-shelf momentum balance studies, are not trivial to overcome. Accurately measuring the correct pressure gradients and advective terms on spatial scales from 10 to 70 km appear to be the most challenging issues. With

this in mind, future dynamical studies focusing on the on-bank 'mini-jet' stations due to their sheltered location, along-shelf similarities, and simplified response to local wind forcing have great potential to further our understanding of the evolution of upwelling and event-scale variability of the inner-shelf.

3.8. Appendix: Calculating pressure anomaly from bottom pressure

In dynamical studies such as this one, the mean and linear trend of a bottom pressure record are not important to the balances we consider. Eliminating them from the record isolates the pressure anomaly from the effects of any long-term spatial movements of the instrument's platform as well as any instrument drift. However, PISCO's sensors were also subjected to episodic shifts of the bottom landers relative to mean sea level (anchor shifts). A procedure was developed to account for these sudden motions using sharp changes in the heading, pitch, and roll of the instrument to identify and eliminate time periods of platform movement. This technique is described below.

Our method uses two assumptions to identify anchor shifts. We assume that vertical movements of the sensor (i.e. pressure shift) are associated with changes in the attitude or orientation of the instrument, but that the magnitude of the attitude change is not necessarily related to the magnitude of the vertical change. Secondly, the platform only moves downward relative to mean sea level as it settles on the bottom over time, so the mean pressure trend must increase over time. Using the first assumption to find all shifts in a deployment, a metric of total platform movement is created by summing first differences of the hourly heading, pitch, and roll measurements and then integrating the sum over each day. This metric, the total daily change in orientation (measured in degrees), accentuates areas of high change. Using a threshold level set by inspection (2.3 degrees per day), all days with total changes above the threshold are considered potential

anchor shifts and flagged. The residual, detided pressure records are scanned, calculating local mean pressures for each unflagged section. The second test is applied here. Working through the time series from beginning to end, where the local mean pressure decreases between adjacent unflagged sections, a vertical shift did not occur, and the local mean pressure is recalculated including both unflagged sections as well as the flagged data in between. If the mean pressure increases between adjacent unflagged sections, a vertical shift is assumed and the flagged section is removed. After applying this procedure, the time series of local mean pressures, from the remaining unflagged sections, is subtracted from the measured pressure, resulting in pressure anomaly.

This process, while saving the maximum amount of data possible, introduces potential errors as the 'mean pressure' could be defined over different time-scales for different stations. Thus the zero crossing of a pressure anomaly and the pressure gradient might be in error. For the 2004 data, the occurrence of this type of error is limited to the first 40 days of the initial deployment date (days 133-135) of the bottom landers as no shifts were identified after day 170. A comparison of the corrected bottom pressure anomaly records with the Newport adjusted sea level (Figure 3.2) finds good agreement and strong correlations both during this initial month as well as during the rest of the study period (Tables 3.3 and 3.4).

3.9. Acknowledgments

This paper is a contribution of PISCO, the Partnership for Interdisciplinary Studies of Coastal Oceans funded primarily by the Gordon and Betty Moore Foundation and David and Lucile Packard Foundation. We thank J. Lubchenco and B. Menge in establishing and maintaining the PISCO observational program at OSU. Additional support for JAB was provided by National Science Foundation Grant OCE-9907854. We also thank Captain P.

York, C. Holmes, and S. Holmes for their data collection efforts and M. Levine, E. Dever, J. Allen, and J. Huyer for their helpful comments on the manuscript.

BIBLIOGRAPHY

Allen, J. and R. Smith, 1981: On the dynamics of wind-driven shelf currents. *Phil. Trans. R. Soc. Lond.*, **A302**, 617–634.

Barth, J., B. Menge, J. Lubchenco, F. Chan, J. Bane, A. Kirincich, M. McManus, K. Nielsen, S. Pierce, and L. Washburn, 2007: Delayed upwelling alters nearshore coastal ocean ecosystems in the northern California Current. *PNAS*, **104**, 3719–3724.

Barth, J., S. Pierce, and R. Castelao, 2005a: Time-dependent, wind-driven flow over a shallow midshelf submarine bank. *J. Geophys. Res.*, **110**, doi:2004JC002761.

Barth, J., S. Pierce, and T. Cowles, 2005b: Mesoscale structure and its seasonal evolution in the northern California Current System. *Deep Sea Res. II*, **52**, 5–28.

Battisti, D. and B. Hickey, 1984: Application of remote wind-forced coastl trapped wave theory to the Oregon and Washington coasts. *J. Phys. Ocean.*, **14**, 887–903.

Castelao, R. and J. Barth, 2005: Coastal ocean response to summer upwelling favorable winds in a region of alongshore bottom topography variations off Oregon. *J. Geophys. Res.*, **110**, doi:10.1029/2004JC002409.

Chapman, D., 1987: Application of wind-forced, long, coastal-trapped wave theory along the California coast. *J. Geophys. Res.*, **92**, 1798–1816.

Cutchin, D. and R. Smith, 1973: Continental shelf waves: low-frequency variations in sea level and currents over the Oregon continental shelf. *J. Phys. Ocean.*, **3**, 73–82.

Davis, R., 1976: Predictability of sea surface temperature and sea level pressure anomalies over the North Pacific Ocean. *J. Geophys. Res.*, **90**, 4741–4755.

Federiuk, J. and J. Allen, 1995: Upwelling on the Oregon continental shelf. Part II: simulations and comparisons with observations. *J. Phys. Ocean.*, **25**, 1867–1884.

Gan, J. and J. Allen, 2002: A modeling study of shelf circulation of northern California in the region of the Coastal Ocean Dynamics Experiment: Response to relaxation of upwelling winds. *J. Geophys. Res.*, **107**, doi:10.1029/2000JC000768.

— 2005: Modeling upwelling circulation off the Oregon coast. *J. Geophys. Res.*, **110**, doi:10.1029/2004JC002692.

Gordon, R., 1996: *Acoustic Doppler Current Profiler: principles of operation, a practical primer Second edition for Broadband ADCPs*. RDI Instruments, 54 pp.

Grantham, B., F. Chan, K. Nielsen, D. Fox, J. Barth, A. Huyer, J. Lubchenco, and B. Menge, 2004: Upwelling-driven nearshore hypoxia signals ecosystem and oceanographic changes in the northeast Pacific. *Nature*, **429**, 749–754.

Huyer, A., J. Fleischbein, J. Keister, P. Kosro, N. Perlin, R. Smith, and P. Wheeler, 2005: Two coastal upwelling domains in the northern California Current System. *J. Mar. Res.*, **63**, 901–929.

Huyer, A., B. Hickey, J. Smith, R. Smith, and R. Pillsbury, 1975: Alongshore coherence at low frequencies in currents observed over the continental shelf off Oregon and Washington. *J. Geophys. Res.*, **80**, 3495–3505.

Huyer, A., R. Smith, and R. Pillsbury, 1974: Observations in a coastal upwelling region during a period of variable winds (Oregon coast, July 1972). *Tethys.*, **6**, 391–404.

Huyer, A., R. Smith, and E. Sobey, 1978: Seasonal differences in low-frequency current fluctuations over the Oregon continental shelf. *J. Geophys. Res.*, **83**, 5077–5089.

Kirincich, A., J. Barth, B. Grantham, B. Menge, and J. Lubchenco, 2005: Wind-driven inner-shelf circulation off central Oregon during summer. *J. Geophys. Res.*, **110**, doi:10.1029/2004JC002611.

Kosro, P., 2005: On the spatial structure of coastal circulation off Newport, Oregon, during spring and summer 2001 in a region of varying shelf width. *J. Geophys. Res.*, **110**, doi:10.1029/2004JC002769.

Kundu, P. and J. Allen, 1976: Some three-dimensional characteristics of low-frequency current fluctuations near the Oregon coast. *J. Phys. Ocean.*, **6**, 181–199.

Kundu, P., J. Allen, and R. Smith, 1975: Modal decomposition of the velocity field near the Oregon coast. *J. Phys. Ocean.*, **5**, 683–704.

Large, W. and S. Pond, 1981: Open ocean momentum flux measurements in moderate to strong winds. *J. Phys. Ocean.*, **11**, 324–336.

Lentz, S. and D. Chapman, 2004: The importance of nonlinear cross-shelf momentum flux during wind-driven coastal upwelling. *J. Phys. Ocean.*, **34**, 2444–2457.

Lentz, S., R. Guza, S. Elgar, F. Feddersen, and T. Herbers, 1999: Momentum balances on the North Carolina inner shelf. *J. Geophys. Res.*, **104**, 18205–18226.

Lentz, S. and C. Winant, 1986: Subinertial currents on the southern California shelf. *J. Phys. Ocean.*, **16**, 1737–1750.

Leslie, H., E. Breck, F. Chan, J. Lubchenco, and B. Menge, 2005: Barnacle reproductive hotspots linked to nearshore ocean conditions. *PNAS*, **102**, 0534–10539.

Menge, B., B. Daley, P. Wheeler, E. Dahlhoff, E. Sanford, and P. Strub, 1997: Benthic-pelagic links and rocky intertidal communities: Bottom-up effects on top-down control? *PNAS*, **94**, 14530–14535.

Menge, B., E. Sanford, B. Daley, T. Freidenburg, G. Hudson, and J. Lubchenco, 2002: An inter-hemispheric comparison of bottom-up effects on community structure: insights revealed using the comparative-experimental approach. *Ecological Research*, **17**, 1–16.

Mooers, C. and R. Smith, 1968: Continental shelf waves off Oregon. *J. Geophys. Res.*, **73**, 549–557.

Oke, P., J. Allen, R. Miller, G. Egbert, J. Austin, J. Barth, T. Boyd, P. Kosro, and M. Levine, 2002a: A modeling study of the three-dimensional continental shelf circulation off Oregon. Part I: model-data comparisons. *J. Phys. Ocean.*, **32**, 1360–1382.

— 2002b: A modeling study of the three-dimensional continental shelf circulation off Oregon. Part II: dynamical analysis. *J. Phys. Ocean.*, **32**, 1383–1403.

Pawlowicz, R., B. Beardsley, and S. Lentz, 2002: Classical tidal harmonic analysis including error estimates in MATLAB using T_TIDE. *Computers and Geosciences*, **28**, 929–937.

Perlin, A., J. Moum, J. Klymak, M. Levine, T. Boyd, and P. Kosro, 2005: A modified law-of-the-wall applied to oceanic bottom boundary layers. *J. Geophys. Res.*, **110**, doi:10.1029/2004JC002310.

Samelson, R., P. Barbour, J. Barth, S. Bielli, T. Boyd, D. Chelton, P. Kosro, M. Levine, and E. Skyllingstad, 2002: Wind stress forcing of the Oregon coastal ocean during the 1999 upwelling season. *J. Geophys. Res.*, **107**, doi: 10.1029/2001JC00900.

Smith, R., 1974: A description of current, wind, and sea level variations during coastal upwelling off the Oregon coast, July/August 1972. *J. Geophys. Res.*, **79**, 435–443.

Smith, R., A. Huyer, and J. Fleischbein, 2001: The coastal ocean off Oregon from 1961 to 2000: is there evidence of climate change or only of Los Ninos? *Prog. Ocean.*, **29**, 63–93.

	Station/deployment					
	LB	**YB**	**LB**	**SR**	**YB**	**SH**
	early season		*late season*			
Latitude (° ' N)	44 51.500	44 19.328	44 51.500	44 30.300	44 19.328	44 15.140
Longitude (° ' W)	124 03.374	124 07.257	124 03.374	124 06.100	124 07.257	124 07.641
start day	133	135	192	191	190	191
end day	192	188	272	253	247	253
			Instrumentation			
Depth (m)						
1	TBT	XTI	TBT	XTI	XTI	TBT
4	TBT	XTI	TBT	XTI	XTI	TBT
8		SBE37		SBE37	SBE37	SBE16
9	TBT	XTI	TBT	XTI	XTI	TBT
11	SBE16		SBE16			SBE16
14	TBT	TBT	XTI	XTI	XTI	TBT
14.5	WH600	WH600	WH600	WH600	WH600	WH600
			Velocity statistics (m s^{-1})			
Along-shelf						
mean	-0.068	-0.007	-0.034	0.023	-0.015	-0.041
std dev	0.086	0.117	0.091	0.101	0.120	0.113
Across-shelf						
mean	0.002	-0.003	-0.004	-0.000	0.001	0.005
std dev	0.010	0.013	0.017	0.010	0.007	0.007
PA direction (^{o})	24	8	23	1	10	7
C_f (x10^3)	1.9	0.7	3.4	2.3	1.3	1.6

TABLE 3.1: The 2004 PISCO mooring deployments. XTI and TBT are Onset XTI and Tidbit temperature loggers, SBE16 and SBE37 are Seabird CT loggers, and WH600 are RDI Workhorse 600kHz ADCPs, with integrated pressure and temperature sensors. Velocity statistics are presented for the depth-averaged along and across-shelf velocities. The principal axis of flow (PA), in degrees east of true North, and the calculated quadratic drag coefficient (C_f) for each deployment are listed as well.

	% Variance					Amplitude			
MODE	Total	LB	SR	YB	SH	LB	SR	YB	SH
	Pressure anomaly (P dB)								
1	77	40	94	86	89	-0.70	-0.93	-1.31	-0.98
2	17	59	0	8	2	1.80	0.11	-0.82	-0.28
3	6	1	3	6	14	-0.38	0.55	-1.25	1.41
	Along-shelf velocity (V m s^{-1})								
1	79	33	69	95	84	-0.66	-1.01	-1.16	-1.10
2	14	60	2	3	5	1.75	0.24	-0.41	-0.84
3	6	8	28	0	9	-0.70	1.60	-0.02	0.99
	across-shelf surface transport (Us m^3 s^{-1})								
1	73	47	68	78	86	-0.59	-1.06	-0.90	-1.30
2	14	1	31	3	8	0.22	-1.68	0.42	0.97
3	5	52	0	1	2	1.89	-0.13	-0.25	-0.58
	Density (σ_t)								
1	95	82	96	96	95	-0.87	-1.07	-1.04	-1.00
2	5	17	0	3	2	1.73	-0.04	-0.75	-0.68
3	1	0	3	0	2	-0.45	1.51	0.01	1.23

TABLE 3.2: EOF results during days 190-250 for the first three modes for pressure anomaly, depth-averaged along-shelf velocity, across-shelf surface transport, and density. The percentage of total and local variance explained by each EOF mode are listed along with modal amplitudes.

Stations	**Wind**		**LB**		**YB**	
	CC	lag	CC	lag	CC	lag
Velocity						
LB	0.71	-5	1	0		
YB	0.65	-19	0.51	-13	1	0
Pressure						
LB	0.53	-1	1	0		
YB	0.68	-7	0.83	-4	1	0
NP	0.74	13	0.72	-9	.94	0

TABLE 3.3: Early season velocity and pressure correlations. Correlations (CC) between along-shelf wind stress and depth-averaged, along-shelf velocity and pressure anomaly time-series for year days 133-190. All correlations shown were statistically significant at the 95% confidence interval. Lagged correlations are included only where they were significantly different from the zero lag correlation. A negative lag (in hours) means the horizontally listed time-series (e.g. wind) leads the vertically listed time-series.

Station	**Wind**		**LB**		**SR**		**YB**		**SH**	
	CC	lag	CC	lag	CC	lag	CC	lag	CC	lag
Velocity										
LB	0.73	-4	1	0						
SR	0.76	-3	0.55	0	1	0				
YB	0.79	-9	0.45	0	0.84	0	1	0		
SH	0.78	-12	0.53	-39	0.73	0	0.93	0	1	0
Pressure										
LB	0.42	10	1	0						
SR	0.71	-8	0.64	-9	1	0				
YB	0.53	-12	0.43	-11	0.84	0	1	0		
SH	0.60	-9	0.50	-10	0.91	0	0.79	0	1	0
NP	0.75	12	0.45	-20	0.92	0	0.79	0	0.89	0

TABLE 3.4: Late season velocity and pressure correlations. Same as Table 3.3, but for year days 190-255.

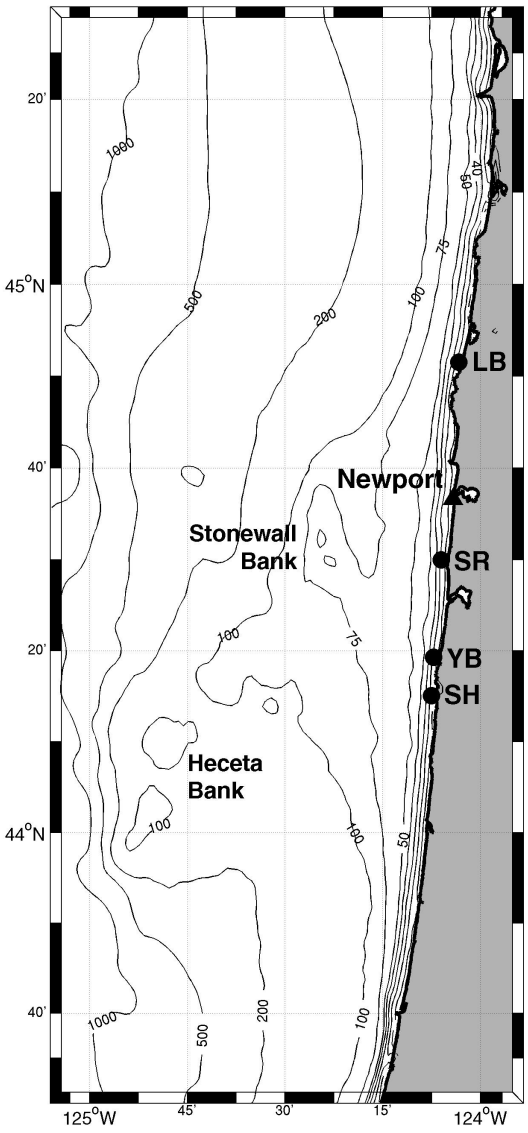

FIGURE 3.1: The central Oregon shelf. The Heceta and Stonewall Bank complex is shown by bathymetric contours offshore of the 50 m isobath and south of 44° 45' latitude. Locations of the 4 PISCO stations (bullets) and the Newport CMAN station (triangle) are shown. Bathymetry is in meters, and in 10 m increments onshore of the 50 m isobath.

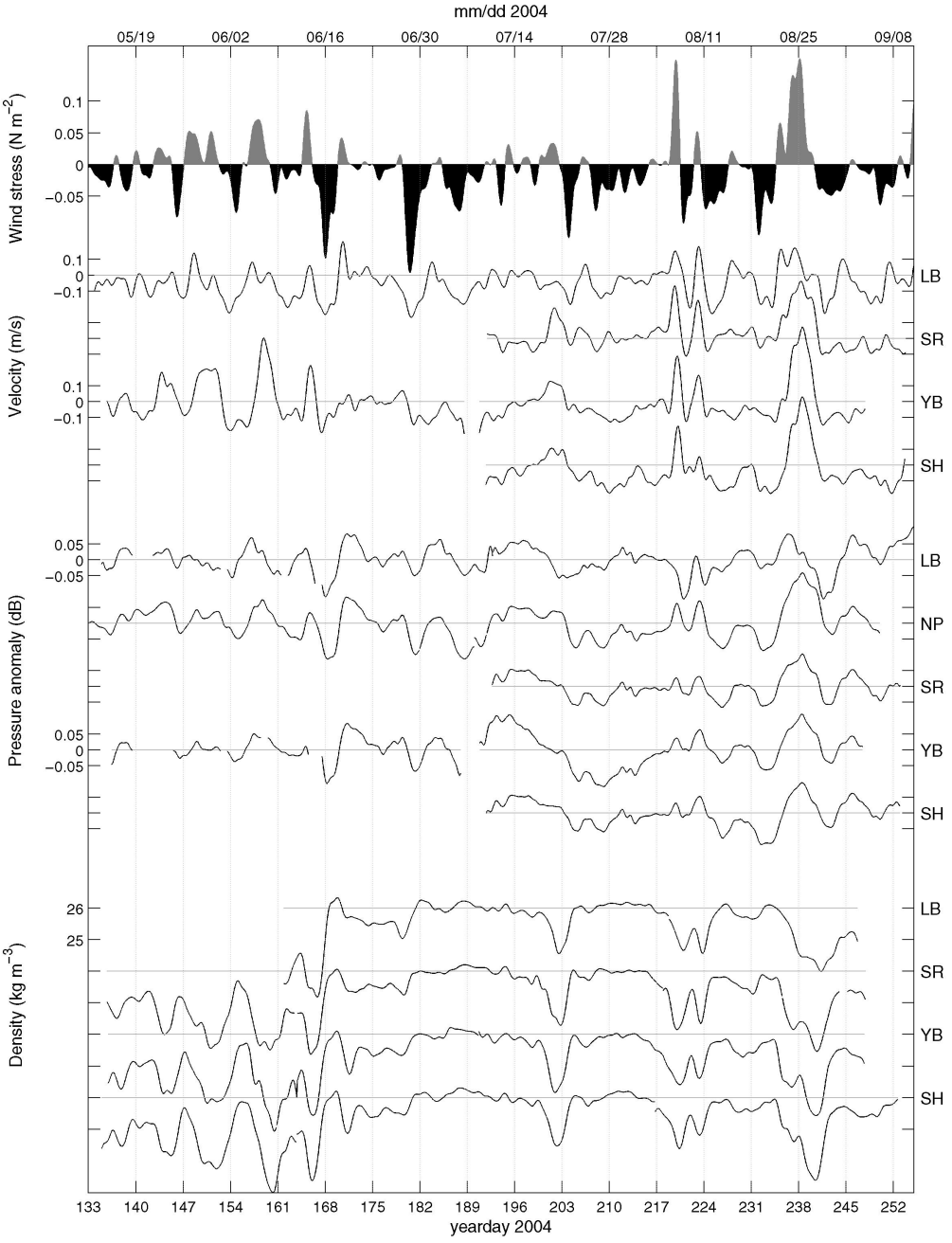

FIGURE 3.2: Inner-shelf conditions during the 2004 upwelling season. North wind stress from the Newport CMAN station is shown above offset plots of depth-averaged, along-shelf velocity (m s^{-1}), pressure anomalies (dB), and mid-water density (kg m^{-3}) from each of the 4 stations. For each type, stations are plotted north (top) to south (bottom). The Newport SSP (NP) is included among the pressure anomalies for reference. For each time series, thin lines mark the zero crossing (velocity and pressure) or 26 kg m^{-3} (density). Tick increments for each are: wind stress (0.05 N m^{-2}), water velocity (0.1 m s^{-1}), pressure (0.05 dB), and density (1 kg m^{-3}).

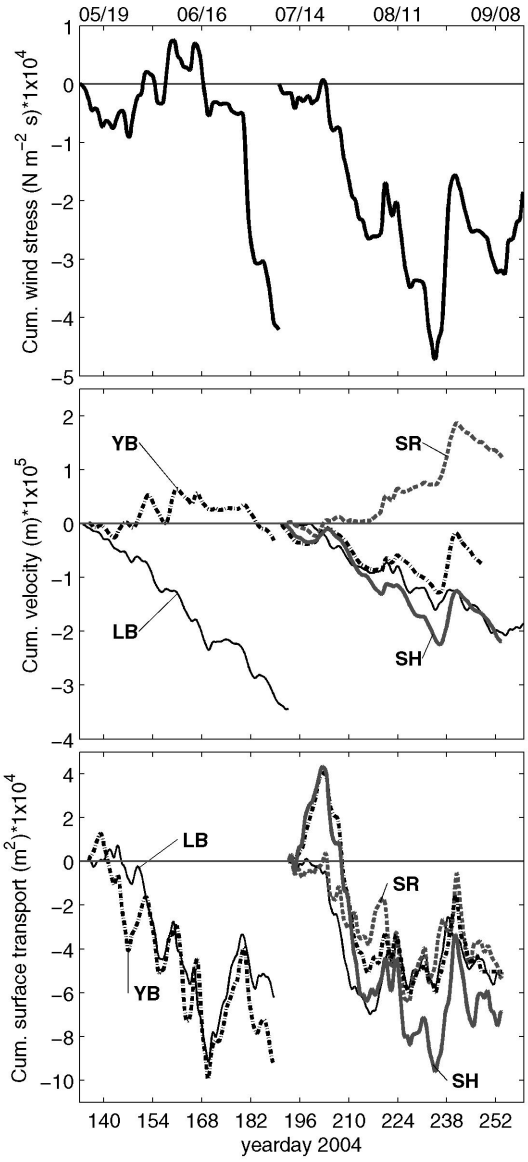

FIGURE 3.3: Cumulative along-shelf wind stress (*top*), cumulative depth-averaged along-shelf velocity (*middle*), or along-shelf displacement, and across-shelf surface transport (*bottom*) between days 133-190 (left) and days 190-273 (right).

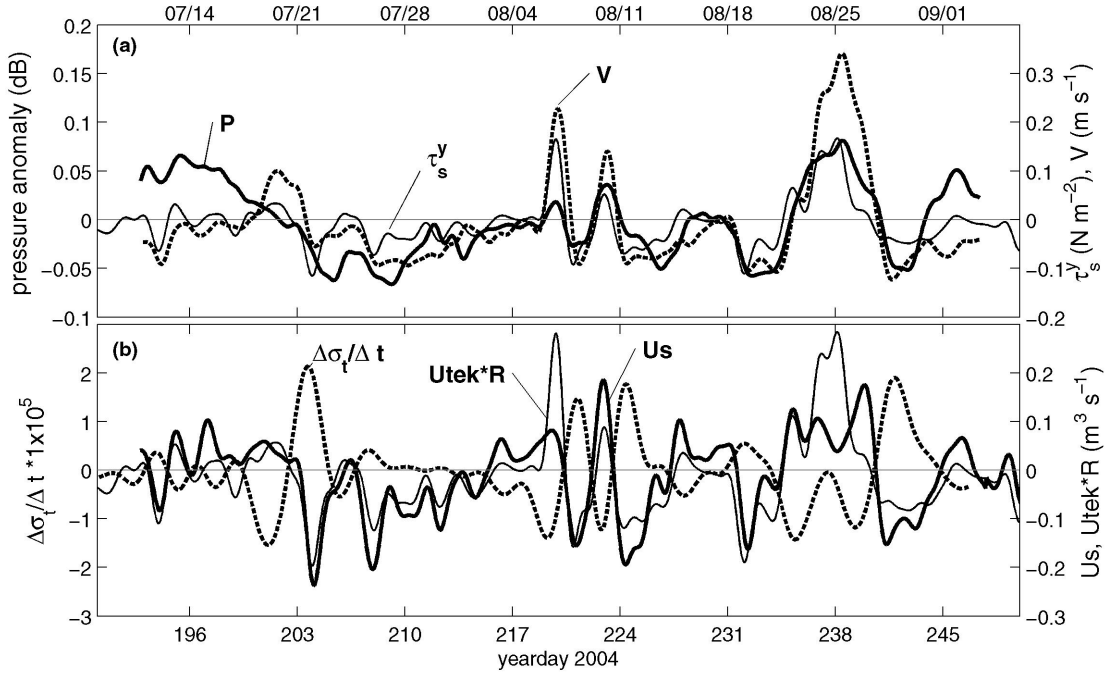

FIGURE 3.4: Mode-one EOF amplitude time series for (a) pressure anomaly and depth-averaged along-shelf velocity and (b) cross-shelf surface transport and the time rate of change of density anomaly. Along-shelf wind stress is included in (a) while the theoretical full Ekman transport (Utek), multiplied by the neutral regression coefficient (R), is included in (b).

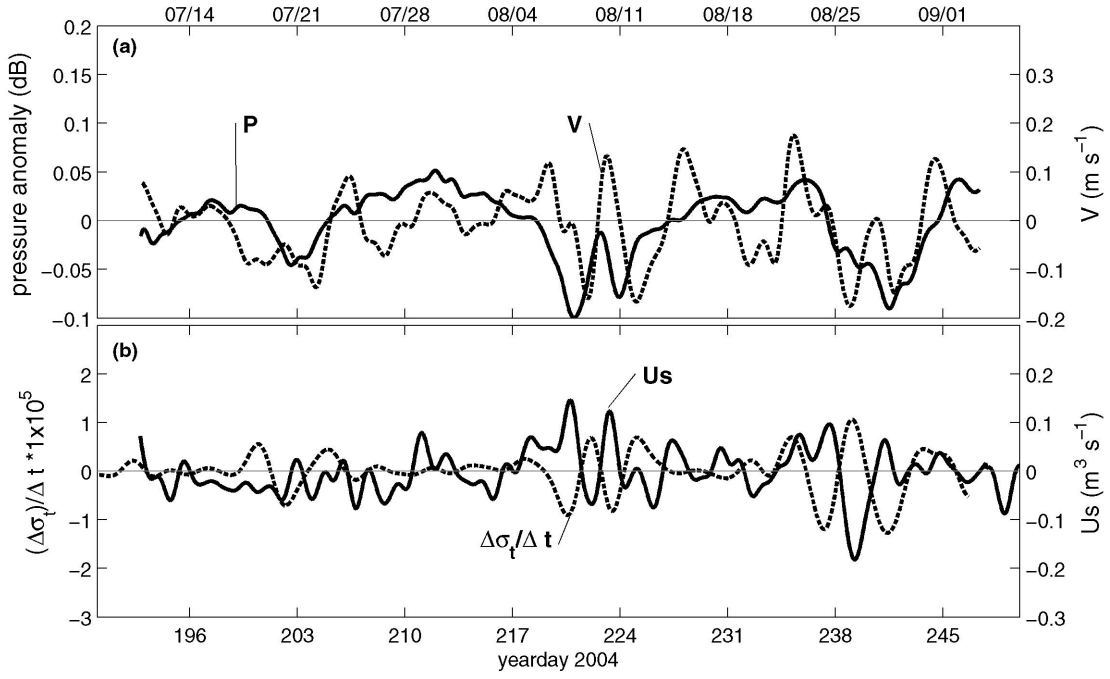

FIGURE 3.5: Mode-two EOF amplitude time series for (a) pressure anomaly and depth-averaged along-shelf velocity and (b) cross-shelf surface transport and the time rate of change of density anomaly.

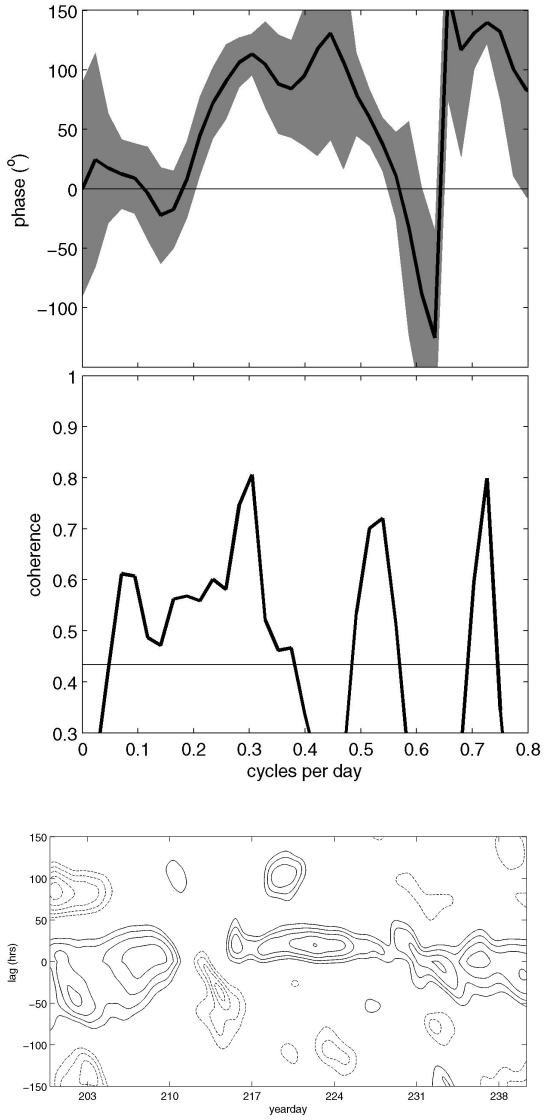

FIGURE 3.6: Phase *(top)* and coherence *(middle)* of the mode-two EOF amplitude time series for depth-averaged along-shelf velocity verses pressure anomaly. The 95% confidence interval is shaded for phase and marked by the horizontal line for coherence interval. Positive phase differences indicate where pressure leads velocity. *(bottom)* A moving two-week windowed cross-covariance between mode-two velocity and pressure. Correlation coefficients greater than +0.4 (solid) or less than -0.4 (dashed) are contoured in increments of 0.1. Positive lags indicate where pressure leads velocity.

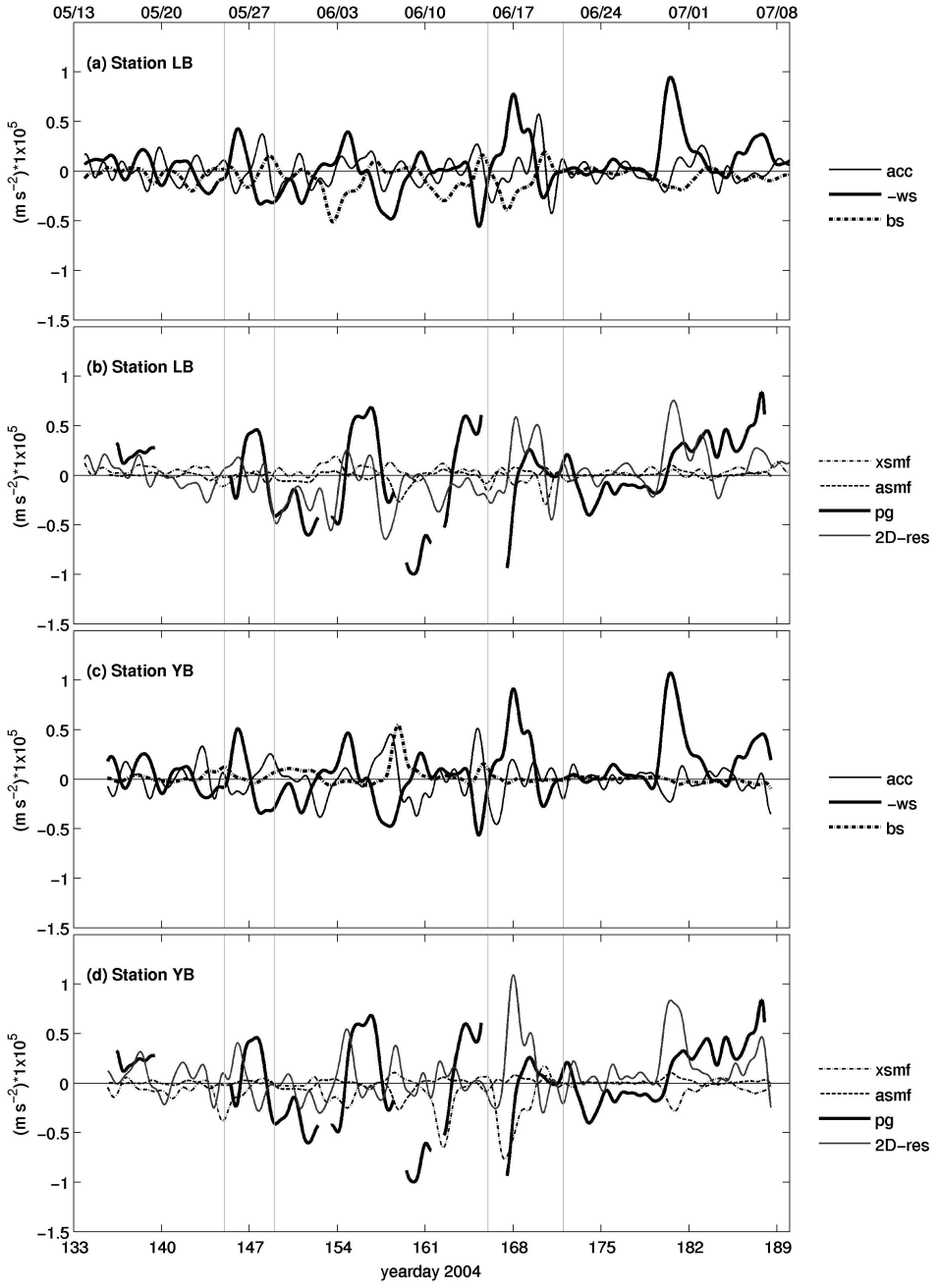

FIGURE 3.7: Terms in the depth-averaged, along-shelf momentum balance at stations LB (top 2 panels) and YB (bottom 2 panels) for days 133-190. Vertical gray lines denote time periods referred to in the text. Legend labels are as follows: (*acc*) acceleration, (*ws*) wind stress, (*bs*) bottom stress, (*xsmf*) across-shelf momentum flux, (*asmf*) along-shelf momentum flux, (*pg*) pressure gradient, (*2D-res*) sum of the acceleration and stresses.

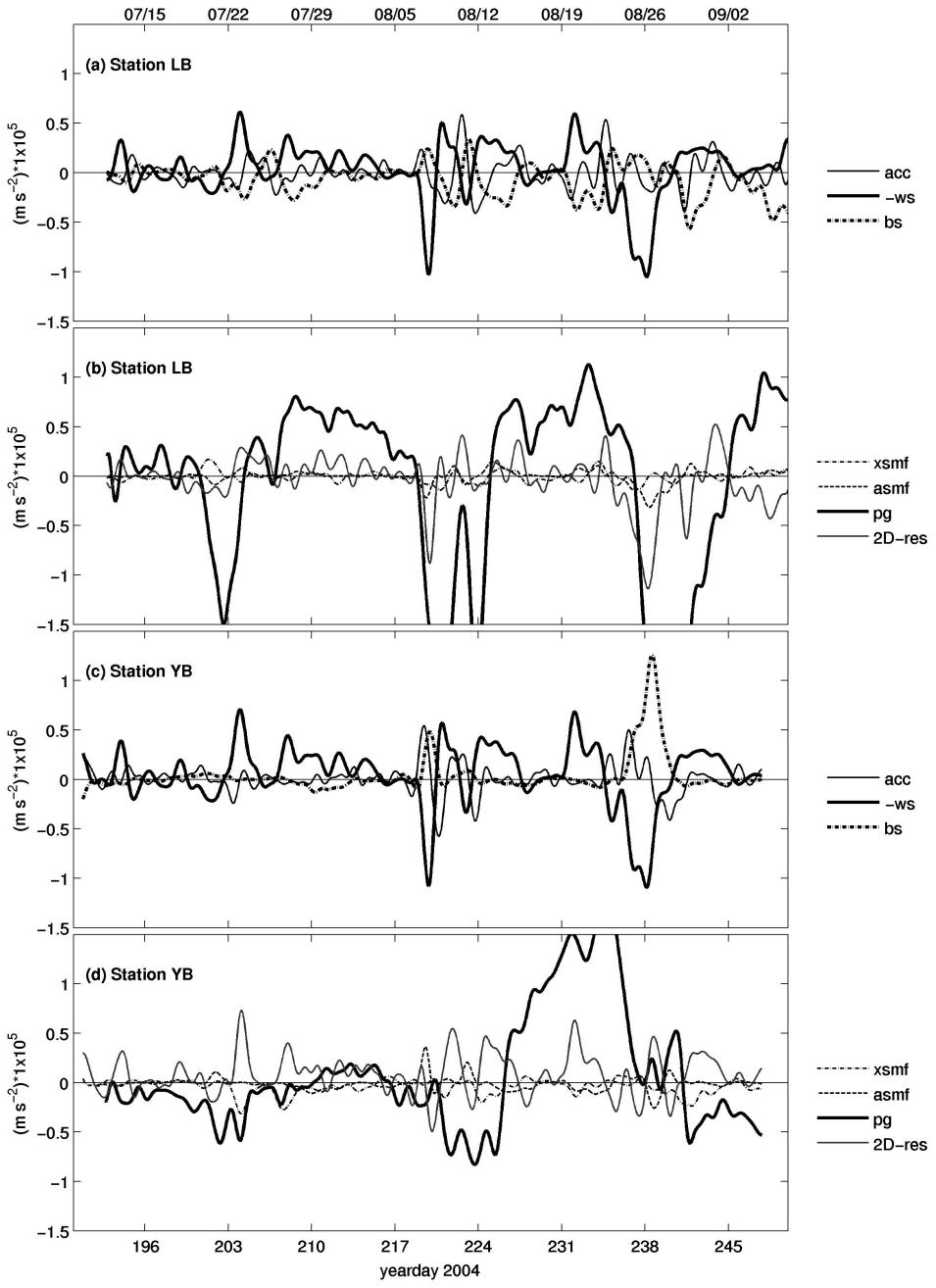

FIGURE 3.8: Terms in the depth-averaged, along-shelf momentum balance at stations LB (top 2 panels) and YB (bottom 2 panels) for days 190-250. Legend labels are the same as in Figure 3.7.

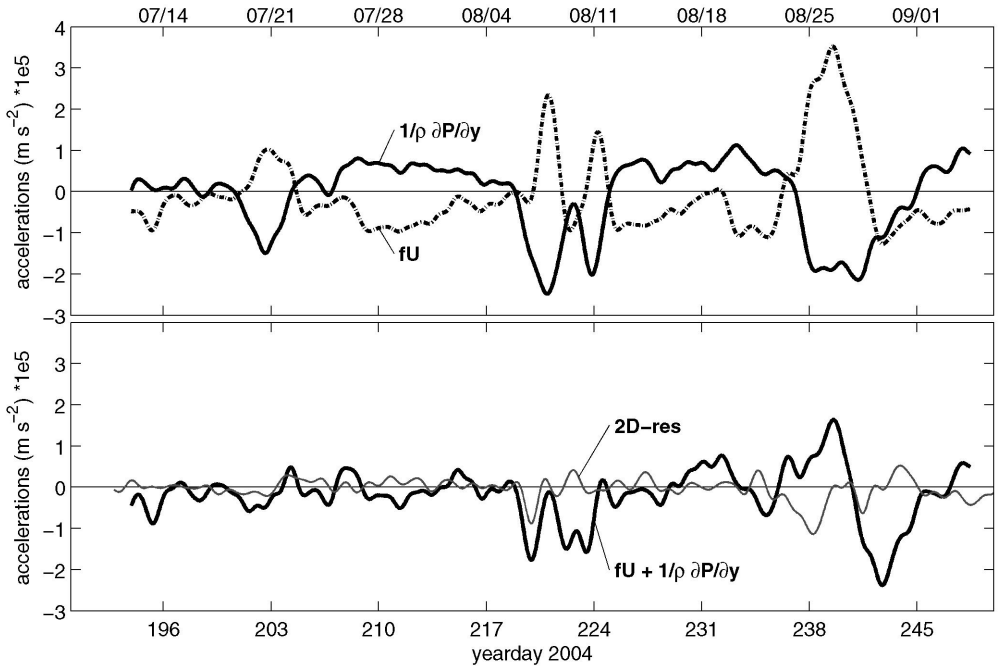

FIGURE 3.9: Illustrating the source of the unbalanced pressure gradient at LB during days 190-250. (a) shows the along-shelf LB-SR pressure gradient (solid) from Figure 3.8b along with the mode-one velocity EOF, lagged by 26 hrs (see text) and multiplied by f, as an estimate of fU. The sum of these terms, assumed to be the actual along-shelf pressure gradient at LB (black solid) is shown in (b) with *2D-res* from station LB during this time period (gray solid).

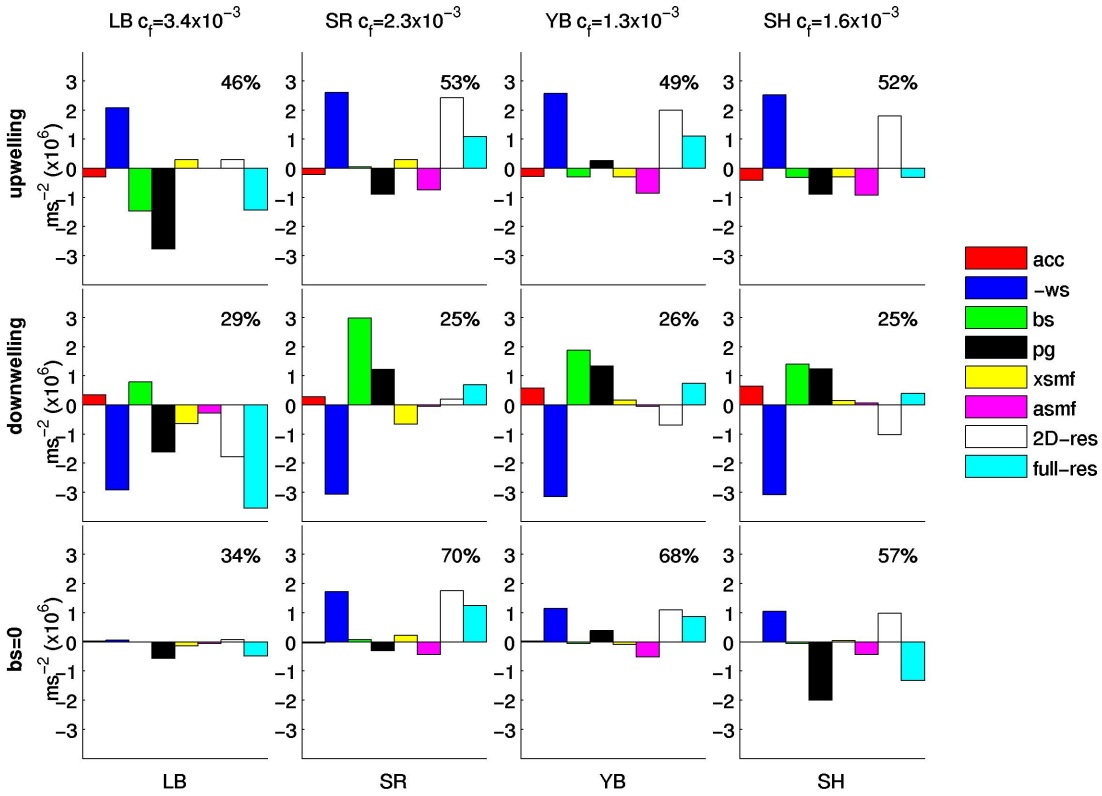

FIGURE 3.10: Mean values for depth-averaged, along-shelf momentum balance terms during days 190-260 under the following conditions: negative (upwelling favorable) wind stress (*top row*), positive (downwelling favorable) wind stress (*middle row*), and near-zero bottom stress (*bottom row*). In each panel the percent of the total time represented by that regime is listed. Residuals, summations of the appropriate terms, from the classic 2D balance (2D-res) and the full equation (full-res) are included on the right side of each panel. Legend labels are the same as in Figure 3.7

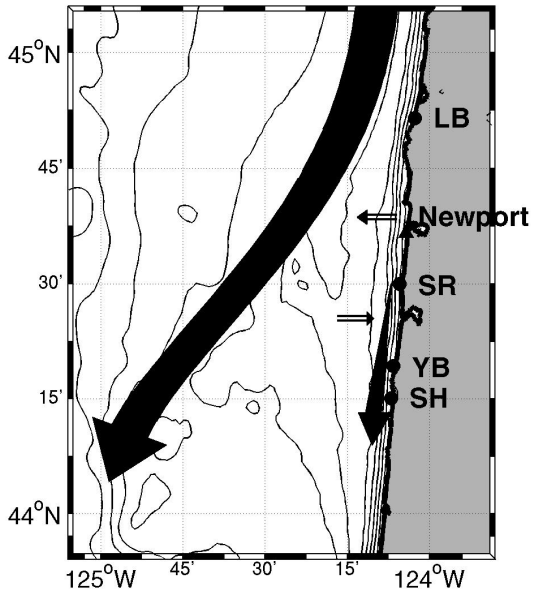

FIGURE 3.11: Cartoon of regional upwelling circulation on the central Oregon shelf during late summer. The core of the coastal jet (large solid arrow) is diverted offshore and around the Heceta and Stonewall Bank complex by flow-topography interactions which cause offshore, cross-isobath transport north of station SR (small open arrow). In the lee of this circulation a smaller upwelling jet (small solid arrow) spins up in the inner-shelf south of Newport. The region offshore of this secondary jet, and over the bank, is characterized by weak, onshore velocities (small open arrow).

4. TIME-VARYING ACROSS-SHELF EKMAN TRANSPORT AND VERTICAL EDDY VISCOSITY ON THE INNER-SHELF.

Anthony R. Kirincich and John A. Barth

Journal of Physical Oceanography

45 Beacon Street, Boston, MA 02108-3693

To be submitted

Abstract

We investigated the event-scale variability of across-shelf transport using observations made in 15 m of water on the central Oregon inner-shelf. Hydrographic and velocity observations from the study area, located in an area of intermittently upwelling-favorable winds and significant density stratification that is sheltered from the larger regional circulation, show rapid across-shelf movement of water masses and variable residence times. Conditions change from weak stratification and strong northward currents during downwelling favorable winds to stronger stratification and southward currents in thermal wind balance with density gradients during upwelling favorable winds over event timescales of 2-7 days. To better understand the time variability of across-shelf exchange, an inverse calculation is used to estimate eddy viscosity and vertical turbulent diffusion of momentum from profiles of velocity and wind forcing. Depth-averaged estimated eddy viscosity varied over a large dynamic range, averaging $0.8\text{x}10^{-3}$ m^2 s^{-1} during upwelling winds and $2.1\text{x}10^{-3}$ m^2 s^{-1} during downwelling winds. The fraction of full Ekman transport present in the surface layer, a measure of the efficiency of across-shelf exchange at this water depth, was a strong function of the eddy viscosity. Transport fractions ranged from 80-100% during times of rapidly changing stratification and forcing, and low eddy viscosity, to 10-20% during times of weak stratification, strong forcing, and high eddy viscosity. The difference in eddy viscosities between upwelling and downwelling led to varying across-shelf exchange efficiencies and, potentially, increased net upwelling over time. These results quantify the variability of across-shelf transport efficiency and have significant implications for ecological processes (e.g., larval transport) in the inner-shelf.

4.1. Introduction

The mechanisms of across-shelf transport of water masses (and therefore nutrients, detritus, phytoplankton, sediments, pollutants, and larvae) in the inner-shelf on wind-driven shelves are of significant scientific and public interest, controlling movement and access between the stratified coastal ocean and the well-mixed surf zone. Recent studies (Lentz, 2001; Kirincich et al., 2005) have reported that the exchange driven by the along-shore wind decreases in relation to the total Ekman transport as the coast is approached, from 100% of full Ekman transport in water depths of 50 m to 25% in water depths of 15 m. This trend is based on mean results, averaged over seasonal (60-120 d) time periods. In contrast, wind-driven circulation varies over much shorter (2-7 d) time scales, and thus the factors that control this transport divergence may vary significantly. In this paper, we investigate inner-shelf upwelling dynamics using moored and shipboard observations from the central Oregon coast in an attempt to quantify the variability of across-shelf exchange during the upwelling season.

The central Oregon shelf is forced by upwelling favorable winds with small offshore wind stress curl during the spring and summer months (Samelson et al., 2002; Kirincich et al., 2005). By late spring the Columbia River plume, the primary source of buoyancy for the Pacific Northwest, is pushed offshore by seasonal winds, leaving shelf waters well stratified in both temperature and salinity for the remainder of the season (Huyer, 1983). Throughout this time, intermittent downwelling wind bursts, occurring on periods of 5-20 d, lead to large variations in local circulation and hydrographic conditions. The timing of these events, controlled by large-scale atmospheric variations (Bane et al., 2005), have enormous consequences for marine ecosystems in the region (Barth et al., 2007). During the summer of 2004, the Partnership for Interdisciplinary Studies of Coastal Oceans (PISCO) program maintained moorings at four along-shelf stations in 15 m of water along

the central Oregon coast (Figure 4.1). Previously, Kirincich and Barth (2007) used these observations to describe the temporal and spatial development of upwelling circulation. Summarizing their results, the three stations inshore of an offshore submarine bank, Seal Rock (SR), Yachats Beach (YB), and Strawberry Hill (SH), are sheltered from the regional upwelling circulation and its southward jet, yet still exposed to the regional wind forcing. Inshore of the bank, a smaller upwelling jet forms in the inner-shelf near station SR and strengthens to the south. Hydrographic and velocity variability at these 'on-bank' stations (SR, YB, and SH) are well correlated with the local wind forcing. Thus a small-scale upwelling system, driven by local wind forcing exists in the lee of the bank. In this paper, we focus on observations made by PISCO of this 'mini-jet' at the southern-most station (SH) to describe the effects of intermittent forcing on inner-shelf upwelling circulation.

We define the inner-shelf as the region where across-shelf Ekman transport is divergent and coastal upwelling actively occurs. In this region, the thickness and amount of overlap of the surface and bottom boundary layers control the location of upwelling and the local volume of across-shelf transport. In its simplest form, assuming waters are unstratified, Ekman layer theory (Ekman, 1905) relates the boundary layer thickness (d) to a vertical eddy viscosity (A) through $d = (2A/f)^{1/2}$, where f is the Coriolis parameter. Using an eddy viscosity allows us to parameterize the transfer of momentum due to turbulent eddies as a function of the vertical shear of the horizontal velocities. Applied along a sloping shelf with a constant eddy viscosity (A=0.08 m^2 s^{-1} following Ekman (1905); Mitchum and Clarke (1986)), this solution reaches the full theoretical Ekman value (100% transport fraction) at water depths of 160 m. The difference in the water depth of full transport seen between the stratified observations (Lentz, 2001; Kirincich et al., 2005) and this unstratified constant eddy viscosity solution exists as density stratification acts to decrease the thickness of the boundary layers, and therefore the across-shelf scale of upwelling. As stratification varies at these inner-shelf locations, due to seasonal hydrographic

changes and intermittent upwelling and downwelling, the boundary layer thickness and the fraction of full transport should also vary. This has direct implications for across-shelf exchange of water masses in the inner-shelf and the ecological processes that depend on it.

While the physical mechanisms controlling across-shelf exchange are well-studied in coastal regions dominated by buoyant plumes (Wiseman and Garvine, 1995; Yankovsky et al., 2000; Garvine, 2004), both observational and modeling studies of wind-driven inner-shelf dynamics have had difficulties resolving across-shelf transport. Across-shelf velocities are generally an order of magnitude smaller than mean along-shelf velocities, tidal motions, and wave orbital velocities. Thus, errors due to measurement biases or the choice of coordinate systems can easily overwhelm the analysis. Further, incorrect assumptions on forcing or lack of measurements to resolve the appropriate spatial scales inhibit proper closure of momentum balances. If the coastal boundary and bathymetry are locally straight and uniform, analytical models can capture the majority of the along-shelf variability of wind- or pressure-driven inner-shelf systems during weakly stratified conditions (Lentz and Winant, 1986; Lentz, 1994). However, across-shelf currents and stratified conditions are more difficult to properly represent, in part due to an over-oversimplification of vertical diffusion of momentum in these models.

More recent work with two-dimensional (2D) numerical models and higher-order turbulent closure schemes have investigated circulation during the spin-up of wind events (Austin and Lentz, 2002) and realistic wind forcing (Kuebel Cervantes et al., 2003) with some success. In their parameterizations of vertical turbulent momentum, eddy viscosity is function of the distance from the boundary, local stratification, as well as instantaneous velocity and velocity shear (Mellor and Yamada, 1982). Both model studies have noted the dynamical differences in across-shelf transport between upwelling and downwelling in the inner shelf. Using a constant wind forcing, Austin and Lentz (2002) saw across-

shelf transport decrease as stratification decreased and vertical diffusion of momentum increased. Using bulk calculations, the observations of Kirincich et al. (2005) point to a similar but weaker relationship between stratification and the fraction of full Ekman transport present. Kuebel Cervantes et al. (2003) noted the importance of the non-linear advective terms on the depth-dependent momentum balance during upwelling even in very shallow (<10 m) water depths. During downwelling, a more simple balance between surface and bottom stress was seen. In both these model studies, the calculation of eddy viscosity, as well as the vertical diffusion of momentum term, were critical to the dynamical descriptions given.

Our analysis of the event scale (2-7 d) upwelling dynamics would also benefit from estimates of the vertical turbulent diffusion of horizontal momentum, as it should be the ultimate control of boundary layer thickness, the amount of overlap, and the efficiency of across-shelf Ekman transport. However, the complex measurements necessary to directly measure the turbulent fluxes are rarely made in the inner-shelf, and never for the extended deployment periods that encompass forcing events. Thus, we use a novel approach to estimate this term by inverting the one-dimensional (1D) model of Lentz (1994) to solve for eddy viscosity and vertical turbulent diffusion given a known surface forcing and the observed velocity profiles. The novelty of this approach is that a pressure gradient matching technique is developed to account for unknown sources (or sinks) of momentum while keeping the form of vertical diffusion intact. A secondary benefit to this inverse calculation is the estimation, through an analysis of the residual terms, of what sources (or sinks) of momentum were neglected from the calculation. From a dynamical standpoint, the estimated eddy viscosity contains the combined effects of stratification and forcing variability on vertical diffusion of momentum and thus across-shelf transport. Using the estimated eddy viscosity, we are able to explain the event-scale variability of across-shelf circulation in the study area.

In this paper we describe the short time-scale (2-7 days) variability of inner-shelf circulation, hydrography and forcing along the central Oregon coast during summer and document the dependence of across-shelf transport on an estimate of vertical turbulent diffusion. The data sources and methods used are introduced first (Section 2), followed by a detailed description of the event-scale variability of circulation in the study area (Section 3). We then describe the inverse calculation method (Section 4), and its general results (Section 5), before discussing the influence of the estimated eddy viscosity on the inner-shelf circulation present (Section 6). Finally, we conclude by summarizing our findings and their implications (Section 7).

4.2. Data and methods

4.2.1 Observations

Between days 190 and 250 (60 d total) of 2004, velocity profiles and hydrographic measurements were collected at station SH of central Oregon by moored instruments maintained by PISCO (Figure 4.1). Conditions at station YB (7 km to the north) and SH are similar (Kirincich and Barth, 2007), thus circulation appears to be locally along-shelf uniform (two-dimensional). While this study focuses on the observations at SH, data from station SR, located 27 km to the north, is used to estimate along-shelf gradients of momentum flux at SH.

At each station a bottom-mounted, upward-looking acoustic Doppler current profiler (ADCP) was deployed adjacent to a mooring of temperature and conductivity sensors. The ADCP, a RDI Workhorse 600 kHz unit, collected velocity profiles in 1 m depth increments between 2.5 m above the bottom and 1 m below the surface as well as temperature and pressure at the instrument (14.5 m depth). The nearby mooring measured temperature at 1, 4, 9, and 14 m with ONSET Tidbit or XTI loggers and temperature and conductivity at

8 m and 11 m depth using Sea-Bird 16 or 37 recorders. Wind measurements collected at NOAA's Coastal-Marine Automated Network (C-MAN) station NWP03 are used for this analysis. Station NWP03, located in Newport, Oregon on the south jetty of the harbor entrance, has been previously found to be representative of nearshore winds throughout the study area during summer (Kirincich et al., 2005; Samelson et al., 2002).

From the moored measurements, we derived hourly-averaged time series of along-shelf velocity, across-shelf surface transport, pressure anomaly, and density profiles using the steps outlined below. The hourly-averaged water velocities were rotated into an along- and across-shelf coordinate system defined by the depth-averaged, time-series mean principal axis of flow, found to be 7° (for SH) and 1° (for SR) east of true North. Time series of across-shelf surface transport were computed from extrapolated velocity profiles, assuming a constant velocity (slab) extrapolation to the surface and bottom, by subtracting the depth-averaged mean, and integrating the resulting profiles from the surface to the first zero crossing. This method is described further in Kirincich et al. (2005). An estimate of the tidal variability, found using the T_TIDE software package (Pawlowicz et al., 2002), and a mean pressure time series, calculated following Kirincich and Barth (2007), were subtracted from the pressure records to yield pressure anomaly. T_TIDE performs a classical harmonic analysis with nodal corrections for both major and 'shallow water' tidal constituents while the mean pressure time series accounts for sensor drift and shifts of the bottom lander over time. Temperature-salinity profiles from CTD casts made by PISCO at these stations revealed that a linear relationship between temperature and salinity exists in the inner-shelf during summer. The average slope of this relationship (m=8.4 ^{o}C/psu) and the 8-m salinity measurement were used to estimate salinity and density at each of the 5 temperature locations. All time series were low-pass filtered using a filter with a 40-hr cut-off frequency to isolate the sub-tidal components.

During the field season, two high resolution hydrographic and velocity surveys were

conducted from the R/V Elakha on July 14th-16th, and August 9th-11th (year days 196-198 and 223-224) along an east-west transect line terminating onshore at station SH (Figure 4.1). Water depths ranged from 15 m onshore to 70 m offshore along the 11 km transect line. Hydrographic measurements were obtained using a Sea Sciences Acrobat, a small undulating towed body, carrying a Sea-Bird 25 Sealogger CTD as payload. Velocity estimates were made with a 300-kHz RDI Workhorse Mariner ADCP mounted on the Elakha. Each day, 2-4 consecutive transects were made along the line, taking 1 hour each. Sampling was done at approximately the same phase of the tidal cycle each day. Initial processing of these ship-based observations follows the methods described by Kirincich (2003). Density and velocity fields for each transect were interpolated to a common 2D grid (offshore distance by vertical depth), averaged, and spatially smoothed to reduce noise from internal waves.

The six high-resolution hydrographic and velocity sections made on August 10th (2) and 11th (4) are used here to test the geostrophic balance at these shallow water depths. We used the thermal wind equation:

$$\frac{\partial v}{\partial z} = \frac{g}{\rho_o f}\frac{\partial \rho}{\partial x} \tag{4.1}$$

to compare the vertical shear of the along-shelf velocity (v) with the across-shelf density (ρ) gradients. In (4.1), f=1x10^{-4} is the Coriolis parameter, ρ_o=1025 kg m^{-3} is a reference density, g=9.81 m s^{-2} is the gravitational acceleration, and z is the vertical coordinate (positive upwards). The surface ($z = 0$) was used as the reference level and the ADCP derived near-surface velocity was used as the reference velocity.

4.2.2 Model formulations

The observations for station SH described above are compared with the results of two simple dynamical models used in previous inner-shelf circulation studies. Both are

based on the horizontal momentum equations, with a parameterization for the vertical turbulent diffusion of momentum:

$$\frac{\partial u}{\partial t} + u\frac{\partial u}{\partial x} + v\frac{\partial u}{\partial y} + w\frac{\partial u}{\partial z} - fv = -\frac{1}{\rho_o}\frac{\partial P}{\partial x} + \frac{\partial}{\partial z}\Big(A\frac{\partial u}{\partial z}\Big) \tag{4.2}$$

$$\frac{\partial v}{\partial t} + u\frac{\partial v}{\partial x} + v\frac{\partial v}{\partial y} + w\frac{\partial v}{\partial z} + fu = -\frac{1}{\rho_o}\frac{\partial P}{\partial y} + \frac{\partial}{\partial z}\Big(A\frac{\partial v}{\partial z}\Big) \tag{4.3}$$

where x, y, z are the across-shelf (positive onshore), along-shelf (positive northwards), and vertical (positive upwards) coordinates, u, v, w are the corresponding velocities, P is pressure, and A is the vertical eddy viscosity. The nonlinear advective terms, terms 2, 3, and 4 in (4.2) and (4.3), are included for completeness here, but ignored by the models presented next.

The first model, the analytical model of Lentz and Winant (1986), uses the spin-down time associated with bottom friction to calculate the vertically-uniform, along-shelf currents associated with a given along-shelf wind or pressure gradient. As formulated here with only wind forcing:

$$v_{lw}(t) = \int_0^t \Big\{\frac{\tau^s}{\rho_o H}\Big\} e^{\frac{-r(t-t')}{H}}\, dt' + v_o(t=0)e^{\frac{-rt}{H}}, \tag{4.4}$$

where v_{lw} and v_o are the modeled and observed depth-averaged along-shelf velocities respectively, H is the bottom depth, τ^s is the along-shelf component of wind stress, and r is a linear drag coefficient of 5x10^{-4} m s^{-1} (Lentz and Winant, 1986). Using both wind input and large-scale along-shelf pressure gradients, not included in (4.4), this model predicted along-shelf velocities well during unstratified winter-time conditions, but did poorly when stratification increased during summer (Lentz and Winant, 1986).

The second model is the 1D eddy-viscosity model originally presented by Lentz (1994, 1995). In short, it uses a control volume formulation with fully implicit time-stepping to calculate the vertical profile of horizontal velocity given a profile of vertical

eddy viscosity and surface or body forces. The model combines (4.2) and (4.3), ignoring the nonlinear terms, into a single equation for C, where $C_i^j = u + \sqrt{-1}v$ is the complex horizontal velocities at time step j and grid point i:

$$\frac{2A_i^j}{h_i(h_i+h_{i-1})}C_{i-1}^j - \Big(\frac{2A_i^j}{h_i(h_i+h_{i-1})} + \frac{2A_{i+1}^j}{h_i(h_{i+1}+h_i)} + \sqrt{-1}f + \frac{1}{\Delta t^j}\Big)C_i^j +$$

$$\frac{2A_{i+1}^j}{h_i(h_{i+1}+h_i)}C_{i+1}^j = \frac{1}{\rho_o}\Big(\frac{\partial P^j}{\partial x} + \sqrt{-1}\frac{\partial P^j}{\partial y}\Big) - \frac{C_i^{j-1}}{\Delta t^j} \tag{4.5}$$

Here, h is the control volume thickness, and $\partial P/\partial x$ and $\partial P/\partial y$ are assumed to be vertically uniform across- and along-shelf pressure gradients. Boundary conditions at the surface and bottom are:

$$A_{m+1}^j \frac{2(C_{m+1}^j - C_m^j)}{(h_m + h_{m+1})} = \frac{\tau^j}{\rho_o} \tag{4.6}$$

and

$$C_0^j = 0 \qquad \text{at} \qquad z = -H + z_{ob} \tag{4.7}$$

where τ^j is the along-shelf wind stress, m is the top control volume, and z_{ob} is a roughness length scale.

Using this model to study the weakly-stratified northern California inner shelf, Lentz (1994) found that regardless of the type of eddy viscosity profile chosen, the model with the local wind and pressure gradients reproduced the temporal variability and vertical structure of the observed along-shelf velocity well. However, across-shelf velocities differed significantly between model and observations and were highly dependent on the form of eddy viscosity used. In this study, we use both the cubic profile formulation of eddy viscosity described first by Signell et al. (1990), as well as a bilinear-cutoff profile (Deardorff, 1972; Smith and Long, 1976).

4.3. 2004 Short time-scale variability

We begin with a description of the conditions at station SH during the later half of the 2004 upwelling season (Figure 4.2) using both the moored and shipboard data. In general, the study area was forced by upwelling favorable winds (wind stress of -0.05 N m^{-2}) that resulted in southward velocities near 0.1 m s^{-1} and dense waters (σ_t=25.5-26 kg m^{-3}) in the inner shelf. Periodic wind reversals occurring near days 203, 220-224, and 236-242 (Figure 4.2) caused reversals of along-shelf velocity and reduced inner-shelf density. Water-column temperatures range from 8-9°C during strong or sustained upwelling, and 14-16°C during these current reversals. This hydrographic variability indicates that conditions regularly transition between fully upwelled (when the upwelling front intersects the surface offshore of the mooring, leaving weakly stratified conditions inshore) and fully downwelled (similar conditions but for a downwelling front) in response to the local wind forcing. Waters tend to be more stratified during periods of weaker winds (e.g. days 195-202 and 227-232), weakly stratified during upwelling conditions (e.g. days 206-215 and 224-227), and nearly unstratified during peak downwelling events (e.g. days 219 and 238-241) (Figure 4.2). Overall, wind fluctuations occur often and rapidly.

The hydrographic effects of these rapid fluctuations are further illustrated using the across-shelf sections obtained on August 10th and 11th (year days 223 and 224) shown in Figure 4.3. During this period, winds transition from a short downwelling event (day 222) to strengthening (day 223) and then sustained (day 224) upwelling (Figure 4.2a). The across-shelf hydrographic sections (Figure 4.3a) show isopyncals transitioning from nearly horizontal on day 223 (dashed lines) to strongly upwelled on day 224 (solid lines). Comparing the relative location of individual isopyncals during this transition, assuming along-shelf uniformity, indicates the rapid pace of water mass transitions present in the inner shelf. The σ_t=25 kg m^{-3} isopycnal lies at 10 m depth inshore of the 15 m isobath

(1.5 km offshore) on day 223, but intersects the surface near the 50 m isobath 6.5 km offshore one day later. A water parcel at this interface would need an average across-shelf velocity of 0.06 m s^{-1} to attain this displacement. Additionally, comparing the ship-based hydrography and velocity surveys using the thermal wind equation (4.1) shows that the across-shelf density structure is nearly geostrophically balanced by along-shelf velocities on day 224 (Figure 4.3b,c). Density derived geostrophic velocities have similar vertical shear and, using the ADCP near-surface velocities as a reference value due to the sloping bottom, similar magnitude and directions as the ship-based velocity throughout the inner-shelf. An rms difference between the two sections is 0.037 m s^{-1} overall, but 0.025 m s^{-1} within the area of the upwelled isopycnals. This comparison illustrates that the along-shelf upwelling circulation can be nearly geostrophically balanced in the inner-shelf at water depths as shallow as 15 m along the Oregon coast.

The time series of measured across-shelf surface transport at SH was correlated with the theoretical Ekman transport for the same period (0.73 at zero lag), but was lower in magnitude (Figure 4.4a). Following the method of (Kirincich et al., 2005), the fraction of full Ekman transport present over the 60 d study period was 24%. This fraction was near the average for this station, based on 5 years of seasonal data. However, comparing the measured surface and theoretical Ekman transports at station SH (Figure 4.4a) over time-scales similar to the 2-7 d wind and stratification events, yields statistically insignificant results. Over these shorter time intervals, there are too few independent degrees of freedom to attain statistical significance between the theoretical and measured transport.

Given the small volume of water inshore of 15 m water depth, it is likely that this wind-forced across-shelf transport is able to move water masses into and out of the inner-shelf on time scales similar to the fluctuating winds. Assuming a simple mass conservation balance between local density changes and the advection of an across-shelf density gradient by the across-shelf circulation, these movements are illustrated by comparing the

measured surface transport to the time rate-of-change of density at the 11 m CT (Figure 4.4b). Episodes of strong offshore (negative) transport occur with positive density changes (e.g. days 203, 220, and 224), evidence of denser waters moving onshore during active upwelling. The opposite was true during transitions to downwelling events, with onshore (positive) surface transport occurring with negative density changes, indicating lighter waters entering the inner-shelf. Stratification (shaded in Figure 4.4b) was most variable during these transitions. Yet, across-shelf transport, density, and stratification did not always vary together. Instances existed where both surface transport and density changes were large but stratification was small (days 238-240), and where surface transport was large but both density changes and stratification were small (e.g. days 207-212, 232-233 in Figure 4.4b). These findings appear to disagree with the relationship between stratification and transport described in the introduction (Austin and Lentz, 2002; Tilburg, 2003; Kirincich et al., 2005). Testing this further, we computed the Ekman transport fraction for varying levels of stratification. Separating the time series of theoretical and measured transport by the level of stratification, and computing the transport fraction, leads to statistically significant results for most bins (Figure 4.5). The resulting mean Ekman transport fraction is similar for all levels of stratification and thus no real trend exists that supports the weak relationship between transport fraction and stratification seen in Kirincich et al. (2005).

Despite the complex dynamics occurring at SH, much of the variability of the depth-averaged along-shelf velocity can be explained by the simple analytical and numerical models introduced earlier. As Figure 4.4c shows, time series of the depth-averaged along-shelf measured V_o, V_{lw} following Lentz and Winant (1986), and V_{cub} following (Lentz, 1994) velocities are similar and correlated (V_o/V_{lw}: 0.81 at zero lag, V_o/V_{cub}: 0.79 at zero lag). However, in agreement with Lentz (1994), the numerical model has difficulty representing the across-shelf circulations described above (not shown here). Further, there

are specific times when even the along-shelf velocities differ significantly. Many of these time periods (days 205-206, 215-220, 226-229, and 233-234) occur when stratification is high or rapidly changing (Figure 4.4c). As with previous studies, these models tend to accurately represent the largest sources of variability when waters are unstratified or weakly stratified. Additional times of poor agreement (days 203-204, 206-214) indicate that secondary forcings (e.g. pressure gradients) may exist in addition to the dominant wind forcing.

Thus with the varying conditions seen at station SH, neither simple models nor metrics derived from the observations were able to accurately represent the variability of the vertical turbulent diffusion of horizontal momentum, the ultimate controller of across-shelf dynamics. More robust models have been used to answer these questions (Austin and Lentz, 2002; Kuebel Cervantes et al., 2003) with some success, but their explanations of observations hinge on correctly forcing the model. Observational assessments of the full, depth-dependent momentum equations in the inner-shelf are also lacking, especially in regions where large-scale oceanic forcings dominate shelf-wide dynamics such as the Oregon coast. In the remainder of this paper we attempt to understand the time variability of across-shelf inner-shelf dynamics with a different approach. We use the observations available at station SH along with the Lentz (1994) 1D model formulation described above to estimate the time-dependent eddy viscosity and thus the vertical diffusion of horizontal velocity at this location. Estimates of these terms should allow us to link the variability seen in the measurements to its true dynamic controller as well as point to important momentum terms that are neglected in the 1D model.

4.4. Inverse methods

In the Lentz (1994) linearized 1D circulation model described above, velocity profiles are estimated given the wind or pressure forcing and an assumed vertical profile of eddy viscosity. Here we seek an inverse solution to (4.2) and (4.3) that estimates the eddy viscosity profile given observations of the vertical profiles of horizontal velocities and wind forcing. Reordering the linear, fully-implicit, control-volume model (4.5) to solve for eddy viscosity (A) gives:

$$-\frac{2(C_i^j - C_{i-1}^j)}{(h_i + h_{i-1})}A_i^j + \frac{2(C_{i+1}^j - C_i^j)}{(h_{i+1} + h_i)}A_{i+1}^j = \sqrt{-1}fC_i^j h_i + \frac{h_i}{\rho_o}\Big(\frac{\partial P^j}{\partial x} + \sqrt{-1}\frac{\partial P^j}{\partial y}\Big) + \frac{(C_i^j - C_i^{j-1})}{\Delta t^j}h_i, \tag{4.8}$$

a first-order ODE requiring knowledge of the horizontal pressure gradients ($\partial P/\partial x$ and $\partial P/\partial y$), the horizontal velocities, and one boundary condition. We use the surface (wind) forcing to obtain the eddy-viscosity at the surface:

$$A_m^j \frac{2(C_{m+1}^j - C_m^j)}{(h_{m+1} + h_m)} = \frac{\tau^j}{\rho_o}, \tag{4.9}$$

where τ^j is the along-shelf wind stress and m is the top control volume.

Of these three inputs to the inverse solution, the depth-dependent horizontal pressure gradients are perhaps the least significant, yet the most difficult to measure, or calculate, directly. In Kirincich and Barth (2007), an estimate of the across-shelf surface pressure gradient, based on measurements of bottom pressure at the PISCO stations and an assumed across-shelf length-scale of upwelling, was in nearly geostrophic balance with the depth-averaged, along-shelf velocities throughout the upwelling season. Additionally, the shipboard results reported in Figure 4.3 show that a thermal wind balance between the vertical shear of the horizontal velocity and the across-shelf density, or internal pressure, gradient is possible at these inner-shelf locations, especially during upwelling favorable

winds. Based on the above evidence, these 'geostrophic' contributions to the total, depth-dependent pressure gradients should be large, particularly in the across-shelf direction. However, these measurements were not made at the PISCO stations with sufficient accuracy and thus must be estimated as part of the inverse solution. For this reason, we divide the unknown pressure gradients into two parts, one in geostrophic balance with the Coriolis momentum term, and one not. The first is assumed to be fully balanced by the Coriolis term, thus removing the depth-dependent geostrophic balance from the inverse calculation. The second, non-geostrophic component of the total pressure gradients is assumed to be vertically uniform to simplify the inverse calculation, as has been done previously (Lentz and Winant, 1986; Lentz, 1994).

With this partition, we seek the vertical profile of eddy viscosity from (4.8), but now must include vertically-uniform, non-geostrophic pressure gradients into the solution. Moreover, if the given velocity profiles are not fully explained by the input forcing and these pressure gradients, had they been known, the resulting eddy viscosity profile will be incorrect, and possibly include an imaginary part. This imaginary part can be understood dynamically considering the balance of momentum. A residual momentum term will exist if the vertical diffusion term, with its magnitude and vertical structure driven by the unknown eddy viscosity as well as the vertical derivatives of horizontal velocity, is unable to account for all of the remaining momentum. In the inverse solution, this residual term, denoted $\mathbf{R}$ as it has a component in both (4.2) and (4.3), is packaged into an imaginary part of the calculated eddy viscosity. To proceed forward, we assume that the bulk of this incorrect or additional momentum is due to the unknown, vertically-uniform, non-geostrophic, along- and across-shelf pressure gradients. We then assign this excess momentum to the pressure gradients, while at the same time forcing the structure of A to be as physically realistic as possible, using a matching technique. This technique finds the pressure gradients that make the profile of A as positive as possible (as vertical diffusion

is a momentum sink ($A > 0$) not a source ($A < 0$)) and minimize the depth-averaged absolute value of the residual momentum terms ($\mathbf{R}$). An example of this pressure-matching technique and a discussion of the accuracy and sensitivity of the inverse solution is given in the Appendix.

With this method, we solve the inverse equation in its linear form using only the velocity profiles and wind stress as input. The raw, hourly velocity profiles used in the calculation were first normalized by water depth and interpolated into a regularly spaced vertical grid. Both velocities and wind stress were low-pass filtering in time before use in the inverse calculation, isolating the sub-tidal components. The results of the inverse calculation consist of time series of matched along- and across-shelf pressure gradients, an eddy viscosity (A), and depth-dependent residual momentum terms ($\mathbf{R}$). The matched pressure gradients are assumed to be composed of the true, non-geostrophic, vertically uniform pressure gradient and the depth-averaged mean of any other unrepresented terms in the momentum equations (e.g. non-linear advection), while the residual momentum term accounts for the depth-dependent part of an unrepresented term.

The method described here is not a true inverse estimate of vertical diffusion and eddy viscosity given the available velocity and wind stress observations, if only because we assume the measurements are error free. Certainly a variational estimation technique, similar to that of Yu and O'Brien (1991) or Panchang and Richardson (1993), could be expanded to include the additional unknowns of the pressure gradients, the time-dependence of A, while more strictly governing the form of the resulting eddy viscosity. Additionally, a formal inverse ocean model, assimilating the velocity profiles, might give dynamically consistent estimates for eddy viscosity. However, the technical aspects of both methods are beyond the scope of this work. We proceed with the basic model described above to understand how variations in vertical eddy viscosity over the time scales of wind and pressure forcing events can effect, or control, across-shelf circulation in the inner-shelf.

Based on the accuracy and sensitivity of the method, inferred from additional tests and described in the Appendix, the inverse calculation formulated here is deemed adequate for this purpose.

4.5. Inverse results

The inverse calculation for the station SH data produces time series of eddy viscosity through the measured portion of the water column (Figure 4.6). In general, the calculated values of A were similar to, or lower than, estimates from inner-shelf numerical modeling studies given in the literature (see discussion). The estimated eddy viscosity had a strong variability (greater than two orders of magnitude) superimposed on a mean value of $1.3\text{x}10^{-3}$ m^2 s^{-1}. Times of peak A values (> 0.01 m^2 s^{-1}) occur at times of strong surface forcing and rapidly changing stratification (near days 222 and 238, Figure 4.6). At these times A was a maximum near the surface, or more precisely, at the top of the measured part of the water column. Additional elevated times occurred when A is a maximum near the bottom. These occasions were associated with the periods of strong positive matched vertically uniform along-shelf pressure gradients (Figures 4.7 and 4.8), and positive wind stress (Figure 4.6).

The difference between upwelling and downwelling dynamics in the inner shelf is striking and best shown by the depth-averaged eddy viscosity. The depth-averaged A during upwelling ranges from the lowest values, $1\text{x}10^{-4}$ m^2 s^{-1}, to 2 to $3\text{x}10^{-3}$ m^2 s^{-1}. The time series mean value during upwelling favorable winds is $8\text{x}10^{-4}$ m^2 s^{-1}. In contrast eddy viscosities are significantly larger during downwelling favorable conditions, with peak values reaching up to 7 to $9\text{x}10^{-3}$ m^2 s^{-1}. The time series mean during downwelling was $2.1\text{x}10^{-3}$ m^2 s^{-1}.

Accuracy testing for the inverse solution was done using the output of several nu-

merical models and is described in detail in the Appendix. Briefly, the results of these tests indicate that the inverse calculation is unable to reasonably estimate eddy viscosity when the vertical shear of the horizontal velocity is less than 5x10^{-3} s^{-1}. Approximately 4.4% of the values from the station SH ADCP record fell below this threshold. Additionally, the inverse did poorly when the true eddy viscosities were less than 5x10^{-5} m^2 s^{-1}. Approximately 4.2% of the estimated eddy viscosity values at station SH fell below this threshold. Above these levels, the comparive tests infer that rms errors are 20% of the mean eddy viscosity values for upwelling and downwelling if the inverse solution is well-formulated. If additional sources or sinks of momentum have been neglected, potential errors increase to 40-60% of the mean upwelling or downwelling values throughout most of the water column, but approach the mean values themselves in the bottom 2-3 m.

A second, independent assessment of the quality of the inverse result comes from a comparison of the resulting depth-averaged, along-shelf, vertical diffusion term with its theoretical equivalent, the sum of the along-shelf wind stress and bottom stresses:

$$\frac{1}{H}\int_{-H}^{0}\frac{\partial}{\partial z}\Big(A\frac{\partial v}{\partial z}\Big)dz \sim \frac{(\tau_y^s - \tau_y^b)}{\rho_o H}. \tag{4.10}$$

Here, H is the water depth integrated over, and τ_y^b is a quadratic bottom stress, calculated using the lowest velocity bin of the ADCP (2.7 m above the bottom) and a drag coefficient of 1.6x10^{-3} following Perlin et al. (2005). In general, the two time series were quite similar (Figure 4.6e) and positively correlated (0.65). They are most similar during upwelling favorable winds (upwelling correlation 0.88), where the values shown in Figure 4.6e are normally positive. The time series differ only when the estimated term was negative (Figure 4.6e), generally coinciding with downwelling wind events, and/or times of positive matched along-shelf pressure gradients (Figure 4.8). These specific discrepancies occur as this comparison is not entirely appropriate during downwelling conditions. During these times, flow conditions are known to be more barotropic, and thus the majority of the

vertical diffusion of turbulent momentum occurs closer to the bottom. As the measured area encompasses only 70% of the water column and excludes the bottom 2 m, this location of significant stress will be missed. An additional inverse calculation, run with velocity profiles that were arbitrarily extrapolated to the surface (as a constant velocity slab) and bottom (as a linear interpolation to zero at the bottom) has much better agreement during downwelling conditions (Table 4.1).

From these comparisons, the inverse calculation appears to represent eddy viscosity sufficiently well, particularly during upwelling favorable winds. The discrepancies that exist during some of the downwelling or weak wind events were also times when the wind-driven models shown earlier did poorly. While these periods appear to be pressure forced, as the matched along-shelf, non-geostrophic pressure gradient is large and positive here (days 204, 215-219, and 238 in Figure 4.8), a portion of the pressure gradients might also account for a mis-match between the forcing and the resulting velocity profiles, a biased estimate of the mean vertical mixing term, or a significant depth-independent non-linear terms.

The distribution of momentum in the inverse model results can be packaged into four terms for each horizontal momentum equation: the measured acceleration, the vertically uniform, non-geostrophic pressure gradient, the vertical diffusion of momentum, and the residual momentum terms. Analysis of these terms in the across and along-shelf momentum balances (Figures 4.7a-d and 4.8a-d) give an idea of what are the dominant momentum balances in addition to the geostrophic balance already removed, how important is the vertical diffusion term, and what are the possible sources of the additional momentum packaged into the residual and pressure terms. Estimates of the across-shelf and vertical advective terms, terms 2 and 4 in (4.2) and (4.3), are given here (Figures 4.7e-f and 4.8e-f) for comparison with the residual term. We estimated these terms from the available PISCO observations and assumptions about their structure. The across-shelf

advection terms use station SH velocities and an across-shelf velocity gradient between the measurements at SH and zero at the coastal boundary. The vertical advective terms were computed by multiplying the vertical gradients of station SH horizontal velocities with an estimate of the vertical velocity. We assume the across-shelf surface transport at station SH, divided by the distance to the outside of the surf zone (700 m), is representative of the maximum, mid-depth vertical velocity (w) and assume a parabolic vertical structure for w. In both equations, the along-shelf momentum flux, term 3 in (4.2) and (4.3), was an order of magnitude smaller than all other terms and thus not included further. It should be noted that all terms are shown (Figures 4.7 and 4.8) as if they were on the left side of the momentum equations (4.2,4.3). Thus while we look for the opposite structure (or colors) for balances among the top four panels, we look for similar structure when comparing the residual term (panels d) to the advective estimates (panels e and f).

In the across-shelf balance, acceleration and the non-geostrophic pressure gradient are small compared to vertical diffusion and the residual term (**R**). Of the advective terms, across-shelf advection is weak throughout but occasionally appears to match **R** (days 204, 221, and 224 in Figure 4.7). Vertical advection is the larger of the two non-linear terms included, and visually matches the sign and vertical structure of **R** more often (days 204, 207-212, 220, 224, 232-245), but is slightly reduced in magnitude.

In the along-shelf balance, the non-geostrophic pressure gradient is often large and frequently balances the bulk of the vertical diffusion term (Figure 4.8). Acceleration is somewhat important during times of rapidly transitioning or strong wind forcing. During upwelling wind periods (e.g. days 207-214, 224-227, 231-234, and 241-252), the vertical structure of **R** was similar to the estimated along-shelf advective term, inferring that much of the residual was due to the exclusion of this non-linear term from the calculation. The estimated vertical advective term was also frequently large. During these same upwelling periods, it was negative, mostly vertically uniform, and thus similar to

the matched non-geostrophic along-shelf pressure gradient. The same is not true during downwelling conditions (e.g. day 238). Here, neither advective term appears to account for the residual momentum.

Spikes or sharp sign changes in vertical diffusion occur in both momentum equations and generally coincide with opposing patterns in the residual momentum terms. These patterns occur most frequently during times of rapid transitions between upwelling and downwelling (days 198, 200, 206, 227, 246) and appear to indicate the effects of measurement or calculation errors. These suspect areas of vertical diffusion and residual momentum are the largest magnitude features for each term. Yet, despite their presence, the comparisons given above suggest the importance of both the across-shelf and vertical advection terms in the momentum balances, especially during upwelling. In the along-shelf balance, across-shelf advection was similar in vertical structure to **R** during these times. While admittedly speculative, the estimated vertical advection also appeared to be an important term in both balances, frequently resembling the residual in the across-shelf balance or the vertically-uniform pressure gradient in the along-shelf balance. Thus the full momentum balance comparisons give further support to the estimated vertical diffusion and eddy viscosity from the inverse calculation.

4.6. Eddy viscosity and across-shelf transport

The inverse model results, despite the possible errors illustrated above, gives an estimate of the magnitude and vertical structure of eddy viscosity at this inner-shelf location. Below we examine the time-dependence of the estimated eddy viscosity (A), its effect on circulation, and relate its vertical structure to the conditions present.

A reanalysis of the binned Ekman fraction calculation using depth-averaged A, instead of stratification, gives drastically different results. Here, the fraction of full Ekman

transport clearly decreases as the magnitude of A increases (Figure 4.9). Of the significant (shaded) results, Ekman transport ranged from 70% for A centered at 0.4x10^{-3} m^2 s^{-1} to 15% centered at 3.6x10^{-3} m^2 s^{-1}. However, the majority of the deployed hours fell in the band between fractions of 40% and 30% and A=0.8 to 1.7 x10^{-3} m^2 s^{-1}. The median fraction given here is 10% higher than the time series mean fraction given above. The distribution of these fractions during the 8 d period starting on year day 218 illustrates how the fraction of full Ekman transport varies with forcing events. The lowest fractions occurred during the peak downwelling event of day 219 (Figure 4.10), while the highest fractions occurred at times of weaker wind forcing or, more importantly, transitioning forcing (days 218, 222.3, and 223). This variability can also be thought of as more (high fraction) or less (low fraction) of the Ekman spiral fitting into the water column as conditions vary in time. The progression of high fractions to low fractions and back to high over the course of a wind event is illustrated by the upwelling events present in this time period (Figure 4.10). This is of particular importance as in the initial or final stages of a wind event, presumably as the water column becomes more stratified, the fractional transport can be large. It is during these times that the total exchange of the inner-shelf water masses is likely to occur.

In general downwelling events tend to have lower fractions (weaker across-shelf transport relative to wind forcing) than upwelling events. This discrepancy has important implications for across-shelf transport in the inner-shelf. As illustrated in the lower part of Figure 4.10, the across-shelf transport accumulated over the 8 d period attains a more negative value than the theoretical transport reduced by the station mean transport fraction. This difference is due to the reduced transport during the first downwelling event as well as increased transport during transitions between events. As a result, twice as much water has been upwelled through the region inshore of the mooring by the end of the period than that predicted.

To analyze the vertical structure of A, we performed an Empirical Orthogonal Function (EOF) analysis of A after removing the depth-averaged mean and normalizing by standard deviation for each vertical profile. This calculation resulted in normal modes, similar to an EOF of the velocity field. Of the results, modes one and two account for 50 and 25% of the total variance, while modes three and four account for 10% and 4%. The vertical structure of eddy viscosity at station SH is well represented by a composite of the first three modes. Examples of this composite at times of positive and negative modal amplitudes for both modes one and two are quite similar to A (Figure 4.11c,d). Sample profiles during mode-one dominated conditions are linear and surface intensified during times of strong wind forcing (e.g. year day 237.2 in Figure 4.11c) but bottom intensified when the matched along-shelf pressure gradient is stronger (e.g. year day 253). Mode two dominated profiles can be either boundary (e.g. day 204) or mid-water (e.g. day 216.1) intensified, corresponding to transitioning or similar forcing conditions (Figure 4.11d).

Focusing on times when modes one or two are clearly dominant (explaining >60% of the hourly variance), mode one is positive (surface intensified A, darker shading in Figure 4.11a) when wind forcing is strong (e.g. days 223, 232-234, and 238). Mode one tends to be dominant and negative (bottom intensified A, light shading) less often than it is dominant and positive. These negative instances occur when the matched pressure forcing is stronger and/or different than the wind (e.g. days 194, 211, and 228). Mode two is negative (both surface and bottom intensified, light shading in Figure 4.11b) during weak wind periods or transitions between upwelling and downwelling events (e.g. days 215-218, 235, 246-249). Mode two is rarely dominant and positive, a mid-water intensified profile similar in form to the 'cubic' A profiles used here and by Lentz (1994) in the 1D eddy viscosity models.

4.7. Discussion and Conclusions

This analysis has described the short time-scale (2-7 day) variability of forcing, circulation, and hydrography along the central Oregon coast. We have also used a one-dimensional numerical model to estimate the vertical eddy viscosity, a parameterization of the transfer of momentum due to turbulent eddies, present in the inner-shelf using typically collected in-situ observations. Conditions in the study area, sheltered from the regional circulation by the offshore submarine bank, were highly variable in time. Due to wind-forced variations, rapid transitions occurred between upwelling and downwelling circulation, causing variable residence times and a variety of water masses to be observed in the inner-shelf. The relationship between full theoretical Ekman transport and the measured surface transport, the fraction of full Ekman transport, is a metric of the efficiency of across-shelf exchange in the inner-shelf. Variations in this metric do not correspond to changes in wind forcing or stratification alone, as has been previously suggested (Tilburg, 2003; Austin and Lentz, 2002; Kirincich et al., 2005), but were instead linked to variations in estimates of vertical eddy viscosity. Instances where eddy viscosity was small allowed for the full flushing of the inner-shelf, even during weak wind stresses. When eddy viscosity was high, across-shelf transport was reduced and residence times increased.

The varying magnitudes of eddy viscosity during upwelling and downwelling seen here have been noted in previous modeling results. Forcing an inner-shelf model with constant winds of 0.1 N m^{-2} and constant stratification, Austin and Lentz (2002) found vertical eddy viscosities with cubic vertical structure and maximum values of 1x10^{-2} m^{-2} s^{-1} during downwelling and 7x10^{-3} m^{-2} s^{-1} during upwelling in similar water depths. With variable forcing conditions, the Kuebel Cervantes et al. (2003) modeling results, also used as a test case in the Appendix, had much lower mean values of 9x10^{-4} m^{-2} s^{-1} during upwelling mean and 3.9x10^{-3} m^{-2} s^{-1} during downwelling. These lower values are

similar to the estimated eddy viscosities for the station SH data reported earlier.

The inverse results have pointed to important missing sources of momentum in the inner-shelf along- and across-shelf momentum equations. While a barotropic geostrophic balance dominates the across-shelf momentum balance, also observed in Lentz et al. (1999), our observations and inverse solution also confirmed the importance of the thermal wind balance at these shallow depths in accounting for the geostrophically-balanced vertical shear of the horizontal velocities. Two of the nonlinear advective terms estimated, along-shelf and vertical advection, appeared to be important in the momentum balances. The importance of the across-shelf advective terms during active upwelling was also seen in the Kuebel Cervantes et al. (2003) inner-shelf model and proposed by Lentz and Chapman (2004) to be an important momentum term during upwelling across the shelf. While similarities between our estimates of these terms and the residual from the inverse calculation existed (Figures 4.7 and 4.8), inclusion of these estimates into the inverse formulation did not significantly alter estimates of A or reduce $\mathbf{R}$ (Table 4.1). Based on this discrepancy, better estimates of these terms, especially vertical advection, are necessary if future studies are to fully understand the time variability of this system.

The results presented here illustrate that northward, downwelling favorable, wind bursts lead to high eddy viscosities and low amounts of across-shelf transport. Thus the net across-shelf circulation can be biased toward the upwelling of colder, nutrient rich waters into the inner shelf during periods of fluctuating wind forcing. This is a notable result, and has significant implications for the common use of large-scale, wind-based upwelling indices to estimate upwelling transports along coastal locations. Although the total magnitude of upwelled waters, integrated across the shelf, is accurately predicted with such indices, the amount of upwelled waters seen at a particular across-shelf location in the inner-shelf may vary greatly from the index. In particular, indices will underestimate the net water upwelled inshore of water depths similar to those studied here during periods

of variable wind forcing.

Our study has identified episodes of total water mass exchange, the sequestering of water masses in the extreme inner shelf, and the progression of transport efficiency during wind events. These effects may have significant implications for inner-shelf ecological communities. Previous ecological studies in upwelling environments show that increased settlement of larval invertebrates was correlated with episodes of increasing water temperatures (Miller and Emlet, 1997; Farrell et al., 1991; Broitman et al., 2005). Along the Oregon coast, the transition from upwelling to downwelling, with its decreased eddy viscosity and increased across-shelf transport efficiency, allows for a full flushing of the inner-shelf and replacement with warm, fresh surface water. Once this transition has occurred, eddy viscosity increases and across-shelf circulation is reduced or 'shutdown'. This process provides a mechanism for focused, successful across-shelf transport or retention of propagules. Whether this aids recruitment depends on the life cycle characteristics of the individual species. Larvae released during such an event would tend to say closer to shore for a longer period of time than if released during normal upwelling conditions. Additionally, with an overall bias toward onshore transport at depth during upwelling, larvae able to adjust their buoyancy would be able to move onshore in a predicable manner.

The inverse method used here may be useful in future dynamical studies of shallow water locations where the velocity profiles are well resolved. As seen in the sensitivity testing, complete water column profiles could further improve this type of analysis, especially filling the area near the bottom. As stated earlier, previous efforts to estimate eddy viscosity from measurements exist (Yu and O'Brien, 1991). However, to our knowledge, none have allowed additional unknown terms (e.g. pressure gradients or nonlinear advection) to appear in the solution. In future work, we hope to add variational estimate techniques that allow for measurement errors and exert greater control over the resulting form of the eddy viscosity profiles.

4.8. Appendix: Inverse method details, accuracy, and sensitivity.

An example of the matching process used to attain estimates for eddy viscosity as well as the vertically-uniform pressure gradients and the residual momentum term is shown graphically in Figure 4.12. To compute the inverse calculation, (4.8) is solved numerically as a matrix inversion of the vertical profile of eddy viscosity A, given the velocity profiles, surface forcing, and a matrix of assumed pressure gradients. The effects of the different assumed pressure gradients on the amount of positive values of A and the depth-averaged mean of the absolute residual are compared as in Figure 4.12. The pair with the highest combined rating, maximizing the number of positive A values while minimizing the depth averaged mean of the absolute residual, is chosen as the 'matched' pressure gradients. This process is done independently for each time step j, computing estimates for eddy viscosity profiles for the deployment period at station SH.

4.8.1 Accuracy

The inverse method described in the text was tested using model output from both the unstratified Lentz (1994) 1D eddy viscosity model and the stratified 2D model output of Kuebel Cervantes et al. (2003). Estimating the eddy viscosity of these forward model outputs, where the 'true' eddy viscosity is known, allows an assessment of the accuracy of the inverse calculation and an understanding of when and how the calculation fails. Model output from the unstratified 1D model was used to test the effects of low-resolution velocity profiles and the pressure matching technique in the inverse method. The full inverse method, including partitioning of the pressure gradients into geostrophically balanced and vertically-uniform, non-geostrophic components, was tested with the stratified 2D forward model output of Kuebel Cervantes et al. (2003). Model output of eddy viscosity, horizontal velocity, and wind forcing from 15 m water depth were extracted from the July-August 60 d model run, spanning the variable forcing and hydrographic conditions

described by Kuebel Cervantes et al. (2003). As these test models vary in formulation, length, wind forcing, and resulting eddy viscosities and vertical shears, separate error estimates are given for each model.

Based on testing with the 1D model, the inverse calculation for eddy viscosity is unreliable for levels of total vertical shear of the horizontal velocity less than 0.005 s^{-1} due to rounding errors in the bin averaging process. An inverse of a fully resolved 1D forward model output retrieves the exact values of A, while an inverse of the model output, bin-averaged to match the 1 m vertical resolution of the ADCP, has a larger rms that is driven primarily by shears less than 0.005 s^{-1}. Excluding estimates of eddy viscosity at times/depths having shears less than 0.005 s^{-1} leaves a rms error of 0.004 m^2 s^{-1}, or <20% of the mean eddy viscosity and is independent of depth or wind forcing conditions (Figure 4.13). The pressure matching component of the inverse adds no additional rms error to the estimate of A for this model.

Inverse estimates of eddy viscosity for the Kuebel Cervantes et al. (2003) model output show the different responses for downwelling and upwelling conditions. For depths/times where the vertical shear of horizontal velocity is greater than the 0.005 s^{-1} threshold used above, rms differences during upwelling favorable conditions increased with depth from $0.4x10^{-3}$ to $1x10^{-3}$ m^2 s^{-1}, or 40-70% of the mean upwelling eddy viscosity $9x10^{-4}$ m^2 s^{-1}, throughout most of the water column. However, potential error increases in the bottom 2 m to more than twice the mean upwelling value. Despite these variations, the mean eddy viscosity profile is well predicted by the inverse calculation during upwelling conditions (Figure 4.13). For values above a shear threshold of 0.01 s^{-1}, upwelling normalized rms error decreased to 40-50% throughout most of the water column, and 50% in the bottom 2 m. RMS differences are larger during downwelling conditions, increasing with depth from $0.5x10^{-3}$ to $2.5x10^{-3}$ m^2 s^{-1} at 11 m depth, or 10% to 60% of the downwelling mean of $3.9x10^{-4}$ m^2 s^{-1}. As a result, the rms difference window about the

mean profile is much larger during downwelling verse upwelling (Figure 4.13). However this is somewhat misleading as the inverse solution for eddy viscosity systematically underestimates the large eddy viscosities seen in the Kuebel Cervantes et al. (2003) model during downwelling conditions, possibly as a result of the assumptions used to partition the pressure gradients. The subtraction of a geostrophic balance, assuming the sheared Coriolis term is fully balanced by a baroclinic pressure gradient, might be incorrect during strong downwelling events and bias the eddy viscosity to lower values. Additional inverse solutions of the Kuebel Cervantes et al. (2003) model, without the pressure partioning, led to reduced rms differences during downwelling. Regardless, the measured and theoretical depth-averaged vertical diffusion terms of the full inverse solution for this model output were positively correlated (0.75 at zero lag), and agree favorably during both upwelling and downwelling.

For both test cases, the estimated eddy viscosities captured both the temporal variability and vertical structure of model output or 'given' eddy viscosities. The major difference between the test model accuracies appears related to the relative distributions of velocity shear and the presence of additional momentum sources neglected in the inverse method. These tests infer that the inverse method is more accurate closer to the surface and at higher values of vertical shear of the horizontal velocity. An increase in error with distance away from the boundary condition is a common issue with numerical solutions to first-order differential equations (Chapra and Canale, 1988). Increasing error with decreasing vertical shear occurs as computational errors become more important at these lower values. In the station SH velocity data, the vertical shear of the horizontal velocity rarely falls below 0.005 s^{-1} (<4% of the observations), and is generally above 0.01 s^{-1} (>85%). In contrast, the distribution of velocity shear for the Kuebel Cervantes et al. (2003) model is strongly skewed towards values less than 0.01^{-1}. Because of this fact, we believe the normalized rms differences for values above a shear threshold of 0.01 s−1,

affecting primarily the upwelling results, may be more representative of the accuracy of the inverse solution for the ADCP measurements described in the text.

4.8.2 Sensitivity

Tests of the sensitivity of the inverse method to variations in the input parameters and calculation methods are described here. We compared these tests by examining the estimated eddy viscosity, the similarities between the estimated and theoretical depth-averaged vertical diffusion (as shown for the *base case* in Figure 4.6e), the magnitudes of the residual momentum terms, and the change in the binned Ekman fraction calculation (Figure 4.9). These tests are summarized here and in Table 4.1.

The *base case* method included removing the geostrophic balance from the equation by partitioning both pressure gradients into two components and using a pressure gradient 'grid' resolution of $5\text{x}10^{-4}$ N m^{-3} for the matching procedure. Variations to the *base case*, described both here and in the text, were made to assess the relative importance of the inverse formulation. The importance of the pressure gradient resolution was tested by decreasing the resolution to $1\text{x}10^{-3}$ N m^{-3} (*course grid*) and increasing the resolution to $2.5\text{x}10^{-4}$ N m^{-3} (*fine grid*). The effect of removing the geostrophic balance from the model was tested by including the Coriolis terms and assuming the total pressure gradients were vertically-uniform (*geo*). The form of the velocity profiles used in the inverse calculation was tested by using un-filtered velocity profiles and wind stresses, thus including tidal and diurnal variability, and secondly by extrapolating the profiles to the surface (assuming a constant velocity slab) and the bottom (assuming a linear interpolation to zero at the bottom). This was done for runs with the geostrophic balance removed (*extrap* and *tidal*) and for runs that included the geostrophic balance (*geo extrap* and *geo tidal*). The possible effects of the neglected nonlinear advective terms were tested by including all three terms in the calculation (*NLT*) or just the along and across-shelf advection terms (*hor. NLT*). The effects of the pressure gradient partitioning were tested by assuming: the across-

shelf pressure gradient was entirely geostrophically balanced and thus only the along-shelf pressure gradient was allowed to have a non-geostrophic component ($dP/dx=0$), and by assuming the along-shelf pressure gradient was only vertically uniform and not able to be partitioned (*ASgeo*). Finally, the sensitivity of the inverse to variations in surface forcing was tested by using along-shelf winds from a nearby offshore buoy (NDBC 46050, *buoy winds*) and reduced wind stress (*reduced winds*) on the assumption that some fraction of the input wind energy might be expended in the top 1 m of the water column not included in the calculation.

As seen in Table 4.1 and Figure 4.13, many of the these alterations to the input time series or calculation methods did not significantly change or improve the estimated eddy viscosity results or the correlations between the theoretical and measured depth-averaged vertical diffusion. Notable exceptions are described here. The tests with the geostrophic terms included (*geo*) had an increased downwelling correlation and a larger percent positive for A. However, *geo* tends to over over-estimate A especially in the lower part of the water column during upwelling to account for the geostrophically-balanced vertical shear present, hence the larger values of A in Table 4.1 and runs with larger near-bottom A in Figure 4.13. Because of this geostrophic shear, *base case* appears more dynamically correct during these times. Tests including tidal and diurnal variability (*tidal, geo tidal*) have estimated values for A that are qualitatively similar to the base case, the metrics for both were quantitatively worse (Table 4.1). It is these tests that result in large A in the lower part of the water column during downwelling conditions (Figure 4.13). Although the analysis given above identifies the advective terms as the main source of the residual momentum, tests *NLT* and *hor. NLT* do not improve the inverse results or lower the residual momentum terms.

As mentioned in the text, the most significant differences in the *base case* depth-averaged vertical diffusion comparison occur during pressure-forced events where the ver-

tical diffusion of momentum near the bottom should be most important. Both tests with extrapolated velocity profiles (*extrap* and *geo extrap*) appear to better account for these downwelling conditions as the correlations for the vertically integrated vertical diffusion during downwelling winds are increased. Thus the discrepancies shown in Figure 4.6e are likely due to the lack of near bottom data. The overall correlations are reduced using extrapolated profiles yet, with A in the extrapolated areas set entirely by the method of extrapolation, non-physical values frequently exist at the transition depth.

As a final sensitivity test, repeating the binned Ekman transport fraction calculation for each iteration (open circles in Figure 4.9) illustrates that these differences do not significantly change the statistics of our main result. The majority of the test results fall within the confidence intervals for the base case, except at the highest bins. For this reason, our analysis focuses on the results of the *base case* only, using this as an estimate for the true eddy viscosity present during the study period.

4.9. Acknowledgments

This paper is a contribution of PISCO, the Partnership for Interdisciplinary Studies of Coastal Oceans funded primarily by the Gordon and Betty Moore Foundation and the David and Lucile Packard Foundation. We thank J. Lubchenco and B. Menge in establishing and maintaining the PISCO observational program at OSU. We also thank Captain P. York, C. Holmes, and S. Holmes for their data collection efforts, B. Kuebel-Cervantes for providing the model output used in the Appendix, and J. Lerzack, and M. Levine for helpful comments on the manuscript.

BIBLIOGRAPHY

Austin, J. and S. Lentz, 2002: The inner shelf response to wind-driven upwelling and downwelling. *J. Phys. Ocean.*, **32**, 2171.

Bane, J., M. Levine, R. Samelson, S. Haines, M. Meaux, N. Perlin, P. Kosro, and T. Boyd, 2005: Atmospheric forcing of the Oregon coastal ocean during the 2001 upwelling season. *J. Geophys. Res.*, **110**, doi:10.1029/2004JC002653.

Barth, J., B. Menge, J. Lubchenco, F. Chan, J. Bane, A. Kirincich, M. McManus, K. Nielsen, S. Pierce, and L. Washburn, 2007: Delayed upwelling alters nearshore coastal ocean ecosystems in the northern California Current. *PNAS*, **104**, 3719–3724.

Broitman, B., C. Blanchette, and S. Gaines, 2005: Recuitment of intertidal invertebrates and oceanographic variability at Santa Cruz Island, California. *Limnol. Oceanogr.*, **50**, 1473–1479.

Chapra, S. and R. Canale, 1988: *Numerical methods for engineers*. McGraw-Hill, 839 pp.

Deardorff, J., 1972: Numerical investigation of neutral and unstable planetary boundary layers. *J. Atmos. Sci.*, **29**, 91–115.

Ekman, V., 1905: On the influence of the Earth's rotation on ocean-currents. *Arkiv. Math. Astro. Fys.*, **2**, 1–53.

Farrell, T., D. Bracher, and J. Roughgarden, 1991: Cross-shelf transport causes recruitment to intertidal populations in central California. *Limnol. Oceanogr.*, **36**, 279–288.

Garvine, R., 2004: The vertical structure and subtidal dynamcis of the inner shelf off New Jersey. *J. Mar. Res.*, **62**, 337–371.

Huyer, A., 1983: Coastal upwelling in the California Current System. *Prog. Oceano.*, **12**, 259–284.

Kirincich, A., 2003: The structure and variability of a coastal density front. *Masters Thesis, University of Rhode Island*.

Kirincich, A. and J. Barth, 2007: Spatial and temporal variability of inner-shelf circulation along the central Oregon coast during summer. *J. Phys. Ocean., submitted*.

Kirincich, A., J. Barth, B. Grantham, B. Menge, and J. Lubchenco, 2005: Wind-driven inner-shelf circulation off central Oregon during summer. *J. Geophys. Res.*, **110**, doi:10.1029/2004JC002611.

Kuebel Cervantes, B., J. Allen, and R. Samelson, 2003: A modeling study of eulerian and lagrangian aspects of shelf circulation off Duck, North Carolina. *J. Phys. Ocean.*, **33**, 2070–2092.

Lentz, S., 1994: Current dynamics over the northern California inner shelf. *J. Phys. Ocean.*, **24**, 2461–2478.

— 1995: Sensitivity of the inner-shelf circulation to the form of the eddy viscosity profile. *J. Phys. Ocean.*, **25**, 19–28.

— 2001: The influence of stratification on the wind-driven cross-shelf circulation over the North Carolina shelf. *J. Phys. Ocean.*, **31**, 2749–2760.

Lentz, S. and D. Chapman, 2004: The importance of nonlinear cross-shelf momentum flux during wind-driven coastal upwelling. *J. Phys. Ocean.*, **34**, 2444–2457.

Lentz, S., R. Guza, S. Elgar, F. Feddersen, and T. Herbers, 1999: Momentum balances on the North Carolina inner shelf. *J. Geophys. Res.*, **104**, 18205–18226.

Lentz, S. and C. Winant, 1986: Subinertial currents on the southern California shelf. *J. Phys. Ocean.*, **16**, 1737–1750.

Mellor, G. and T. Yamada, 1982: Development of a turbulence closure model for geophysical fluid problems. *Rev. Geophys. and Space Phys.*, **20**, 851–875.

Miller, B. and R. Emlet, 1997: Influence of nearshore hydrodynamics on larval abundance and settlement of sea urchins Stronglocentrotus franciscanus and S. purpuratus in the Oregon upwelling zone. *Ecol. Prog. Ser.*, **148**, 83–94.

Mitchum, G. and A. Clarke, 1986: The frictional nearshore response to forcing by synoptic scale winds. *J. Phys. Oceano.*, **16**, 934–946.

Panchang, V. and J. Richardson, 1993: Inverse adjoint estimation of eddy viscosity for coastal flow models. *J. Hydr. Eng.*, **119**, 506–524.

Pawlowicz, R., B. Beardsley, and S. Lentz, 2002: Classical tidal harmonic analysis including error estimates in MATLAB using T_TIDE. *Computers and Geosciences*, **28**, 929–937.

Perlin, A., J. Moum, J. Klymak, M. Levine, T. Boyd, and P. Kosro, 2005: A modified law-of-the-wall applied to oceanic bottom boundary layers. *J. Geophys. Res.*, **110**, doi:10.1029/2004JC002310.

Samelson, R., P. Barbour, J. Barth, S. Bielli, T. Boyd, D. Chelton, P. Kosro, M. Levine, and E. Skyllingstad, 2002: Wind stress forcing of the Oregon coastal ocean during the 1999 upwelling season. *J. Geophys. Res.*, **107**, doi: 10.1029/2001JC00900.

Signell, R., R. Beardsley, H. Graber, and A. Capotondi, 1990: Effect of wave-current interaction on wind-driven circulation in narrow, shallow embayments. *J. Geophys. Res.*, **95**, 9671–9678.

Smith, J. and C. Long, 1976: The effects of turning in the bottom boundary layer on continental shelf sediment transport. *Mem. Soc. Roy. Sci. Liege. Ser.*, **6**, 369–396.

Tilburg, C., 2003: Across-shelf transport on a continental shelf: do across-shelf winds matter? *J. Phys. Oceano.*, **33**, 2675–2688.

Wiseman, W. and R. Garvine, 1995: Plumes and coastal currents near large river mouths. *Estuaries*, **18**, 509–517.

Yankovsky, A., R. Garvine, and A. Munchow, 2000: Mesoscale currents on the inner New Jersey shelf driven by the interaction of buoyancy and wind forcing. *J. Phys. Oceano.*, **5**, 2214–2230.

Yu, L. and J. O'Brien, 1991: Variational estimation of the wind stress drag coefficient and oceanic eddy viscosity profile. *J. Phys. Ocean.*, **21**, 709–719.

	eddy viscosity (A)				Depth averaged vertical diffusion		Residual momentum std. dev.	
	(m^2 s^{-1})x10^{-3}			%	$\tau_y < 0$	$\tau_y > 0$	(m s^{-2})x10^{-6}	
run	mean	50%	99%	positive	CC	CC	across	along
base case	1.3	0.8	10.6	98.48	0.88	0.29	1.5	0.8
course grid	1.4	0.8	10.8	98.43	0.88	0.29	1.6	0.9
fine grid	1.2	0.7	10.4	98.17	0.88	0.31	1.4	0.7
geo	1.7	1.2	10.7	98.75	0.70	0.54	1.8	1.7
geo extrap	1.8	1.1	12.1	95.95	0.60	0.68	4.7	3.8
geo tidal	1.9	1.5	7.4	94.90	0.53	NS	4.7	1.5
extrap	1.3	0.7	11.2	96.91	0.91	0.77	2.7	2.1
tidal	1.7	1.3	6.8	92.87	0.36	NS	1.2	1.0
NLT	1.5	0.9	11.5	98.40	0.62	0.29	2.0	1.4
hor. NLT	1.3	0.7	11.1	98.56	0.84	0.31	1.7	1.1
dP/dx=0	1.2	0.7	10.0	96.34	0.87	0.43	1.6	1.1
ASgeo	1.3	0.7	10.6	98.34	0.86	0.29	1.6	1.0
buoy winds	1.3	0.8	7.8	98.64	0.90	NS	2.1	1.3
reduced winds	1.1	0.6	8.6	98.58	0.88	0.28	1.3	0.7

TABLE 4.1: Inverse model sensitivity testing. See text for run descriptions. NS means not statistically significant.

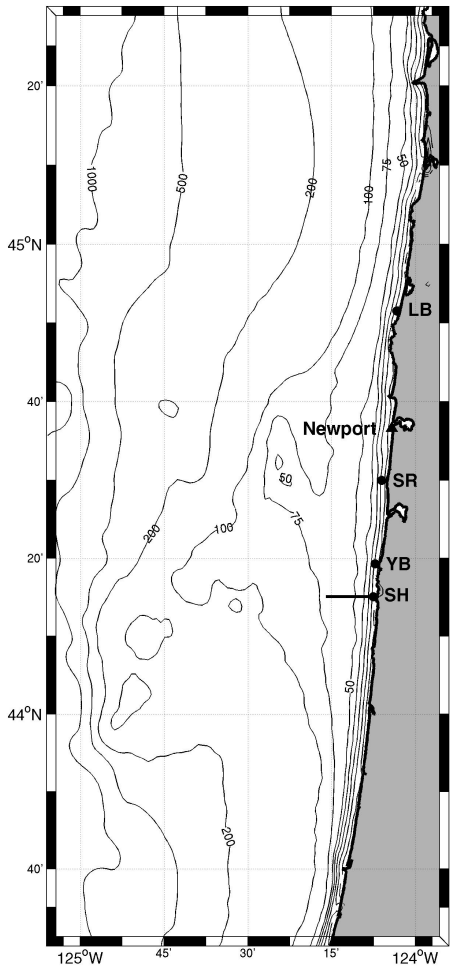

FIGURE 4.1: The central Oregon shelf with the 2004 PISCO stations (dots) and the Newport CMAN station (triangle) marked. The bold line offshore of SH marks the transect line occupied during the high resolution ship-based surveys. Isobaths (thin, black lines) are marked in meters.

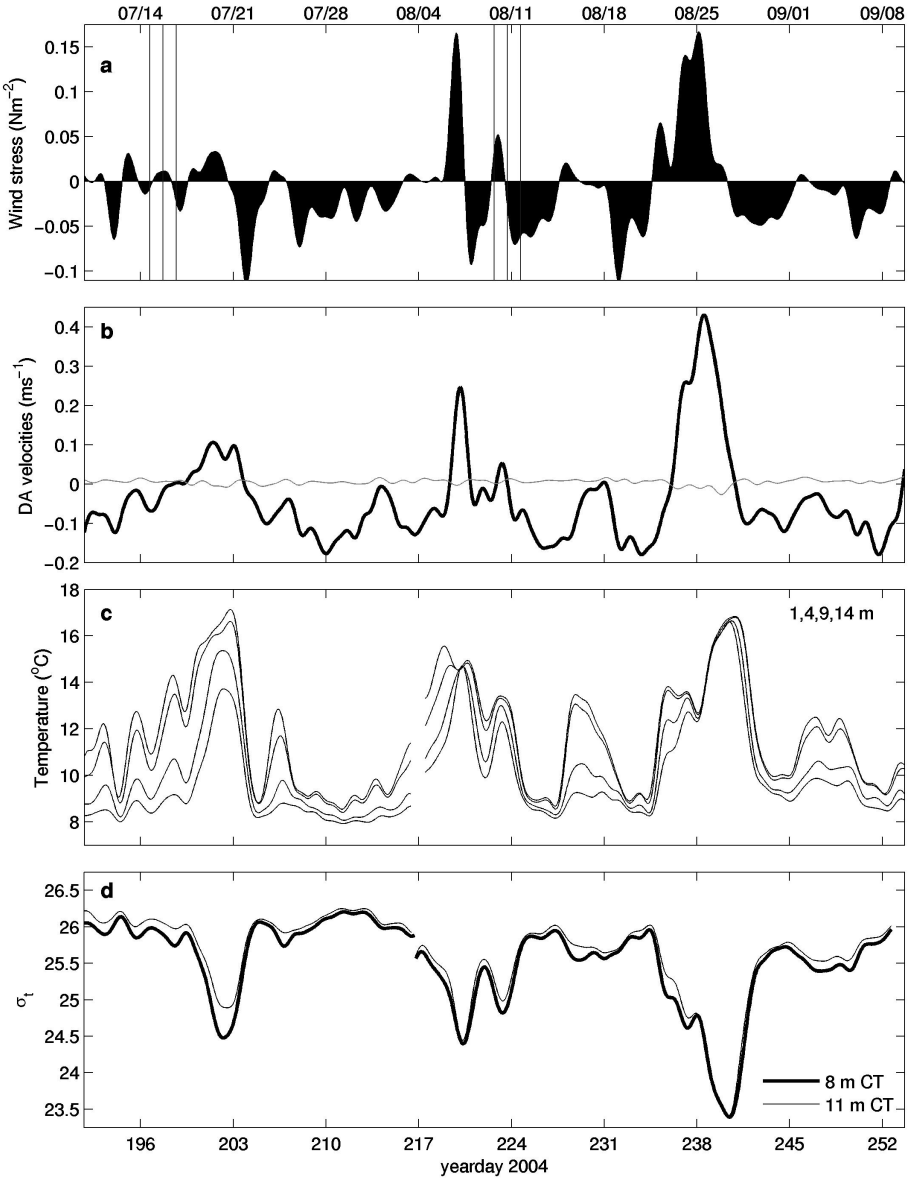

FIGURE 4.2: Observed **(a)** along-shelf wind stress at Newport with Acrobat section times marked by vertical lines and **(b)** depth-averaged along- (bold) and across-shelf (thin) velocities, **(c)** temperature, and **(d)** density at station SH.

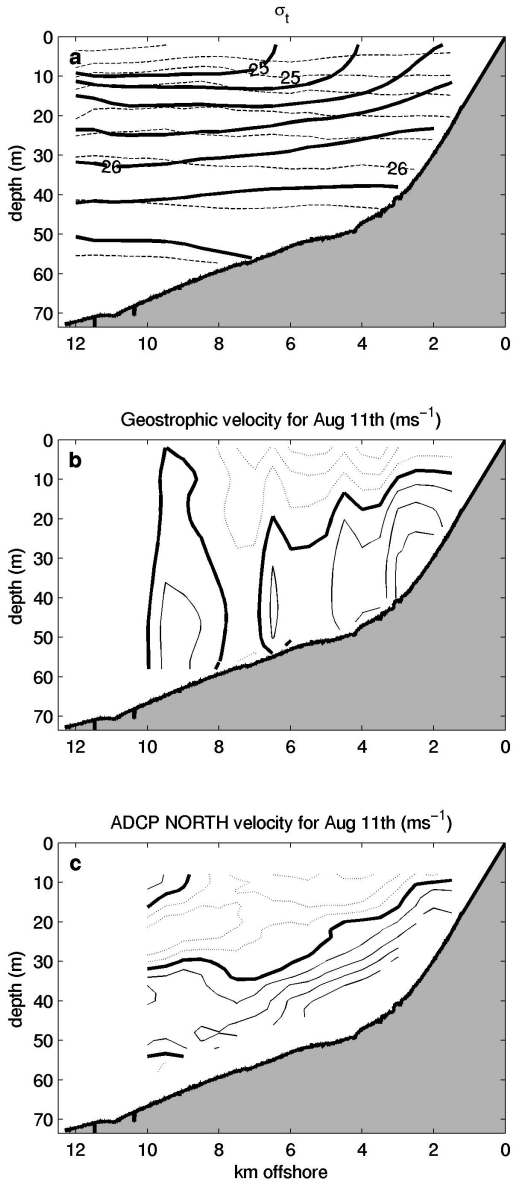

FIGURE 4.3: **(a)** Observed across-shelf hydrographic structure offshore of SH 15 on Aug 10th (day 223, dashed) and 11th (day 224, solid) lines, **(b)** the geostrophic (via the thermal wind equation) velocity for Aug 11th, and **(c)** average northward velocities for Aug 11th from R/V Elakha's shipboard ADCP. In the lower panels, southward velocities (dashed) and northward velocities (solid) are marked every 0.025 m s^{-1}. The bold, solid line is the 0 m s^{-1} contour.

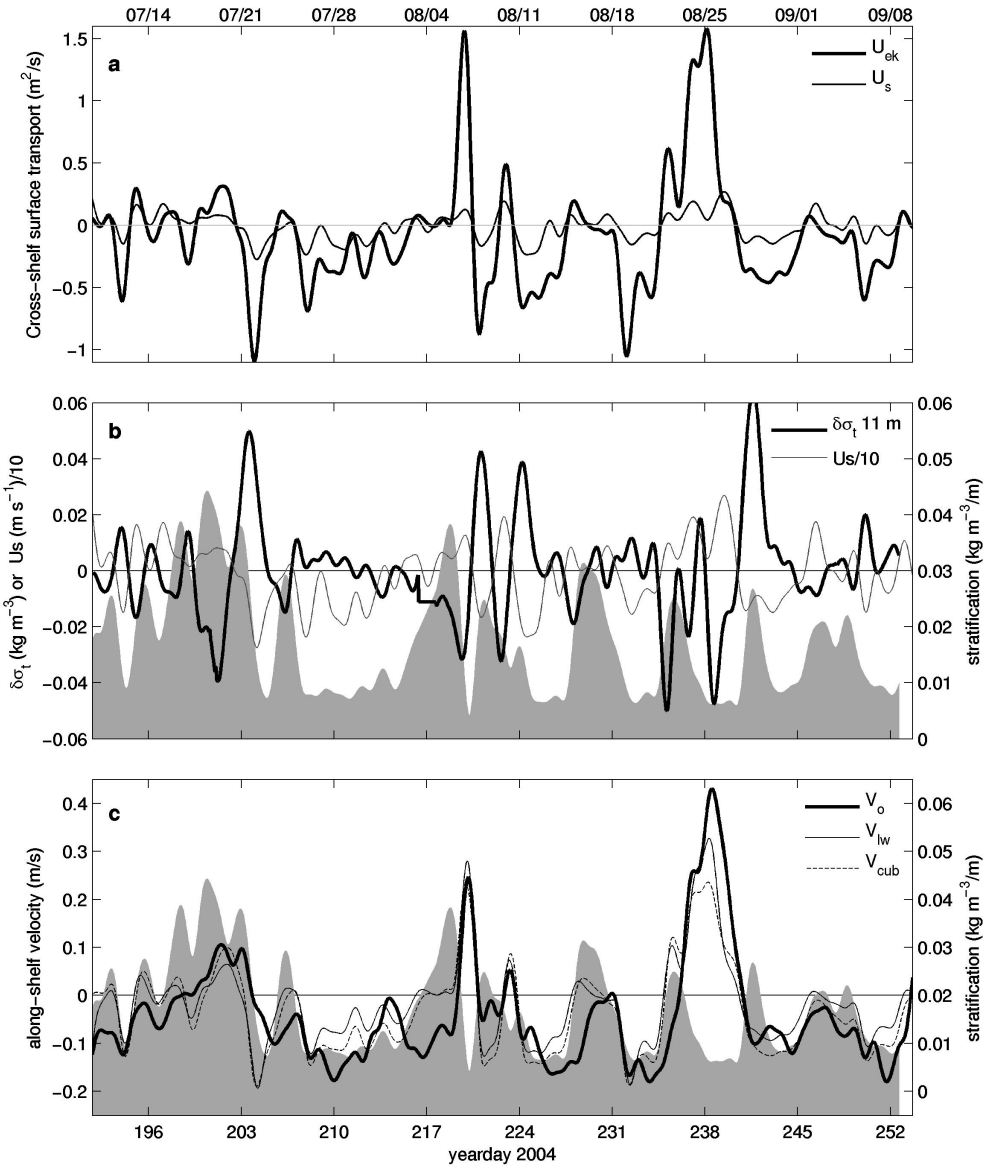

FIGURE 4.4: **(a)** Theoretical (bold) and measured (solid) across-shelf transport in 15 m of water at station SH. **(b)** Density stratification (shaded background), time rate of change of density at 11 m depth ($\delta\sigma_t$ - bold), and measured across-shelf transport divided by 10 ($Us/10$ - solid). **(c)** Density stratification (shaded background) and depth-averaged along-shelf velocities from observations (V_o), the Lentz and Winant (1986) analytical model (V_{lw}), and the 1D numerical model with a cubic eddy viscosity profile (V_{cub}).

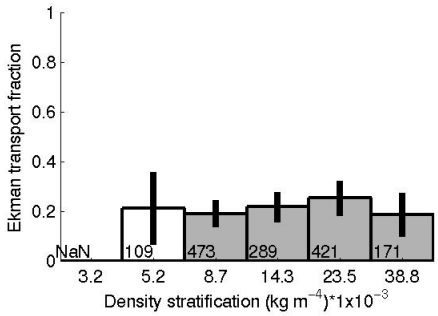

FIGURE 4.5: Ekman fraction calculation, following (Kirincich et al., 2005), for station SH surface transport and theoretical Ekman transport, binned by density stratification. Results where the measured and theoretical transports are significantly correlated (at the 95% confidence interval) are shaded. Confidence intervals for the regression are shown as vertical lines on each bar. The number of hours in each stratification bin are listed as well.

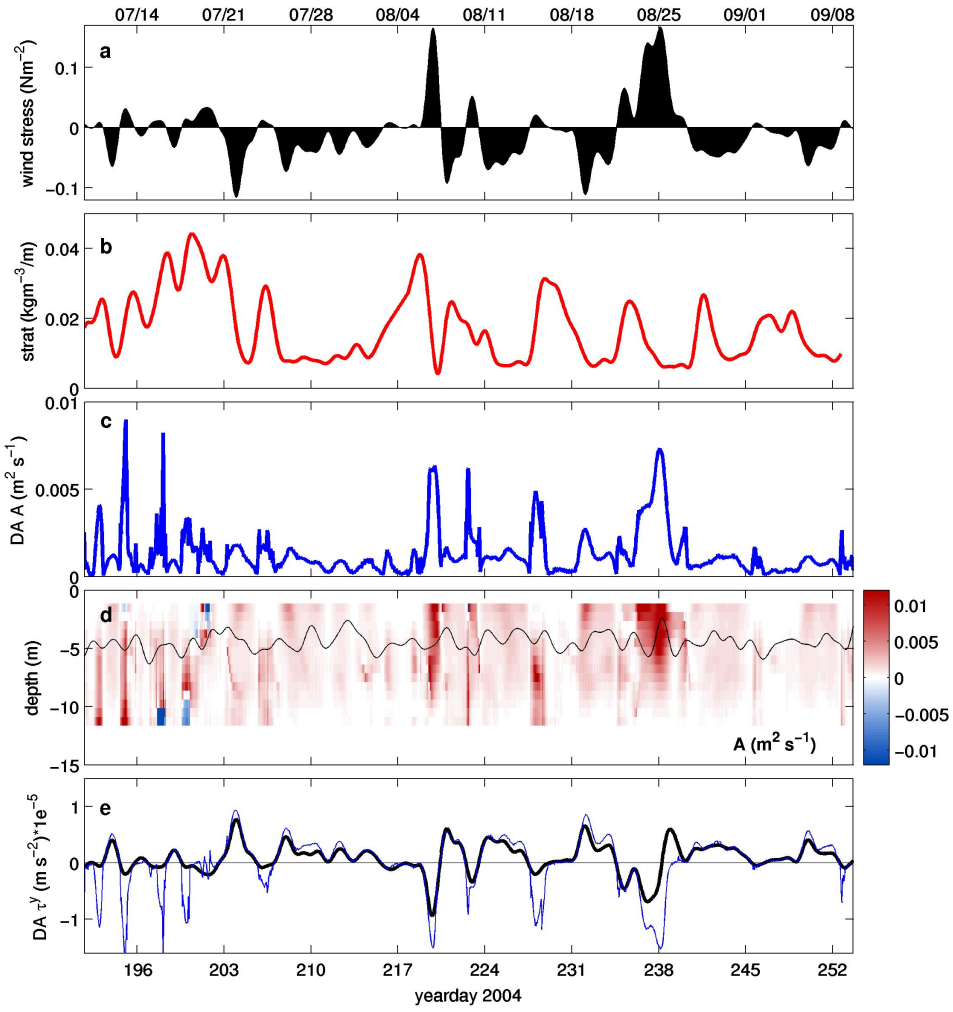

FIGURE 4.6: The **(a)** North wind stress and **(b)** density stratification along with estimated **(c)** depth-averaged and **(d)** full eddy viscosity. The location of the zero-crossing of the across-shelf velocity profile is included here as the black line. **(e)** A comparison of the estimated (thin) and theoretical (bold) depth-averaged vertical turbulent diffusion of horizontal momentum terms.

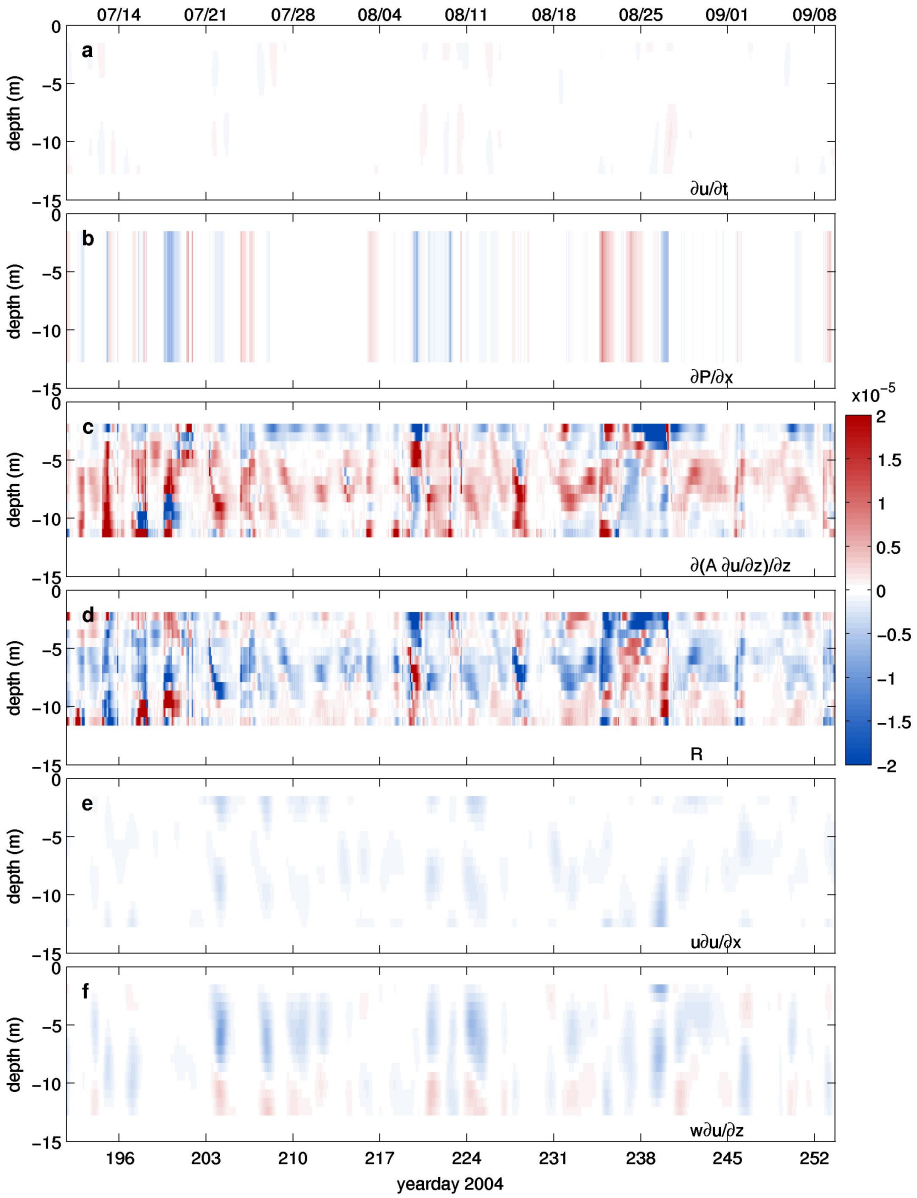

FIGURE 4.7: Terms in the across-shelf momentum balance (m s^{-2}): **(a)** acceleration, **(b)** non-geostrophic pressure gradient, **(c)** vertical diffusion, **(d)** 'residual' momentum, and estimates of the **(e)** along-shelf and **(f)** vertical advection terms. Terms are shown as they would appear on the left side of equation 4.2.

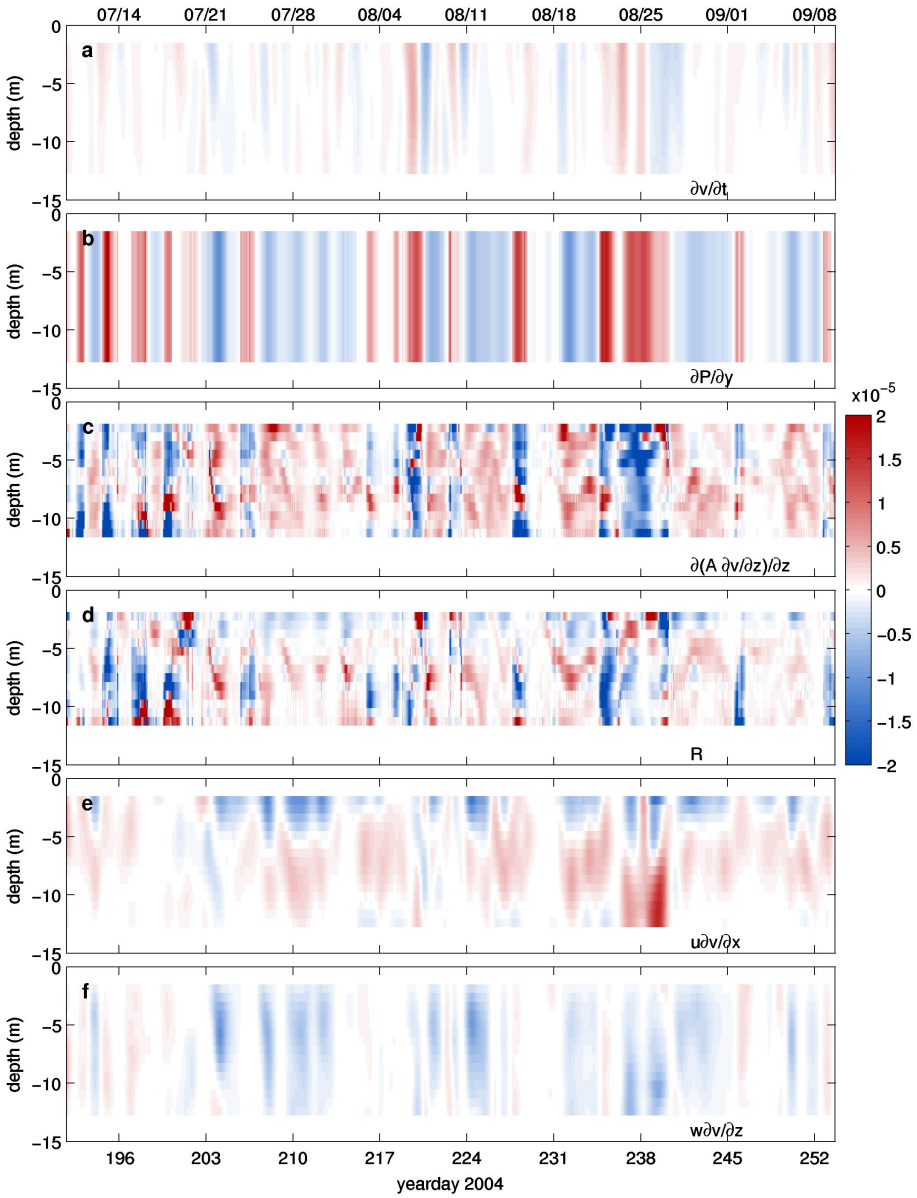

FIGURE 4.8: Terms in the along-shelf momentum balance (m s^{-2}): **(a)** acceleration, **(b)** non-geostrophic pressure gradient, **(c)** vertical diffusion, **(d)** 'residual' momentum, and estimates of the **(e)** along-shelf and **(f)** vertical advection terms. Terms are shown as they would appear on the left side of equation 4.3.

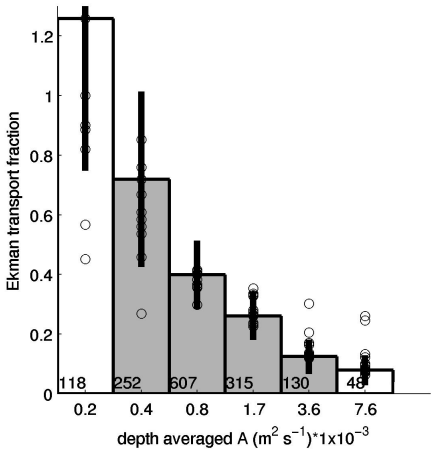

FIGURE 4.9: Ekman fraction calculation binned by the depth-averaged eddy viscosity (A). Open circles are estimates using the sensitivity runs described in the appendix.

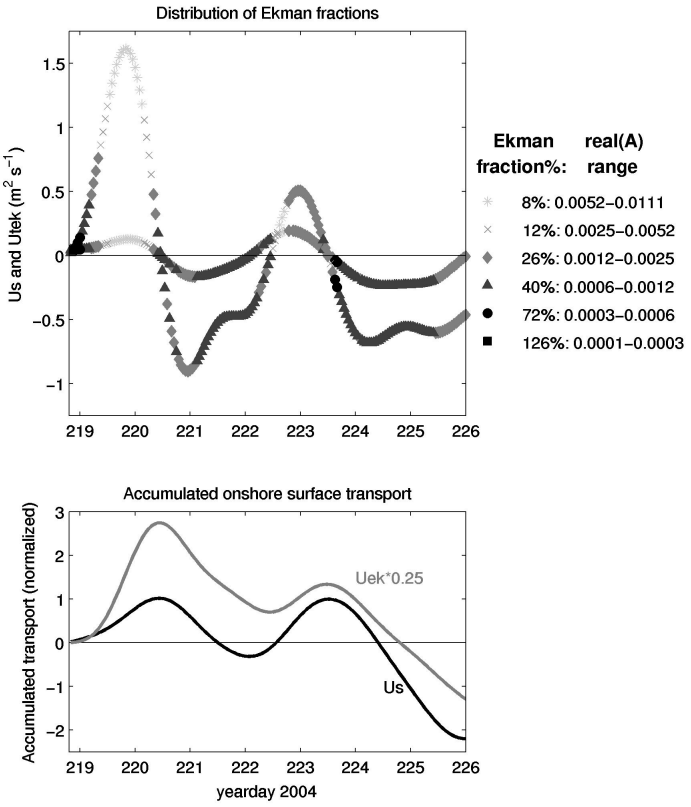

FIGURE 4.10: Temporal variability of eddy viscosity and its effects on circulation during year days 218-226. **(top)** The ranges of A used in the Ekman transport fraction calculation shown in Figure 4.9 are distributed on time series of theoretical Ekman transport ($Utek$, large variations) and measured surface transport (Us, smaller variations). **(bottom)** Illustrating the effects of eddy viscosity variability on across-shelf transport, the accumulated mean theoretical Ekman transport ($Utek * 0.25$-the mean fraction for this station) and measured surface transport (Us) are shown, normalized by the volume of the inner-shelf inshore of station SH.

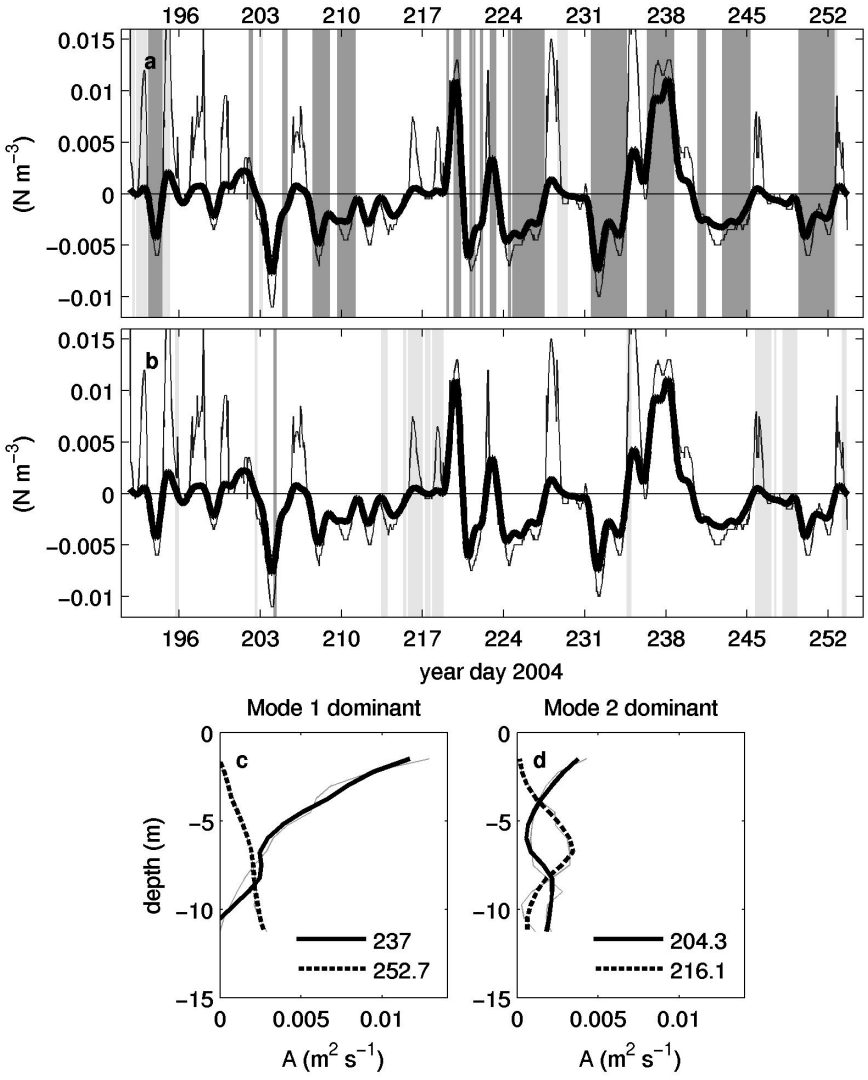

FIGURE 4.11: The vertical structure of the estimated eddy viscosity at station SH. Panels **(a)** and **(b)** both show the along-shelf wind (τ^y/H, thick line) and matched along-shelf, non-geostrophic pressure gradient (dP/dy, thin line) superimposed on vertical bars denoting the occurrence of positive and negative mode one **(a)** and mode two **(b)** dominant conditions. In both panels, positive (negative) modal conditions are shaded darker (lighter) while no shading (white) indicates times when the mode was not dominant (see text). Examples of the vertical structure of A during times of positive and negative mode one **(c)** and mode two **(d)** dominance are shown below. Thick profiles, solid (dashed) during positive (negative) modal amplitudes, are composites of the first three modes while the thinner profiles for each are the full A estimated from the inverse calculation.

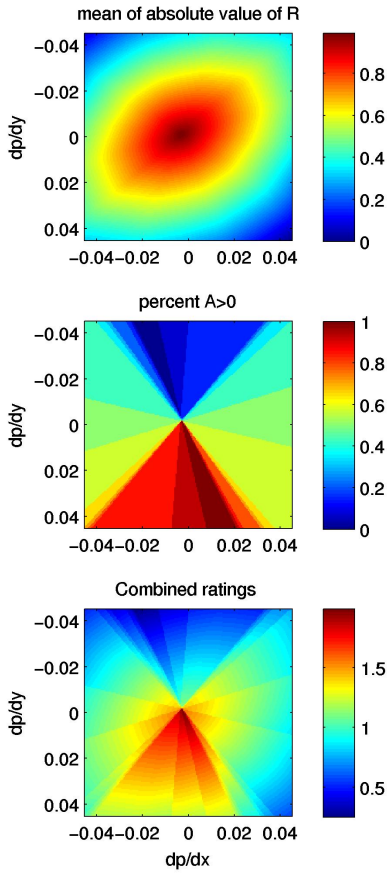

FIGURE 4.12: Sample of pressure matching technique. The two quantities, the depth average of the absolute value of the residual momentum and the percent of positive A values, are shown with their normalized and combined rating in the lower panel. The matching technique picks the vertically-uniform, non-geostrophic pressure gradients corresponding to the maximum value of the combined metric.

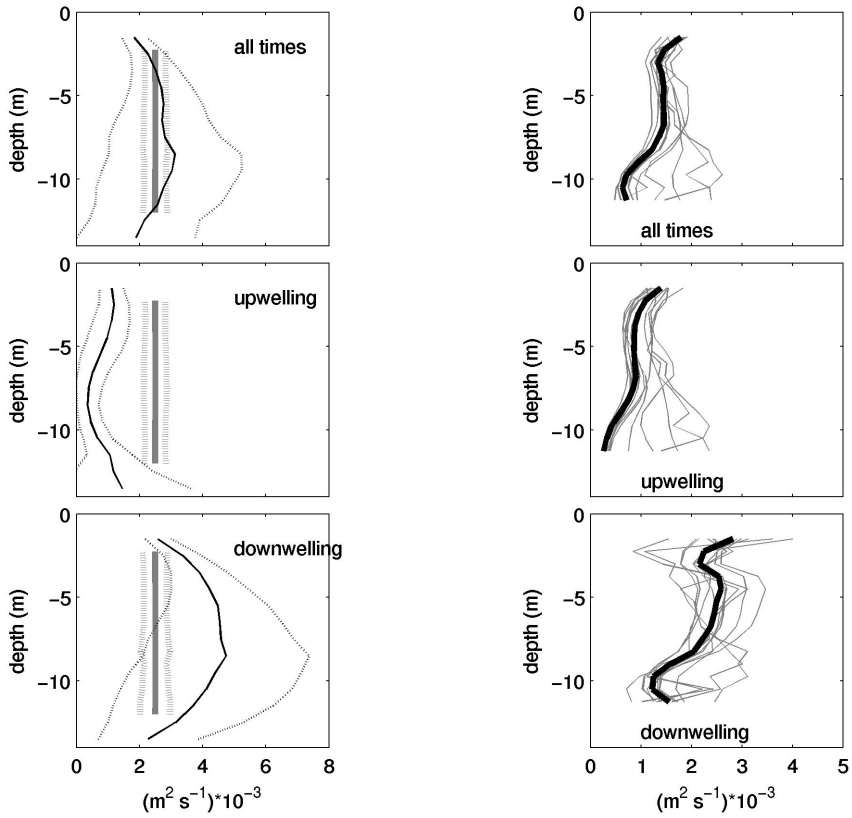

FIGURE 4.13: (**Left panels**) Given mean eddy viscosities for the 1D forward model of Lentz (1994) (*gray, thick lines*) and the 2D forward model of Kuebel Cervantes et al. (2003) (*black, thin lines*) for all times (***top panels***), upwelling favorable along-shelf winds (***middle panels***), and downwelling favorable along-shelf winds (***bottom panels***). RMS differences between given model eddy viscosities and that estimated using the inverse calculation are shown as dashed windows about the means. (**Right panels**) Estimated mean eddy viscosity for the *base case* inverse calculation of station SH data (*black line*) and all other sensitivity tests (*gray lines*)for similar forcing conditions. Only data where the total vertical shear of the horizontal velocity was greater than 0.005 s^{-1} was included in all panels.

5. CONCLUSIONS

This dissertation has analyzed inner-shelf circulation along the central Oregon coast using observations from an ongoing long-term monitoring program. As this area has been poorly sampled in the past, this work has increased our understanding of inner-shelf dynamics as well as the nature of circulation in the inner-shelf along the central Oregon coast. Collectively, these results help better explain the transition of physical processes that control across-shelf exchange between the surf zone onshore and the larger coastal ocean offshore. This final chapter summarizes the main points of the previous three, synthesizing the results into a coherent picture of inner-shelf circulation off the central Oregon coast and applying them to ecological systems in the region. Additionally, new research questions about inner-shelf dynamics, or refined old ones, have been identified throughout the study. Below, a complete summary of the physical results is given first, followed by an in-depth discussion of their ecological implications and inner-shelf questions deserving further research.

5.1. Summary of inner-shelf circulation results

In Chapter 2, velocity measurements from 17 deployments of moored acoustic Doppler current profilers, obtained during the summer upwelling season, were used to describe the across-shelf divergence of Ekman transport in the inner shelf. For each deployment, the measured surface and bottom across-shelf transports were compared with estimates of the theoretical Ekman transports to find the fraction of full theoretical Ekman transport present. In general, in 15 m of water at 1-2 km offshore, measured transport was 25% of the full Ekman transport. Measured transports reached full Ekman transport 5-6 km offshore in 50 m of water. Thus, the mean region of active upwelling marked by

the divergence of Ekman transport was limited to a narrow region along the coast. The relationship between transport fraction and water depth was similar to that found by Lentz (2001) off the North Carolina coast. This similarity indicates the dominant effect of the Ekman layer thickness and water depth on the Ekman divergence despite varying shelf widths, stratification, or forcing conditions. Average transport fractions at each station were similar from year to year, and no significant along-shelf trends in the transport fractions were observed. The one exception to this, station FC, is located just north of a local topographic and bathymetric feature. Based on the large and variable rotation of horizontal currents with depth, local topography exerts a strong control of flow at station FC. At station LB, 2 km north of station FC, circulation appears more consistent with stations to the south. A weak linear relationship exists between transport fractions calculated over shorter time periods and stratification. Thus it appears that as stratification decreases, the theoretical boundary layers thicken and less across-shelf tranport is realized.

In Chapter 3, a description of inner-shelf circulation along the central Oregon coast was given using measurements obtained in water depths of 15 m during the summer of 2004. Although wind forcing and bathymetry are nearly spatially uniform in the inner-shelf, distinct differences in circulation existed among four stations spanning 70 km along the coast. North of an offshore submarine bank at station LB, time dependent upwelling circulation was similar to classic two-dimensional (2D) upwelling with bottom stress and acceleration balancing wind stress in the depth-averaged along-shelf momentum equation. In contrast, this 2D balance was poor onshore of the bank at the southern three stations where the pressure gradient and nonlinear terms were needed to better close the balance. During downwelling events the 2D balance held well at the southern sites, but poorly at the northern site. The dominant mode of variability, found using an EOF analysis of pressure, along-shelf velocity, across-shelf surface transport, and density, was positively correlated to the local wind forcing and present at all stations. A second mode drives additional

upwelling or downwelling at the northernmost station (LB), and may result from remote forcings that alter the larger scale upwelling circulation but not the circulation of the 'mini-jet' inshore of the bank. The observed temporal and spatial differences result from region-wide flow-topography interactions which leave the on-bank stations in a lee. By late summer, inner-shelf flow during upwelling is strong and southward north of the bank, weak and onshore on the northern part of the bank, and increasingly southward on the southern part of the bank. Coupled with previous outer- and mid-shelf observations (Barth et al., 2005a,b; Kosro, 2005) and modeling studies (Oke et al., 2002a,b; Gan and Allen, 2005) conducted in the region, these results provide an improved picture of shelf-wide circulation along the central Oregon coast during summer.

In Chapter 4, the temporal variability of the across-shelf scale of the divergence of Ekman transport was examined in detail as it controls the efficiency of across-shelf transport in the inner-shelf. At station SH during the late summer of 2004, hydrographic and velocity observations highlight the rapid across-shelf movement of water masses and variable residence times that exist in the inner shelf. Conditions changed from weak stratification and strong northward currents during downwelling favorable winds to stronger stratification and southward currents during upwelling favorable winds over event timescales of 2-7 days. Additional shipboard observations indicated that along-shelf velocities could be in thermal wind balance with density structure at these shallow water depths, but was highly dependent on local wind-driven upwelling. To better understand the time variability of across-shelf exchange, an inverse calculation was used to estimate eddy viscosity and vertical turbulent diffusion of momentum from profiles of velocity and wind forcing. Depth-averaged estimated eddy viscosity varied over a large dynamic range, averaging $0.8\text{x}10^{-3}$ m^2 s^{-1} during upwelling winds and $2.1\text{x}10^{-3}$ m^2 s^{-1} during downwelling winds, and was consistent with previous numerical modeling studies. The fraction of full Ekman transport present in the surface layer, a measure of the efficiency of across-shelf exchange

at this water depth, was found to be a strong function of eddy viscosity. Transport fractions ranged from 80-100% during times of rapidly changing stratification and forcing, and low eddy viscosity, to 10-20% during times of weak stratification, strong forcing, and large eddy viscosity. The difference in eddy viscosities between upwelling and downwelling leads to varying across-shelf exchange efficiencies and, potentially, increased net upwelling over time. The vertical structure of eddy viscosity was surface intensified during wind forcing, bottom intensified during pressure forcing, and bi-modal (cubic) during mixed forcing or transitions events. Additionally, an analysis of the residual terms from the inverse calculation, including a comparison with estimates of the nonlinear terms in the along- and across-shelf momentum equations, suggests the importance of a vertically-uniform alongshelf pressure gradient and both the across-shelf and vertical advection terms in these shallow waters.

The results described above have answered key questions regarding inner-shelf dynamics on wind-forced shelves. The across-shelf scale of coastal upwelling on the central Oregon coast was defined and its strong dependence on water depth shown. Temporal variations of this across-shelf transport were quantified and related to variations in eddy viscosity, wind forcing, and stratification. Finally, the seasonal evolution of inner-shelf circulation along the central Oregon coast was described and placed in the context of the region-wide circulation.

5.2. Ecological implications

The implications of these results to ecological communities in the region have been sprinkled throughout the discussions of the previous chapters. Here they are collected and extended to develop a clear picture of the coastal ocean's affects on nearshore ecosystems, providing a foundation for future interdisciplinary studies.

The mean across-shelf scale of coastal upwelling along the Oregon coast was defined in Chapter 2. That only 25% of the theoretical Ekman across-shelf transport occurs at water depths of 15 m means that only 25% of the waters upwelled over the shelf have access to the inner-shelf inshore of this depth. This is a small fraction of the total waters upwelled, and it has been used to justify the importance of additional mechanisms of across-shelf exchange (Fewings et al., 2007) in other regions. However, the total volume of water inshore of this water depth along the Oregon coast is also quite small. With the 15 m isobath located (at maximum) 1.5 km offshore, assuming a wedge shaped across-shelf section with unit along-shelf width gives a 11250 m^3 volume inshore of 15 m. A typical across-shelf velocity of 0.025 m s^{-1} in the top half of the water column could fully flush this volume in under 17 h, or about one inertial period at this latitude. Thus, even this reduced mean Ekman transport fraction is sufficient to exchange water masses, nutrients, and larvae in the inner-shelf rapidly. Yet as the results from Chapter 4 show, across-shelf exchange can happen much faster than the mean picture described above. Across-shelf transport is highest during transitions between downwelling and upwelling events, and the instantaneous fraction of full transport during upwelling can be as much as double the mean value found.

The description of inner-shelf circulation along the central Oregon coast outlined in Chapter 3 has a number of important implications for the regional marine ecosystem. The varying fates of inner-shelf waters north of the bank and those onshore of the bank appear to explain known regional variations in ecological processes. A key difference between the southward transport at stations YB and SH, inshore of the bank, and station LB north of the bank, is that LB waters are diverted offshore and around the bank, while YB and SH waters tend to remain closer to shore. Inner-shelf (and surf zone) chlorophyll *a* concentrations, a proxy for phytoplankton biomass, at station SH are consistently higher than at station LB in the north (Leslie et al., 2005). Offshore of the southern sites, the low

flow region over the bank is also high in chlorophyll *a* (Barth et al., 2005a). Perhaps as a result, growth rates of barnacles (*Balanus glandula*) and mussels (*Mytilus californianus*) in the adjacent intertidal zone are higher at these on-bank stations when compared to station LB. Barnacles also have been found to produce more larvae at the southern on-bank sites (Leslie et al., 2005). Previous studies (Leslie et al., 2005; Barth et al., 2005a) have suggested a link between the low flow area over the bank offshore and increased primary production and consumers both offshore and onshore. The inner-shelf circulation results presented here carry the connection across the transition zone, providing much stronger evidence of these interactions.

The seasonal development of this circulation pattern appears to explain the location and timing of mussel larval recruitment. The cumulative along-shelf transports from the 2004 season infer that the stagnation point of along-shelf flow in the inner-shelf shifts northward from station YB, early in the season, to station SR later in the season as the inshore jet spins up to the south. Although recruitment is generally elevated between May and August in the region (Connolly et al., 2001), recruitment of mussels at stations YB and SR are higher than all other sites to the north and south based on 8-17 years of monthly recruitment data (Barth et al., 2007) *(see their Figure 6)*. However, the timing of peak recruitment also varies by site. Peak recruitment occurs in July at YB, coinciding with the time of weakest southward flow at that station (Barth et al., 2007). As the season progresses, the stagnation point moves north to station SR as the inshore jet spins up to the south. This circulation pattern is well underway when mussel recruitment peaks at station SR in September. Thus peak mussel recruitment at these sites is roughly timed with the seasonal development and along-shelf movement of the stagnation point of along-shelf, upwelling-driven flow.

In contrast to mussels, barnacle recruitment at stations YB and SR are similar to sites both to the north and south (Barth et al., 2007). The recruitment differences

between the two species may be due to life cycle characteristics. Recent work has shown that recruiting barnacles are more frequently found near the surface (Rilov, 2007), and that barnacle settlement pulses appear to be positively correlated with the warmer water temperatures associated with downwelling or relaxation events Broitman et al. (2005).

The analysis of Chapter 4 identified episodes of total water mass exchange, the sequestering of water masses in the extreme inner shelf, and the progression of transport efficiency during wind forcing events. These variations to the mean picture of upwelling or downwelling above have significant implications for food availability and recruitment events of inner-shelf ecological communities. If barnacle settlement is indeed linked to downwelling events (Roughgarden et al., 1998; Dudas et al., 2007), the variable efficiency of across-shelf exchange during transitions might exert a strong control on the recruitment process. These physical conditions would favor recruitment from individuals that amass at the front (or the highest level of stratification) as this water mass has the highest likelihood of onshore delivery during reversals. During the initial transition between upwelling and downwelling or a relaxation event, decreased eddy viscosity and increased across-shelf transport efficiency allow a full flushing of the inner-shelf and replacement with warmer surface waters. Once this transition has occurred, eddy viscosity increases and across-shelf circulation efficiency decreases as the water de-stratifies. Larvae or parcels behind the leading edge or front would have a reduced opportunity of passive onshore transport as this process causes across-shelf currents to shutdown. Thus, this pulse of increased transport efficiency appears to provide a mechanism for focused successful on-shore transport of propagules during a downwelling burst. Similar particle trajectories have been seen in inner-shelf modeling results (Austin and Lentz, 2002; Kuebel Cervantes et al., 2003; Tilburg, 2003). Additionally, ecological evidence also exists for aggregation near fronts or areas of strong velocity shear. A recent laboratory study (Woodson et al., 2005) found that planktonic copepods tended to aggregate at velocity or density gradients, and moored

observations of larval surfclam concentrations on the New Jersey coast (Ma and Grassle, 2004) found the highest concentrations during the passage of strong density gradients.

The shutdown of across-shelf transport after the initial transition from upwelling and downwelling may actually work in favor of recruitment at some PISCO sites. Larvae in the inner-shelf after the initial transition would tend to stay closer to shore for a longer period of time than if released during normal upwelling conditions, as across-shelf transport efficiency is low during this time. Given the strong northward flows that occur at all stations during downwelling events, but especially station SR, this feature suggests that the on-bank sites could be a source of larvae for sites to the north. Northward, downwelling-driven velocities of up to 0.3 m s^{-1} would enable water from station SR to transit the 26 km to stations FC/LB in approximately one day. Thus a high larval pool in the stagnation point at SR could supply FC/LB recruitment during these downwelling events, if the larvae released at FC/LB are swept offshore by the bank during upwelling. If true, this mechanism would also explain the spatial uniformity in barnacle recruitment along the Oregon coast shown by Barth et al. (2007).

Finally, due to the variability of across-shelf transport efficiency, the dynamics of the inner-shelf tend to bias net across-shelf transport in favor of upwelling. As shown in Chapter 4, an estimate of across-shelf transport at 15 m water depth, formed by multiplying the theoretical Ekman transport times the season-long mean Ekman transport fraction at station SH (0.25), underestimates the net amount of across-shelf transport at the 15 m isobath during variable forcing conditions. This implies that more nutrient-rich water upwelled into the inner-shelf inshore of 15 m than that predicted. As a result, inner-shelf waters are refreshed more often and farther inshore then previously thought. Thus an upwelling metric such as the Bakun upwelling index, based on winds and mean dynamics only, might under-predict the total upwelling in this inshore area. With a overall bias toward onshore transport at depth during upwelling, larvae able to adjust their buoyancy and move downward into the bottom return flow would be able to move onshore in a

predicable manner.

5.3. Next steps

While these results have extended our picture of shelf-wide circulation off Oregon into the inner-shelf and increased our understanding about across-shelf exchange on this wind-driven shelf, additional work remains. A number of further steps that would improve upon the existing work are described below, including obtaining better numerical and observational estimates for the vertical turbulent diffusion of momentum, and better estimates of the nonlinear momentum terms. Finally, ideas for future efforts to bridge the remaining gaps in across-shelf exchange are discussed.

The inverse calculation for eddy viscosity used in Chapter 4 may be useful in future dynamical studies, and thus additional refinements to the method could greatly improve results. As seen in the sensitivity testing, full water-column profiles of velocity would improve the analysis, especially by filling in the larger data gap along the bottom. Increased vertical resolution of velocity observations would also help, decreasing errors from the bin-averaging process. More rigorous improvements to the method, whether by adding variational estimation methods or a full data-assimilating model, could further decrease calculation errors. The addition of a variational optimization technique into the calculation outlined in Chapter 4 is a natural next step, and would better account for errors in the wind stress or velocity profiles. The work of Yu and O'Brien (1991) could be extended to include a time-dependent eddy viscosity profile and vertically-uniform pressure gradients. However, as the authors discuss in a follow-up work (Yu and O'Brien, 1992), correctly defining the initial conditions is a source of difficulty with this method, requiring additional effort to efficiently overcome. Also, the geostrophically balanced velocity shear would remain a significant issue. Subtracting this geostrophic shear first aids the

inverse calculation during upwelling, but appears to hinder it during downwelling. It is not readily apparent how to appropriately account for this dynamical difference in the inverse calculation. Despite these issues, successful results from this inverse method could make an interesting test case for examining the appropriateness of different turbulent closure parameterizations, akin to the forward model-only efforts by Durski et al. (2004) and Wijesekera et al. (2003). Further increasing in complexity, a 3D data assimilation model, assimilating water velocities, could better account for the occurrence of geostrophically balanced vertical shear as well as additional momentum sources or sinks. Yet, if a turbulent closure parameterization is included in the forward model, its choice would clearly influence the resulting eddy viscosity profiles, reducing the independence of the vertical diffusion estimates.

A more direct method to derive estimates of vertical diffusion is through the use of ADCP velocities to calculate turbulent stresses within the water column. These 'variance' methods (Stacey et al., 1999; Williams and Simpson, 2004) have been used in estuaries (Whipple and Luettich, 2005) and tidal channels (Lu and Lueck, 1999) to estimate Reynolds stresses in the presence of surface-gravity waves, but have yet to be proven in the stratified coastal ocean. A recent change in PISCO's observational methods has enabled the development and use of this method to estimate turbulent Reynolds stresses off the Oregon coast. Starting in 2007, PISCO deployed ADCPs have been modified to record single pings, as opposed to ensemble averages, enabling long-term estimates of stresses and thus vertical diffusion. This observational method, along with the expanded inverse calculation methods discussed above, can significantly further our understanding of how forces are transmitted through the water column, how this process varies over time, and the implications for inner-shelf circulation.

In addition to vertical diffusion, this analysis found that the non-linear advective terms also need further work. The depth-dependent momentum balance analysis of Chap-

ter 4 appeared to give conflicting results. The comparison of the inverse results with estimates of the across-shelf and vertical advective terms found that much of the residual momentum could be visually explained by these two advective terms. However, inclusion of these estimates into the inverse calculation did not noticeably improve the results. This discrepancy infers that the standard PISCO array is ill-suited to accurately estimate the spatial gradients of horizontal velocity and vertical velocity. In the past, multiple across-shelf velocity measurements have been made at both stations FC and SH; 8 and 15 m water depths in 2001 and 15 m and 30 m in 2002. While the accuracy of spatial gradients in these instances deserves further investigation, additional across-shelf deployments of three or more instruments are most likely necessary to properly understand the interaction between across-shelf advection and vertical diffusion in the region. Future projects are also needed to measure or better constrain the vertical advective term and thus the actual amount of upwelling inshore of the PISCO moorings. Process studies using dye tracers would be best suited to make this type of estimate. An intensive dye study during variable wind forcing could document vertical velocities, upwelling, as well as the three-dimensional (3D) movement of water masses, and their associated larvae, into and out of the inner shelf.

Based on the inner-shelf circulation characteristics described in Chapter 3, the southernmost PISCO stations (YB and SH) appear to be advantageous locations to pursue further dynamical studies. The along-shelf spin-up of the 'mini-jet' in this area, isolated from the regional circulation, presents a small-scale laboratory in which theories on upwelling dynamics can be tested over much smaller spatial scales. This study has shown that the important terms in outer-shelf upwelling balances, across-shelf and vertical advection, geostrophic shear, and vertical momentum diffusion, are important in this scaled-down upwelling system as well.

Finally, while across-shelf transport due to along-shelf wind forcing appears to be

the dominant mechanism of across-shelf exchange at water depths as shallow as 15 m along the Oregon coast, it is unclear how far inshore of the 15 m isobath this view holds. Thus, alternative mechanisms of across-shelf transport such as across-shelf wind stress, surface-gravity wave driven undertow, internal waves, and local (1-5 km) scale topographic and bathymetric variations deserve further investigation. In recent observational and numerical studies, across-shelf transport forced by across-shelf winds have been found to be significant in shallow water depths (Fewings et al., 2007; Tilburg, 2003). While the dominant north-south atmospheric forcing and high coastal mountains along much of the central Oregon coast limit the potential significance of this mechanism, there are locations where its effect may be noticeable. Station SR, one such location, is adjacent to a relatively open stretch of the Oregon coast, with irregular coastal mountains set back from the coast compared to sites to the north and south. Based on the results of Chapter 2, station SR appears to have slightly higher mean exchange rates than most of 15 m stations. Thus, this station would be a good candidate to investigate the potential of across-shelf sea-breeze driven upwelling in the inner-shelf, and whether it could account for the higher exchange rates present.

Surface-gravity wave driven 'undertow' also has the potential to cause additional across-shelf transport in the shallower waters of the inner shelf (Lentz et al., 2007; Fewings et al., 2007). This mechanism could be critical to closing the final gap between water depths of 15 m and the surf zone as wave-driven transport increases as water depth decreases (Lentz et al., 2007). Results from the deployment of an Acoustic Wave and Current (AWAC) profiler at PISCO stations in 2005 (not shown here) found coherent wave features across the shelf that were well correlated with wind forcing events. Increased across-shelf exchange due to combined along-shelf wind and wave forcing, above that due to along-shelf wind forcing alone, would be difficult to separate given these conditions. However this mechanism deserves further analysis, both with the PISCO dataset and new

experiments, as incoming surface-gravity waves are significant throughout the year along the Oregon coast.

The effects of internal waves on the hydrography, mixing, and across-shelf transport of the inner shelf is not well known and significant effort is needed in this area. These features exist in the PISCO data set, especially when waters are stratified, making it an excellent starting place for further efforts.

Perhaps the most important alternative mechanism of across-shelf exchange between the surf zone and the inner-shelf is exchange driven by flow-topography interactions at local scales (meters to kilometers). On larger scales, the controlling effect of regional flow-topography interactions on inner-shelf circulation in the region was shown in Chapter 3. As the coastline with its small-scale capes, bays, ridges, and reefs is approached, the 2D along-shelf uniform assumption implicit in all other exchange mechanisms must breakdown. Here, local coastline variations cause rip currents, upwelling shadows, convergences, or retention zones, controlling across-shelf exchange at small spatial scales. This transition point was seen in the across-shelf transport fraction results of Chapter 2 as transports at Station FC, both at 8 m and 15 m water depths, were uncorrelated with the wind while transports at Station LB, 2 km to the north, were well correlated with the wind. It is thought that interactions between circulation and small-scale, local topography caused these calculation failures. Thus an exploration of how the 'mean' circulation features and forcing mechanisms present offshore interacts with the true coastline must occur to fully understand the transport pathways between beaches and rocky headlands and the ocean offshore. Close to shore, these coastline variations control local pressure gradients, wind shadows, and surf zone dynamics, forcing 3D circulation features that may extend far seaward of the feature itself, dominating transport events.

Flow-topography interactions in the inner-shelf could be attacked as an intensive field campaign to fully map bathymetry, hydrography, and circulation in single area,

resolving transport events and quantifying the transition from 3D circulation onshore to 2D circulation offshore. Future work such as this, especially bathymetric measurements, is necessary. However, intensive efforts can not take place everywhere. Additional research to determine the factors controlling the scale of the 3D to 2D transition and the character of its associated across-shelf exchanges is equally important, enabling extrapolation of the results to all locations. Only by including the effects of these additional pathways will the true communication between nearshore waters and the larger coastal ocean be quantified and understood, bridging that last sliver of ocean.

BIBLIOGRAPHY

Allen, J., P. Newberger, and J. Federick, 1995: Upwelling circulation on the Oregon continental shelf, part 1: Response to idealized forcing. *J. Phys. Ocean.*, **25**, 1843–1866.

Allen, J. and R. Smith, 1981: On the dynamics of wind-driven shelf currents. *Phil. Trans. R. Soc. Lond.*, **A302**, 617–634.

Austin, J. and B. Grantham, in progress: Subinertial variability of the Oregon inner shelf. *J. Geophys. Res.*.

Austin, J. and S. Lentz, 2002: The inner shelf response to wind-driven upwelling and downwelling. *J. Phys. Ocean.*, **32**, 2171.

Bane, J., M. Levine, R. Samelson, S. Haines, M. Meaux, N. Perlin, P. Kosro, and T. Boyd, 2005: Atmospheric forcing of the Oregon coastal ocean during the 2001 upwelling season. *J. Geophys. Res.*, **110**, doi:10.1029/2004JC002653.

Barth, J., B. Menge, J. Lubchenco, F. Chan, J. Bane, A. Kirincich, M. McManus, K. Nielsen, S. Pierce, and L. Washburn, 2007: Delayed upwelling alters nearshore coastal ocean ecosystems in the northern California Current. *PNAS*, **104**, 3719–3724.

Barth, J., S. Pierce, and R. Castelao, 2005a: Time-dependent, wind-driven flow over a shallow midshelf submarine bank. *J. Geophys. Res.*, **110**, doi:2004JC002761.

Barth, J., S. Pierce, and T. Cowles, 2005b: Mesoscale structure and its seasonal evolution in the northern California Current System. *Deep Sea Res. II*, **52**, 5–28.

Battisti, D. and B. Hickey, 1984: Application of remote wind-forced coastl trapped wave theory to the Oregon and Washington coasts. *J. Phys. Ocean.*, **14**, 887–903.

Boyd, T., M. Levine, P. Kosro, and S. Gard, 2000: Mooring observations from the Oregon continental shelf: April-September 1999. *Oregon State University Data Report*, **177**.

Boyd, T., M. Levine, P. Kosro, S. Gard, and W. Waldorf, 2002: Observations from moorings on the Oregon continental shelf: May-August 2001. *Oregon State University Data Report*, **190**.

Broitman, B., C. Blanchette, and S. Gaines, 2005: Recuitment of intertidal invertebrates and oceanographic variability at Santa Cruz Island, California. *Limnol. Oceanogr.*, **50**, 1473–1479.

Castelao, R. and J. Barth, 2005: Coastal ocean response to summer upwelling favorable winds in a region of alongshore bottom topography variations off Oregon. *J. Geophys. Res.*, **110**, doi:10.1029/2004JC002409.

Chapman, D., 1987: Application of wind-forced, long, coastal-trapped wave theory along the California coast. *J. Geophys. Res.*, **92**, 1798–1816.

Chapra, S. and R. Canale, 1988: *Numerical methods for engineers*. McGraw-Hill, 839 pp.

Connolly, S., B. Menge, and J. Roughgarden, 2001: A latitudinal gradient in recruitment of intertidal invertebrates in the northeast Pacific ocean. *Ecology*, **82**, 1799–1813.

Cutchin, D. and R. Smith, 1973: Continental shelf waves: low-frequency variations in sea level and currents over the Oregon continental shelf. *J. Phys. Ocean.*, **3**, 73–82.

Davis, R., 1976: Predictability of sea surface temperature and sea level pressure anomalies over the North Pacific Ocean. *J. Geophys. Res.*, **90**, 4741–4755.

Deardorff, J., 1972: Numerical investigation of neutral and unstable planetary boundary layers. *J. Atmos. Sci.*, **29**, 91–115.

Dudas, S., B. Grantham, A. Kirincich, B. Menge, and J. Lubchenco, 2007: Current reversals drive barnacle recruitment on the central Oregon coast: regional and local effects. *in progress*.

Durski, S., S. Glenn, and D. Haidvogel, 2004: Vertical mixing schemes in the coastal ocean: comparison of the level 2.5 Mellor-Yamada scheme with an enhanced version of the K profile parameterization. *J. Geophys. Res.*, **109**, doi:10.1029/2002JC001702.

Ekman, V., 1905: On the influence of the Earth's rotation on ocean-currents. *Arkiv. Math. Astro. Fys.*, **2**, 1–53.

Farrell, T., D. Bracher, and J. Roughgarden, 1991: Cross-shelf transport causes recruitment to intertidal populations in central California. *Limnol. Oceanogr.*, **36**, 279–288.

Feddersen, F., R. Guza, S. Elgar, and T. Herbers, 1998: Alongshore momentum balances in the nearshore. *J. Geophys. Res.*, **103**, 15667–15676.

Federiuk, J. and J. Allen, 1995: Upwelling on the Oregon continental shelf. Part II: simulations and comparisons with observations. *J. Phys. Ocean.*, **25**, 1867–1884.

Fewings, M., S. Lentz, and J. Fredericks, 2007: Observations of cross-shore flow driven by cross-shore winds on the inner continental shelf. *J. Phys. Oceans. (submitted)*.

Gan, J. and J. Allen, 2002: A modeling study of shelf circulation of northern California in the region of the Coastal Ocean Dynamics Experiment: Response to relaxation of upwelling winds. *J. Geophys. Res.*, **107**, doi:10.1029/2000JC000768.

— 2005: Modeling upwelling circulation off the Oregon coast. *J. Geophys. Res.*, **110**, doi:10.1029/2004JC002692.

Garrett, C. and B. Petrie, 1981: Dynamical aspects of the flow through the strait of Belle Isle. *J. Phys. Ocean.*, **11**, 376–393.

Garvine, R., 2004: The vertical structure and subtidal dynamcis of the inner shelf off New Jersey. *J. Mar. Res.*, **62**, 337–371.

Gill, A., 1982: *Atmosphere-ocean dynamics*. Academic Press, 666 pp.

Gordon, R., 1996: *Acoustic Doppler Current Profiler: principles of operation, a practical primer Second edition for Broadband ADCPs*. RDI Instruments, 54 pp.

Grant, W. and O. Madson, 1979: Combined wave and current interaction with a rough bottom. *J. Geophys. Res.*, **84**, 1797–1808.

Grantham, B., F. Chan, K. Nielsen, D. Fox, J. Barth, A. Huyer, J. Lubchenco, and B. Menge, 2004: Upwelling-driven nearshore hypoxia signals ecosystem and oceanographic changes in the northeast Pacific. *Nature*, **429**, 749–754.

Hickey, B., 1998: Coastal oceanography of western North America from the tip of Baja California to Vancouver island. *The Sea, v11*, A. Robinson and K. Brink, eds., John Wiley and Sons, chapter 12, 345–393.

Huyer, A., 1983: Coastal upwelling in the California Current System. *Prog. Oceano.*, **12**, 259–284.

— 1990: Shelf circulation. *The Sea, v9a*, B. LeMehaute and D. Hanes, eds., John Wiley and Sons, chapter 12, 1647–1658.

Huyer, A., J. Fleischbein, J. Keister, P. Kosro, N. Perlin, R. Smith, and P. Wheeler, 2005: Two coastal upwelling domains in the northern California Current System. *J. Mar. Res.*, **63**, 901–929.

Huyer, A., B. Hickey, J. Smith, R. Smith, and R. Pillsbury, 1975: Alongshore coherence at low frequencies in currents observed over the continental shelf off Oregon and Washington. *J. Geophys. Res.*, **80**, 3495–3505.

Huyer, A., R. Smith, and R. Pillsbury, 1974: Observations in a coastal upwelling region during a period of variable winds (Oregon coast, July 1972). *Tethys.*, **6**, 391–404.

Huyer, A., R. Smith, and E. Sobey, 1978: Seasonal differences in low-frequency current fluctuations over the Oregon continental shelf. *J. Geophys. Res.*, **83**, 5077–5089.

Kirincich, A., 2003: The structure and variability of a coastal density front. *Masters Thesis, University of Rhode Island*.

Kirincich, A. and J. Barth, 2007: Spatial and temporal variability of inner-shelf circulation along the central Oregon coast during summer. *J. Phys. Ocean., submitted*.

Kirincich, A., J. Barth, B. Grantham, B. Menge, and J. Lubchenco, 2005: Wind-driven inner-shelf circulation off central Oregon during summer. *J. Geophys. Res.*, **110**, doi:10.1029/2004JC002611.

Kirincich, A. and D. Hebert, 2005: The structure of a coastal density front at the outflow of Long Island Sound during spring 2002. *Cont. Shelf. Res.*, **25**, 1097–1114.

Komar, P., 1998: *Beach processed and sedimentation*. Prentice Hall, 544 pp.

Kosro, P., 2005: On the spatial structure of coastal circulation off Newport, Oregon, during spring and summer 2001 in a region of varying shelf width. *J. Geophys. Res.*, **110**, doi:10.1029/2004JC002769.

Kuebel Cervantes, B., J. Allen, and R. Samelson, 2003: A modeling study of eulerian and lagrangian aspects of shelf circulation off Duck, North Carolina. *J. Phys. Ocean.*, **33**, 2070–2092.

Kundu, P. and J. Allen, 1976: Some three-dimensional characteristics of low-frequency current fluctuations near the Oregon coast. *J. Phys. Ocean.*, **6**, 181–199.

Kundu, P., J. Allen, and R. Smith, 1975: Modal decomposition of the velocity field near the Oregon coast. *J. Phys. Ocean.*, **5**, 683–704.

Large, W. and S. Pond, 1981: Open ocean momentum flux measurements in moderate to strong winds. *J. Phys. Ocean.*, **11**, 324–336.

Lentz, S., 1992: The surface boundary layer in coastal upwelling regions. *J. Phys. Ocean.*, **22**, 1517–1539.

— 1994: Current dynamics over the northern California inner shelf. *J. Phys. Ocean.*, **24**, 2461–2478.

— 1995: Sensitivity of the inner-shelf circulation to the form of the eddy viscosity profile. *J. Phys. Ocean.*, **25**, 19–28.

— 2001: The influence of stratification on the wind-driven cross-shelf circulation over the North Carolina shelf. *J. Phys. Ocean.*, **31**, 2749–2760.

Lentz, S. and D. Chapman, 2004: The importance of nonlinear cross-shelf momentum flux during wind-driven coastal upwelling. *J. Phys. Ocean.*, **34**, 2444–2457.

Lentz, S., M. Fewings, P. Howd, J. Fredericks, and K. Hathaway, 2007: Observations of undertow over the inner continental shelf. *J. Phys. Oceans.*, **submitted**.

Lentz, S., R. Guza, S. Elgar, F. Feddersen, and T. Herbers, 1999: Momentum balances on the North Carolina inner shelf. *J. Geophys. Res.*, **104**, 18205–18226.

Lentz, S. and J. Trowbridge, 1991: The bottom boundary layer over the northern California shelf. *J. Phys. Ocean.*, **21**, 1186–1200.

Lentz, S. and C. Winant, 1986: Subinertial currents on the southern California shelf. *J. Phys. Ocean.*, **16**, 1737–1750.

Leslie, H., E. Breck, F. Chan, J. Lubchenco, and B. Menge, 2005: Barnacle reproductive hotspots linked to nearshore ocean conditions. *PNAS*, **102**, 0534–10539.

Lu, Y. and R. Lueck, 1999: Using a broadband ADCP in a tidal channel. Part 2: Turbulence. *J. Atmos. Ocean Technol.*, **16**, 1568–1579.

Ma, H. and J. Grassle, 2004: Invertebrate larval availability during summer upwelling and downwelling on the inner continental shelf off New Jersey. *J. Mar. Res.*, **62**, 837–865.

MacCready, P. and P. Rhines, 1993: Slippery bottom boundary layers on a slope. *J. Phys. Ocean.*, **23**, 5–22.

Mellor, G. and T. Yamada, 1982: Development of a turbulence closure model for geophysical fluid problems. *Rev. Geophys. and Space Phys.*, **20**, 851–875.

Menge, B., C. Blanchette, P. Raimondi, T. Freidenburg, S. Gaines, J. Lubchenco, D. Lohse, G. Hudson, M. Foley, and J. Pamplin, 2004: Species interaction strength: testing model predictions along an upwelling gradient. *Ecological Monographs*, **74**, 663684.

Menge, B., B. Daley, P. Wheeler, E. Dahlhoff, E. Sanford, and P. Strub, 1997: Benthic-pelagic links and rocky intertidal communities: Bottom-up effects on top-down control? *PNAS*, **94**, 14530–14535.

Menge, B., E. Sanford, B. Daley, T. Freidenburg, G. Hudson, and J. Lubchenco, 2002: An inter-hemispheric comparison of bottom-up effects on community structure: insights revealed using the comparative-experimental approach. *Ecological Research*, **17**, 1–16.

Miller, B. and R. Emlet, 1997: Influence of nearshore hydrodynamics on larval abundance and settlement of sea urchins Stronglocentrotus franciscanus and S. purpuratus in the Oregon upwelling zone. *Ecol. Prog. Ser.*, **148**, 83–94.

Mitchum, G. and A. Clarke, 1986: The frictional nearshore response to forcing by synoptic scale winds. *J. Phys. Oceano.*, **16**, 934–946.

Mooers, C., 1968: A compilation of observations from moored current meters and thermographs, vol 2: Oregon continental shelf, August-September 1966. *OSU Data Report*.

Mooers, C. and R. Smith, 1968: Continental shelf waves off Oregon. *J. Geophys. Res.*, **73**, 549–557.

Morgan, S. G., 2001: The larval ecology of marine communities. *Marine community ecology*, M. Bertness, S. Gaines, and M. Hay, eds., Sinauer Associates, Inc., 159–181.

Oke, P., J. Allen, R. Miller, G. Egbert, J. Austin, J. Barth, T. Boyd, P. Kosro, and M. Levine, 2002a: A modeling study of the three-dimensional continental shelf circulation off Oregon. Part I: model-data comparisons. *J. Phys. Ocean.*, **32**, 1360–1382.

— 2002b: A modeling study of the three-dimensional continental shelf circulation off Oregon. Part II: dynamical analysis. *J. Phys. Ocean.*, **32**, 1383–1403.

Panchang, V. and J. Richardson, 1993: Inverse adjoint estimation of eddy viscosity for coastal flow models. *J. Hydr. Eng.*, **119**, 506–524.

Pauly, D. and V. Christensen, 1995: Primary production required to sustain global fisheries. *Nature*, **374**, 255–257.

Pawlowicz, R., B. Beardsley, and S. Lentz, 2002: Classical tidal harmonic analysis including error estimates in MATLAB using T_TIDE. *Computers and Geosciences*, **28**, 929–937.

Perlin, A., J. Moum, J. Klymak, M. Levine, T. Boyd, and P. Kosro, 2005: A modified law-of-the-wall applied to oceanic bottom boundary layers. *J. Geophys. Res.*, **110**, doi:10.1029/2004JC002310.

Picket, M. and J. Paduan, 2003: Ekman transport and pumping in the California current based on the U.S. Navy's high-resolution atmospheric model (COAMPS). *J. Geophys. Res.*, **108**, doi:10.1029/2003JC001902.

Reed, B., 1992: Linear least-squares fits with errors in both coordinates. *Am. J. Phys.*, **60**, 59–62.

Rilov, G., 2007: Barnacle and mussel larval distributions, pers. comm.

Roughgarden, J., S. Gaines, and H. Possingham, 1998: Recruitment dynamics in complex life cycles. *Science*, **241**, 1460–1466.

Samelson, R., 1997: Coastal boundary conditions and the baroclinic structure of wind-driven continental shelf currents. *J. Phys. Ocean.*, **27**, 2645–2662.

Samelson, R., P. Barbour, J. Barth, S. Bielli, T. Boyd, D. Chelton, P. Kosro, M. Levine, and E. Skyllingstad, 2002: Wind stress forcing of the Oregon coastal ocean during the 1999 upwelling season. *J. Geophys. Res.*, **107**, doi: 10.1029/2001JC00900.

Signell, R., R. Beardsley, H. Graber, and A. Capotondi, 1990: Effect of wave-current interaction on wind-driven circulation in narrow, shallow embayments. *J. Geophys. Res.*, **95**, 9671–9678.

Small, L. and D. Menzies, 1981: Patterns of primary productivity and biomass in a coastal upwelling region. *Deep-sea Res.*, **28**, 123–149.

Smith, J. and C. Long, 1976: The effects of turning in the bottom boundary layer on continental shelf sediment transport. *Mem. Soc. Roy. Sci. Liege. Ser.*, **6**, 369–396.

Smith, R., 1974: A description of current, wind, and sea level variations during coastal upwelling off the Oregon coast, July/August 1972. *J. Geophys. Res.*, **79**, 435–443.

— 1995: The physical processes of coastal ocean upwelling systems. *Upwelling and the ocean: modern processes and ancient records*, C. Summerhayes, K. Emeres, M. Angel, R. Smith, and B. Zeitzchel, eds., John Wiley and Sons, 39–64.

Smith, R., A. Huyer, and J. Fleischbein, 2001: The coastal ocean off Oregon from 1961 to 2000: is there evidence of climate change or only of Los Ninos? *Prog. Ocean.*, **29**, 63–93.

Stacey, M., S. Monismith, and J. Burau, 1999: Measurements of Reynolds stress profiles in unstratified tidal flow. *J. Geophys. Res.*, **104**, 10933–10949.

Svendsen, I., 2006: *Introduction to nearshore hydrodynamics*. World Scientific, 722 pp.

Tilburg, C., 2003: Across-shelf transport on a continental shelf: do across-shelf winds matter? *J. Phys. Oceano.*, **33**, 2675–2688.

Whipple, A. and H. Luettich, R.A. Seim, 2005: Measurements of Reynolds stress in a wind-driven lagoonal estuary. *Ocean Dynamics*, **21**, DOI 10.1007/s10236–005–0038–x.

Wijesekera, H., J. Allen, and P. Newberger, 2003: Modeling study of turbulent mixing over the continental shelf. *J. Geophys. Res.*, **108**, doi:10.1029/2001JC001234.

Williams, E. and J. Simpson, 2004: Uncertainties in estimates of Reynolds stress and TKE production rate using the ADCP variance method. *J. Atmos. Ocean Technol.*, **21**, 347–357.

Winant, C., 1980: Downwelling over the southern California shelf. *J. Phys. Ocean.*, **10**, 791–799.

Wiseman, W. and R. Garvine, 1995: Plumes and coastal currents near large river mouths. *Estuaries*, **18**, 509–517.

Woodson, C., D. Webster, M. Weissburg, and J. Yen, 2005: Response of copepods to physical gradients associated with structure in the ocean. *Limol. Oceanogr.*, **5**, 1552–1564.

Yankovsky, A., R. Garvine, and A. Munchow, 2000: Mesoscale currents on the inner New Jersey shelf driven by the interaction of buoyancy and wind forcing. *J. Phys. Oceano.*, **5**, 2214–2230.

Yu, L. and J. O'Brien, 1991: Variational estimation of the wind stress drag coefficient and oceanic eddy viscosity profile. *J. Phys. Ocean.*, **21**, 709–719.

— 1992: On the initial condition in parameter estimation. *J. Phys. Ocean.*, **22**, 1361–1364.